RF pulse design for parallel excitation in MRI

by

William Allyn Grissom

A dissertation submitted in partial fulfillment
of the requirements for the degree of
Doctor of Philosophy
(Biomedical Engineering)
in The University of Michigan
2008

Doctoral Committee:

Professor Douglas C. Noll, Chair
Professor Jeffrey A. Fessler
Professor Eric Michielssen
Professor Thomas Chenevert

ACKNOWLEDGEMENTS

I have many people to thank.

First, I would like to thank Doug Noll, for taking me on as a student five years ago. He is the best mentor I have ever had, and I look up to him as a model of what an engineer should be. He is creative, open-minded, friendly and excited about his work. I was blessed to have him as an advisor, and I am excited to be working in a field with people like him in it.

I would also like to thank Jeff Fessler, from whom I have also learned a ton, and who I would also like to emulate. I never left a meeting with Jeff without a new idea or direction. His dedication to his students and his ability to switch between modes of thinking for each students' project is amazing.

Chun-yu Yip has been like my lab-brother. We started working together when I first joined the lab, and I know my constant questioning must have been annoying at first, but I have learned a lot from him, and I feel as though we have grown up as MR engineers together. His skills as a communicator and his attention to detail make him a great scientist, who will surely do wonderful things in his career. I would also like to thank the rest of my senior lab-mates Valur Olafsson, Greg Lee, Kiran Pandey, Alberto Vazquez, Sangwoo Lee and Yoon Chung Kim, for helping me out whenever I had a problem with the scanner, or my computer, or anything else. You guys have been great and supportive friends. I would also like to thank Luis, Eve, Scott, Chuck and Keith, who have also helped me a great deal, and whose tireless work keeps our lab running like a dream.

I would like to thank Eric Michielssen, for serving on my committee, and for being a great EM teacher whose classes I have truly enjoyed taking, and Tom Chenevert, for serving on my committee and providing constructive feedback on my research.

I am grateful to Troy Stevens, whom I worked for at General Dynamics just before grad school. Troy piqued my interest in research and encouraged me to continue with school.

I also have to thank my dogs, Billy and Sugar, for providing comic relief at home, and reminding me that life is pretty much silly most of the time.

Rachael, my wife, has done so much to support me over the years. She was the one who encouraged me to go talk to somebody in medical imaging (who turned out to be Doug) about getting involved in research. Both as friends in undergrad, and as my partner in grad school, she has always been there, through happy and stressful times. She is my best friend. I owe her so much.

Finally, I want to thank my family. My mom Sally, my dad Tim, my brother Matt, my sisters Jessica and Sarah, my grandparents and my aunts. I love you all; thanks for helping me get here.

William Grissom

Ann Arbor, Michigan

24 November, 2007

TABLE OF CONTENTS

LIST OF FIGURES

Figure

CHAPTER I

Introduction

This research project focuses on the development of RF pulse design techniques in parallel excitation. Parallel excitation was first proposed by Katscher et al [1] and Zhu [2] as a means of accelerating multi-dimensional excitation by performing excitation using multiple coils driven with independent waveforms. It was a natural extension of ideas that had emerged in the field of parallel imaging to the excitation stage of MRI. In a manner analogous to parallel imaging methods such as SENSE [3] or GRAPPA [4], parallel excitation enables a more rapid traversal of the spatial frequency domain to excite a desired magnetization pattern, by exploiting the localized influence of surface coils to deposit RF energy in untraversed regions of the spatial frequency-domain. Because parallel excitation is a new field in MRI, current research focuses on the basics; hardware implementation, applications, and pulse design methods.

In this chapter, we will review fundamental theories of excitation in MRI that are necessary to the development of new parallel excitation pulse design methods, and to the analysis of these methods' performance. We will begin with the Bloch equation, and then introduce Fourier analyses of RF excitation that facilitate fast pulse design, and review a single-coil Fourier-based RF pulse design method. We will introduce parallel excitation and the motivations for its use, followed by a review of current parallel pulse design meth-

ods. I will then state the major goals of this project that will be addressed by subsequent chapters.

1.1 The Bloch Equation

The Bloch equation [5] governs the precession of a nuclear magnetic moment $\boldsymbol{m}(\boldsymbol{x}) = (m_x(\boldsymbol{x}), m_y(\boldsymbol{x}), m_z(\boldsymbol{x}))^T$ about a time-varying externally-applied magnetic field $\boldsymbol{\omega}(t) = (\omega_x(t), \omega_y(t), \omega_z(t))^T$. In the context of MR excitation, the Bloch equation relates the gradient fields $\boldsymbol{G}(t) = (G_x(t), G_y(t), G_z(t))^T$ and the RF magnetic fields $\boldsymbol{b}_1(t) = (b_{1,x}(t), b_{1,y}(t))^T$ to the time derivative of the magnetization. In a frame that rotates at the Larmor frequency, the Bloch equation is given by:

$$\frac{d\boldsymbol{m}(\boldsymbol{x},t)}{dt} = \gamma \begin{pmatrix} 0 & \boldsymbol{G}(t)\cdot\boldsymbol{x} & -b_{1,y}(t) \\ -\boldsymbol{G}(t)\cdot\boldsymbol{x} & 0 & b_{1,x}(t) \\ b_{1,y}(t) & -b_{1,x}(t) & 0 \end{pmatrix} \boldsymbol{m}(\boldsymbol{x},t), \tag{1.1}$$

where γ is the gyromagnetic ratio of the nucleus of interest, and we have neglected relaxation effects. Here, we assume that the RF fields are spatially uniform, though in later sections we will generalize our analysis to non-uniform fields, as is the case in parallel excitation. Equation 1.1 can be used to determine the magnetization state following RF excitation, given an initial magnetization state and RF pulse and gradient waveforms. The goal of our work is to develop methods for designing pulses $\boldsymbol{b}_1(t)$ that rotate magnetization from an initial state $\boldsymbol{m}(\boldsymbol{x},0)$ at the beginning of the pulse, to a desired state $\boldsymbol{m}_{des}(\boldsymbol{x},T)$ at the end of the pulse.

Later we will make use of an alternative *spin domain* expression of the Bloch equation [6]. While Eq. 1.1 operates on the magnetization directly, the spin domain Bloch equation operates on the rotation matrix, which is determined by two complex *spinor* parameters, α and β. Together they describe a rotation by an angle ϕ about a unit axis vector $\hat{\boldsymbol{n}} =$

(n_x, n_y, n_z), as:

$$\alpha = \cos\frac{\phi}{2} + in_z \sin\frac{\phi}{2} \tag{1.2}$$

$$\beta = i\left(n_x - in_y\right)\sin\frac{\phi}{2}. \tag{1.3}$$

In the spin domain, α and β determine a rotation matrix, given by:

$$\boldsymbol{Q} = \begin{pmatrix} \alpha & \beta \\ -\beta^* & \alpha^* \end{pmatrix}, \tag{1.4}$$

where '*' denotes complex conjugate. The spin domain version of the Bloch equation is:

$$\begin{pmatrix} \dot{\beta} \\ \dot{\alpha}^* \end{pmatrix} = \frac{i\gamma}{2}\begin{pmatrix} \boldsymbol{G}(t)\cdot\boldsymbol{x} & b_1^*(t) \\ b_1(t) & -\boldsymbol{G}(t)\cdot\boldsymbol{x} \end{pmatrix}\begin{pmatrix} \beta \\ \alpha^* \end{pmatrix}, \tag{1.5}$$

where $b_1(t) = b_{1,x}(t) + ib_{1,y}(t)$. Given an initial magnetization state $\left(m_{xy}^-, m_z^-\right)$, where $m_{xy} = m_x + im_y$, the magnetization state following the application of a pulse $b_1(t)$ and gradient waveform $\boldsymbol{G}(t)$ is given by:

$$\begin{pmatrix} m_{xy}^+ \\ m_{xy}^{+*} \\ m_z^+ \end{pmatrix} = \begin{pmatrix} (\alpha^*)^2 & -(\beta^*)^2 & -2\alpha^*\beta^* \\ -\beta^2 & \alpha^2 & -2\alpha\beta \\ \alpha^*\beta & \alpha\beta^* & \alpha\alpha^* - \beta\beta^* \end{pmatrix}\begin{pmatrix} m_{xy}^- \\ m_{xy}^{-*} \\ m_z^- \end{pmatrix}, \tag{1.6}$$

where α and β are the solutions to Eq. 1.5 for $b_1(t)$ and $\boldsymbol{G}(t)$.

1.2 Fourier Interpretations of Selective Excitation

1.2.1 Small-tip-angle approximation

The small-tip-angle approximation to the Bloch equation, first introduced by Pauly et al [7], greatly simplifies small-tip-angle RF pulse design by providing a Fourier relationship between an RF pulse and the magnetization pattern it excites. It is the basis of all small-tip-angle parallel pulse design algorithms, and inspires the large-tip-angle pulse design strategies we will introduce in Chapters III and IV. To derive it, we make the assumptions

that (i) magnetization is at equilibrium at the beginning of the pulse, i.e., $\boldsymbol{m}(\boldsymbol{x},0) = (0,0,M_0(\boldsymbol{x}))^T$, where $M_0(\boldsymbol{x})$ is the equilibrium magnetization, and (ii) that the RF pulse $b_1(t)$ excites a small angle $\theta < 30°$. These assumptions lead to the approximation that $M_z(t)$ remains constant during the RF pulse. The Bloch equation becomes:

$$\frac{d\boldsymbol{m}(\boldsymbol{x},t)}{dt} \approx \gamma \begin{pmatrix} 0 & \boldsymbol{G}(t)\cdot\boldsymbol{x} & -b_{1,y}(t) \\ -\boldsymbol{G}(t)\cdot\boldsymbol{x} & 0 & b_{1,x}(t) \\ b_{1,y}(t) & -b_{1,x}(t) & 0 \end{pmatrix} \begin{pmatrix} m_x(\boldsymbol{x},t) \\ m_y(\boldsymbol{x},t) \\ M_0(\boldsymbol{x}) \end{pmatrix}. \tag{1.7}$$

Multiplying this out for the $\frac{dm_x(\boldsymbol{x},t)}{dt}$ and $\frac{dm_y(\boldsymbol{x},t)}{dt}$ terms, and combining them to obtain a complex magnetization $m(\boldsymbol{x},t) = m_x(\boldsymbol{x},t) + im_y(\boldsymbol{x},t)$ gives:

$$\frac{dm(\boldsymbol{x},t)}{dt} \approx -i\boldsymbol{G}(t)\cdot\boldsymbol{x}m(\boldsymbol{x},t) + ib_1(t)M_0(\boldsymbol{x}), \tag{1.8}$$

Equation 1.8 is a first order linear differential equation whose solution at the end of a pulse of length T is given by:

$$m(\boldsymbol{x},T) = i\gamma M_0(\boldsymbol{x}) \int_0^T b_1(t)\, e^{-i\gamma\boldsymbol{x}\cdot\int_t^T \boldsymbol{G}(t')t'} dt. \tag{1.9}$$

From this equation we can introduce a spatial frequency variable that is defined as a time-reversed integration of the gradient waveform $\boldsymbol{G}(t)$:

$$\boldsymbol{k}(t) = -\gamma \int_t^T \boldsymbol{G}(t')\, dt', \tag{1.10}$$

and rewrite Eq. 1.9 as:

$$m(\boldsymbol{x},T) = i\gamma M_0(\boldsymbol{x}) \int_0^T b_1(t)\, e^{i\boldsymbol{x}\cdot\boldsymbol{k}(t)} dt. \tag{1.11}$$

This equation has a simple interpretation. Under small-tip-angle assumptions, the excited pattern $m(\boldsymbol{x},T)$ is given by a Fourier integral that is weighted by the RF pulse $b_1(t)$ at spatial frequency locations determined by the *excitation k-space trajectory* $\boldsymbol{k}(t)$. We will revisit this formalism many times in this and later chapters.

A second, less-common interpretation of Eq. 1.11 that we will use in Chapter III can be derived by relating $m(\boldsymbol{x}, T)$ to the initial longitudinal magnetization and the spinor parameters representing RF excitation. Equation 1.6 gives this relationship:

$$\begin{aligned} m(\boldsymbol{x}, T) &= -2\alpha^*(\boldsymbol{x}, T)\,\beta^*(\boldsymbol{x}, T)\,M_0(\boldsymbol{x}) \\ &= 2i\cos\frac{\phi(\boldsymbol{x}, T)}{2}\left(n_x(\boldsymbol{x}, T) + in_y(\boldsymbol{x}, T)\right)\sin\frac{\phi(\boldsymbol{x}, T)}{2}M_0(\boldsymbol{x})\,. \end{aligned} \tag{1.12}$$

Here we have chosen to represent excitation as a rotation about an x-y vector, so $n_z = 0$. We have done this because it allows us to interpret $\phi(\boldsymbol{x}, T)$ as the *tip-angle*, i.e., the positive angle between the excited magnetization and the z-axis. Because $\phi(\boldsymbol{x}, T)$ is small, $\cos\frac{\phi(\boldsymbol{x},T)}{2} \approx 1$ and $\sin\frac{\phi(\boldsymbol{x},T)}{2} \approx \frac{\phi(\boldsymbol{x},T)}{2}$. Making these substitutions gives:

$$\begin{aligned} m(\boldsymbol{x}, T) &\approx 2i\left(n_x(\boldsymbol{x}, T) + in_y(\boldsymbol{x}, T)\right)\frac{\phi(\boldsymbol{x}, T)}{2}M_0(\boldsymbol{x}) \\ &= \phi(\boldsymbol{x}, T)\,e^{i\angle m(\boldsymbol{x},T)}M_0(\boldsymbol{x})\,, \end{aligned} \tag{1.13}$$

where the second equality follows from the fact that $\phi(\boldsymbol{x}, T)$ and $M_0(\boldsymbol{x})$ are real and positive, so the phase of $m(\boldsymbol{x}, T)$ must equal that of $i\left(n_x(\boldsymbol{x}, T) + in_y(\boldsymbol{x}, T)\right)$, which has unit norm. Equating (1.13) and (1.11), and dividing both sides by $M_0(\boldsymbol{x})$ gives the relationship we seek:

$$\phi(\boldsymbol{x}, T)\,e^{i\angle m(\boldsymbol{x},T)} = i\gamma\int_0^T b_1(t)\,e^{i\boldsymbol{x}\cdot\boldsymbol{k}(t)}dt. \tag{1.14}$$

This shows that under the small-tip-angle regime, Eq. 1.11 can be used to obtain a complex-valued pattern whose magnitude equals the tip-angle excited by the pulse, and whose phase corresponds to that of the excited magnetization.

1.2.2 Small-excitation approximation

Away from equilibrium, Pauly et al [8] derived another Fourier relationship for an RF pulse that excites a small angle. The relationship is formulated in the spin domain, and is

therefore independent of the initial magnetization state. It is derived by first inspecting the spin-domain Bloch equation for the parameter α^*:

$$\dot{\alpha}^* = \frac{i\gamma}{2}\left(b_1(t)\,\beta - \boldsymbol{G}(t)\cdot\boldsymbol{x}\alpha^*\right). \tag{1.15}$$

We then invoke the small-excitation approximation, by assuming that $b_1(t)\,\beta$ is small. This is a reasonable approximation for two reasons: (i) for a small rotation, $|\alpha^*| \approx 1$, and β is near zero, and (ii) for non-central spatial locations, as well as for the majority of a selective pulse's duration, the magnitude of the RF field $b_1(t)$ is smaller than the gradient field $\boldsymbol{G}(t)\cdot\boldsymbol{x}$. This reduces the α^* equation to:

$$\dot{\alpha}^* + \left(\frac{i\gamma}{2}\boldsymbol{G}\cdot\boldsymbol{x}\right)\alpha^* = 0, \tag{1.16}$$

the solution of which is given by (with initial condition $\alpha^*(0) = 1$, corresponding to no rotation):

$$\alpha^*(t) = e^{-\frac{i\gamma}{2}\boldsymbol{x}\cdot\int_0^t \boldsymbol{G}(t')dt'}. \tag{1.17}$$

This solution can then be used to solve the β equation,

$$\dot{\beta} = \frac{i\gamma}{2}\left(\boldsymbol{G}(t)\cdot\boldsymbol{x}\beta + b_1^*(t)\,\alpha^*\right), \tag{1.18}$$

the solution of which is given by (for initial condition $\beta(0) = 0$, again corresponding to no rotation):

$$\beta(T) = \frac{i\gamma}{2}e^{-\frac{i\gamma}{2}\boldsymbol{x}\cdot\int_0^T \boldsymbol{G}(t')dt'}\int_0^T b_1^*(t)\,e^{i\gamma\boldsymbol{x}\cdot\int_t^T \boldsymbol{G}(t')dt'}dt. \tag{1.19}$$

As in the small-tip-angle case, we can simplify these expressions by substituting the spatial frequency variable $\boldsymbol{k}(t)$ (Eq. 1.10) into Eqs. 1.17 and 1.19, yielding:

$$\alpha^*(T) = e^{\frac{i}{2}\boldsymbol{x}\cdot\boldsymbol{k}(0)} \tag{1.20}$$

$$\beta(T) = \frac{i\gamma}{2}e^{\frac{i}{2}\boldsymbol{x}\cdot\boldsymbol{k}(0)}\int_0^T b_1^*(t)\,e^{-i\boldsymbol{x}\cdot\boldsymbol{k}(t)}dt. \tag{1.21}$$

To summarize, we have reviewed the derivation of a linear, Fourier relationship between a small-flip-angle pulse $b_1(t)$, and the spinor parameters (α^*, β) produced by that pulse. In Chapter IV we will use a similar analysis to derive a large-tip-angle parallel excitation pulse design method.

1.2.3 The Linear Class of Large-tip-angle Pulses

Small-excitation analysis has been used to characterize a class of Fourier-designed pulses that can be scaled to accurately excite large-tip-angles [8]. Consider an RF pulse $b_1(t)$ that is played out along an excitation k-space trajectory $\boldsymbol{k}(t)$, and suppose $b_1(t)$ deposits energy in a Hermitian-symmetric manner. That is, for each location in k-space that the pulse deposits energy, it also deposits energy with a conjugate weighting at a location that is symmetric about the origin. Suppose further that the trajectory is refocused, i.e., $\boldsymbol{k}(0) = 0$. Under these assumptions, the spinor parameters for this pulse are:

$$\alpha^*(T) = 1 \tag{1.22}$$

$$\beta(T) = \frac{i\gamma}{2} \int_0^T b_1^*(t)\, e^{-i\boldsymbol{x}\cdot\boldsymbol{k}(t)} dt, \tag{1.23}$$

where $\beta(T)$ is a purely imaginary function of $\boldsymbol{x}$. If we refer back to Eq. 1.2, we notice that real α and imaginary β correspond to a rotation about an axis

$$\hat{\boldsymbol{n}} = (1, 0, 0), \tag{1.24}$$

that is not a function of $\boldsymbol{x}$. If we again refer to Eq. 1.2, we see that in this scenario, $\beta = i \sin\frac{\phi}{2}$. Since for small $\frac{\phi}{2}$, $\sin\frac{\phi}{2} \approx \frac{\phi}{2}$, we can approximate ϕ as:

$$\begin{aligned} \phi &\approx 2 \sin\frac{\phi}{2} \\ &= \frac{2}{i}\beta \\ &= \gamma \int_0^T b_1^*(t)\, e^{-i\boldsymbol{x}\cdot\boldsymbol{k}(t)} dt. \end{aligned} \tag{1.25}$$

This result shows that a small-excitation inherently refocused pulse excites a flip angle pattern that is the Fourier transform of the RF-weighted k-space trajectory. Note that our analysis has made no assumptions about the initial magnetization state. Now, we use this analysis to synthesize a large-tip-angle pulse via concatenation of a series of small-excitation pulses. Consider a scenario in which we are given a large-tip-angle pulse that may be decomposed into a sequence of n small-excitation, Hermitian-symmetric, refocused pulses. The rotation produced by the j-th pulse is

$$\phi_j = \gamma \int_{T_{j-1}}^{T_j} b_1^* (t)\, e^{-i\boldsymbol{x}\cdot\boldsymbol{k}_j(t)} dt, \tag{1.26}$$

where $\boldsymbol{k}_j (t)$ is a refocused trajectory given by:

$$\boldsymbol{k}_j (t) = -\gamma \int_t^{T_j} \boldsymbol{G} (t')\, dt'. \tag{1.27}$$

Because each of these pulses rotates magnetization about the vector $\hat{\boldsymbol{n}} = (1, 0, 0)$, the flip angles they produce add, and the flip angle pattern resulting from their concatenation is

$$\begin{aligned} \phi &= \sum_{j=1}^{n} \phi_j \\ &= \sum_{j=1}^{n} \gamma \int_{T_{j-1}}^{T_j} b_1^* (t)\, e^{-i\boldsymbol{x}\cdot\boldsymbol{k}_j(t)} dt \\ &= \gamma \int_0^T b_1^* (t)\, e^{-i\boldsymbol{x}\cdot\boldsymbol{k}(t)} dt. \end{aligned} \tag{1.28}$$

This result shows that a pulse that can be decomposed into a series of small-excitation, Hermitian-symmetric refocused pulses excites a flip angle pattern equal to the Fourier transform of the pulse, evaluated along the excitation k-space trajectory. Because we have only invoked the small-excitation approximation for the subpulses, the pulse obtained by their concatenation may excite large-tip-angles, so the result holds for large-tip-angle pulses. The conditions under which the approximations made in this section hold are collectively referred to as the *linear class conditions*. We will visit them again in Chapter II

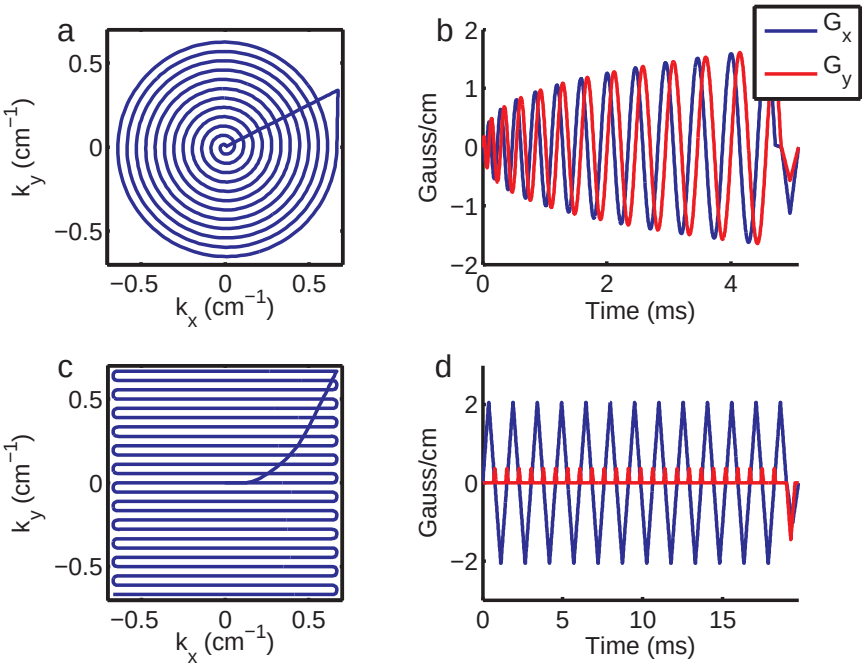

Figure 1.1: (a) A spiral k-space trajectory, obtained by time-reversed integration of the gradient waveforms in (b). (c) An echo-planar (EP) trajectory and (d) the gradient waveforms that generate it.

when analyzing the performance of small-tip-designed parallel excitation pulses at large tip-angles. Their practical consequence is that one can design a pulse $b_1(t)$ using a linear Fourier analysis, and as long as the pulse and its trajectory satisfy these conditions, the pulse may be scaled to excite accurate large-tip-angle patterns. Not all excitation k-space trajectories may be decomposed into refocused trajectories, however. For example, the two most commonly-used two-dimensional excitation k-space trajectories are spiral and echo-planar (EP). Both are illustrated in Fig. 1.1. Between these, only the spiral may be approximately decomposed into refocused trajectories. To design pulses that do satisfy the linear class conditions, one may use the small-tip-angle expression of Eq. 1.11, by simply re-interpreting the excited magnetization pattern as the flip angle pattern, in radians. Therefore, any general small-tip-angle pulse design method can also be used to design large-tip-angle pulses.

1.3 Iterative Small-tip-angle Selective Excitation Pulse Design

In 2005, Yip et al introduced an iterative method for small-tip-angle RF pulse design [9]. The method forms the basis of the small-tip-angle pulse design method of Chapter II, and its discrete model-based formulation is analogous to the large-tip-angle method of Chapter IV, so we will introduce it here. It represents a major improvement over previous pulse design methods, which we refer to as *conjugate phase* methods [10]. Specifically, it permits control of the magnitude of a pulse, does not require computation of a Jacobian determinant, minimizes excitation error, allows for the incorporation of regions of interest (ROI's) to improve excitation accuracy, and is capable of modeling and accounting for off-resonance in pulse design in a more robust manner than conjugate phase methods. It is a model-based approach, analogous to recently-developed iterative image reconstruction techniques [11, 12] that improve image quality relative to conjugate phase reconstruction methods [11–13].

The iterative small-tip-angle pulse design method is derived from the small-tip-angle formula (Eq. 1.11). Including phase evolution due to a static off-resonance map $\Delta\omega\left(\boldsymbol{x}\right)$, and re-writing m as a function of the pulse $b_1\left(t\right)$, this is

$$m\left(\boldsymbol{x};b_1\right) = i\gamma M_0\left(\boldsymbol{x}\right)\int_0^T b_1\left(t\right)e^{i\boldsymbol{x}\cdot\boldsymbol{k}(t)+i\Delta\omega(\boldsymbol{x})(t-T)}dt. \tag{1.29}$$

In practice, an RF pulse is played out as a series of hard pulses on a high-rate digital-to-analog (D/A) converter. The pulse is then modulated to the resonant frequency of the chemical species to be excited, and is played out through an amplifier and coil. Though the RF circuitry and the loaded coil effect a temporal smoothing of each hard pulse, it is common practice to model the point spread function (PSF) of the RF system as narrow. We therefore represent an RF pulse $b_1\left(t\right)$ as a weighted train of N_t Dirac impulses, with a sampling period of Δt seconds, though alternative PSF's could easily be incorporated in

our analysis. Under these assumptions, we can approximate Eq. 1.29 as

$$m\left(\boldsymbol{x};b_1\right) \approx i\gamma\Delta t M_0\left(\boldsymbol{x}\right)\sum_{j=1}^{N_t} b_1\left(t_j\right) e^{i\boldsymbol{x}\cdot\boldsymbol{k}(t_j)+i\Delta\omega(\boldsymbol{x})(t_j-T)}. \tag{1.30}$$

Sampling the magnetization m at spatial locations $\{\boldsymbol{x}_i\}_{i=1}^{N_s}$ yields a matrix/vector equation:

$$\boldsymbol{m} \approx \boldsymbol{A}\boldsymbol{b}, \tag{1.31}$$

where $\boldsymbol{m} = \left[m\left(\boldsymbol{x}_1;b_1\right),\ldots,m\left(\boldsymbol{x}_{N_s};b_1\right)\right]^T$, $\boldsymbol{b} = \left[b_1\left(t_1\right),\ldots,b_1\left(t_{N_t}\right)\right]^T$, and the elements of the $N_s \times N_t$ *system matrix* are given by:

$$a_{ij} = i\gamma M_0\left(\boldsymbol{x}\right)\Delta t e^{i\boldsymbol{x}\cdot\boldsymbol{k}(t_j)+i\Delta\omega(\boldsymbol{x})(t_j-T)}. \tag{1.32}$$

We are now in a position to define an optimization problem to design the RF pulse. The pulse that solves this problem will minimize a quadratic cost function, consisting of a term that quantifies excitation error and terms to control other pulse attributes, such as integrated or instantaneous pulse power. The problem is given by:

$$\hat{\boldsymbol{b}} = \underset{\boldsymbol{b}}{\operatorname{argmin}}\left\{\|\boldsymbol{A}\boldsymbol{b}-\boldsymbol{d}\|_{\boldsymbol{W}}^2 + R\left(\boldsymbol{b}\right)\right\}, \tag{1.33}$$

where $\boldsymbol{d}$ is a vector containing samples of the desired excitation pattern, $\boldsymbol{W}$ is an $N_s \times N_s$ diagonal spatial weighting matrix that can be used to specify a Region of Interest (ROI), and $R\left(\boldsymbol{b}\right)$ is a regularization term. To reduce integrated RF power, the user can set $R\left(\boldsymbol{b}\right) = \beta\boldsymbol{b}'\boldsymbol{b}$, where β is a user-selected Tikhonov regularization parameter that is chosen to strike an appropriate balance between excitation error and integrated power, and $'$ denotes complex conjugate transpose. The optimization problem can be solved efficiently using the Conjugate Gradient (CG) algorithm [12], and in the case $\Delta\omega\left(\boldsymbol{x}\right) = 0$, non-uniform Fast Fourier transforms (NUFFT's) [14] can be used to evaluate multiplications with the system matrix $\boldsymbol{A}$. For non-zero off-resonance maps, one can use time- or frequency-segmentation approaches combined with NUFFT's to achieve fast computation [15, 16].

1.4 Parallel Excitation

Up to now, the excitation theory and techniques introduced in this chapter have presumed that excitation was performed with a single coil. We further assumed that the magnetic field produced by a current running through this coil is uniform within the object being excited, so that a non-selective pulse excites spatially-uniform flip angles. Measured in the rotating frame of reference, the magnetic field produced by a current running through the coil is referred to as the B_1^+ field. In parallel excitation, multiple surface coils are placed around an object, each of which produces an intentionally *non*-uniform B_1^+ field. In this context the B_1^+ fields are referred to as *transmit sensitivity patterns*. An example set of transmit sensitivity patterns for an array of surface coils is shown in Fig. 1.2. Generally, the fields are smoothly-varying, are peaked near the coil, and fall off slowly away from the coil. Mathematically, in parallel excitation we model the RF field produced by a single coil as a separable function of time and space:

$$b_1(\boldsymbol{x}, t) = s(\boldsymbol{x})\, b_1(t), \tag{1.34}$$

where $s(\boldsymbol{x})$ is the complex-valued B_1^+ field, and is generally taken to have units of magnetic field magnitude (Gauss or Tesla) per full RF waveform magnitude. By the linearity of magnetic fields in biological tissue, the fields imposed by multiple coils sum, so that the total excitation field is

$$b_{tot}(\boldsymbol{x}, t) = \sum_{r=1}^{R} s_r(\boldsymbol{x})\, b_{1,r}(t), \tag{1.35}$$

where R is the number of coils.

To elucidate the mechanism underlying parallel excitation, we re-visit the small-tip-angle formula of Eq. 1.11, now substituting the spatially-varying multiple-coil RF model

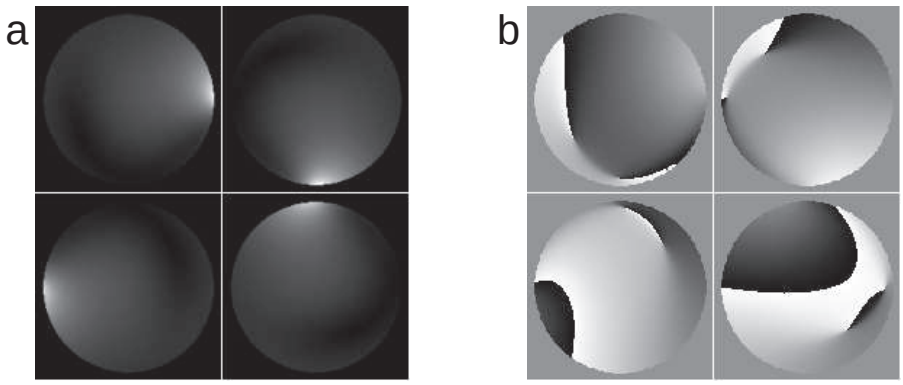

Figure 1.2: Simulated (a) magnitude and (b) phase of B_1^+ fields for 4 coils in a transmit array . The fields are peaked near the coil, and fall off slowly away from the coil. They vary slowly in both magnitude and phase. Simulation details are given in Section 3.3.2.

of Eq. 1.35 for $b_1(t)$:

$$\begin{aligned} m(\boldsymbol{x},T) &= i\gamma M_0(\boldsymbol{x}) \int_0^T b_{tot}(\boldsymbol{x},t)\, e^{i\boldsymbol{x}\cdot\boldsymbol{k}(t)} dt \\ &= i\gamma M_0(\boldsymbol{x}) \int_0^T \sum_{r=1}^{R} s_r(\boldsymbol{x})\, b_{1,r}(t)\, e^{i\boldsymbol{x}\cdot\boldsymbol{k}(t)} dt \\ &= i\gamma M_0(\boldsymbol{x}) \sum_{r=1}^{R} s_r(\boldsymbol{x}) \int_0^T b_{1,r}(t)\, e^{i\boldsymbol{x}\cdot\boldsymbol{k}(t)} dt \\ &= \sum_{r=1}^{R} s_r(\boldsymbol{x})\, m_r(\boldsymbol{x},T), \end{aligned} \tag{1.36}$$

where the $m_r(\boldsymbol{x},T)$ are the patterns that would be excited by the pulses $b_{1,r}(t)$ if each were played through coils with uniform sensitivities $s_r(\boldsymbol{x}) = 1$. Equation 1.36 can be equivalently expressed in the the Fourier domain as:

$$\tilde{m}(\boldsymbol{k}) = \sum_{r=1}^{R} \tilde{s}_r(\boldsymbol{k}) \otimes \tilde{m}_r(\boldsymbol{k}), \tag{1.37}$$

where $\tilde{m}(\boldsymbol{k})$, $\tilde{s}_r(\boldsymbol{k})$, and $\tilde{m}_r(\boldsymbol{k})$ are the Fourier transforms of the total excited magnetization pattern, the sensitivities, and the individual excited patterns, respectively, and $\otimes$ denotes a convolution. Because the Fourier transforms of the individual excitation patterns $\tilde{m}_r(\boldsymbol{k})$ are the pulses $b_{1,r}(t)$, this expression shows that the localized sensitivity patterns

of the coils have the effect of blurring RF pulse energy in k-space. In parallel excitation, we use multiple coils to control this blurring effect. This allows us to use excitation k-space trajectories that do not fully sample k-space, with the same excitation accuracy as a fully-sampled pulse, using sensitivity blurring to push energy out into untraversed regions. Because the transmit sensitivity patterns are smoothly-varying, they blur energy locally in k-space, so we accelerate trajectories by undersampling them relative to the desired field-of-view (FOV). Figure 1.3 shows examples of spiral and echo-planar (EP) trajectories with different FOV's. Trajectories with smaller FOV's have larger gaps between visited k-space locations in one or more dimensions, into which energy is blurred by the sensitivity patterns, so that a pattern can be excited using an undersampled trajectory with the same accuracy as when using a fully-sampled trajectory. Because we have traded traversal of these regions by the k-space trajectory for the instantaneous blurring effect of the coil sensitivities, the pulses along the undersampled trajectories will be shorter in duration. This is the fundamental mechanism underlying parallel excitation.

1.4.1 Applications of Parallel Excitation

This section is based on materials from Ref. [17]

General Multi-dimensional RF Pulse Acceleration

Compared to multidimensional excitation with a single coil, parallel RF excitation with localized coils allows for a reduction of pulse length. The reduction comes from the use of an undersampled (and therefore short-duration) k-space trajectory with an excitation FOV (XFOV) that is smaller than the FOV of the desired pattern. In analogy to parallel imaging, we can characterize the reduction by a *speedup factor*, defined as the ratio of the FOV of the desired pattern to the XFOV of the undersampled trajectory. High excitation accuracy can be maintained over a range of speedup factors in parallel excitation, as demonstrated

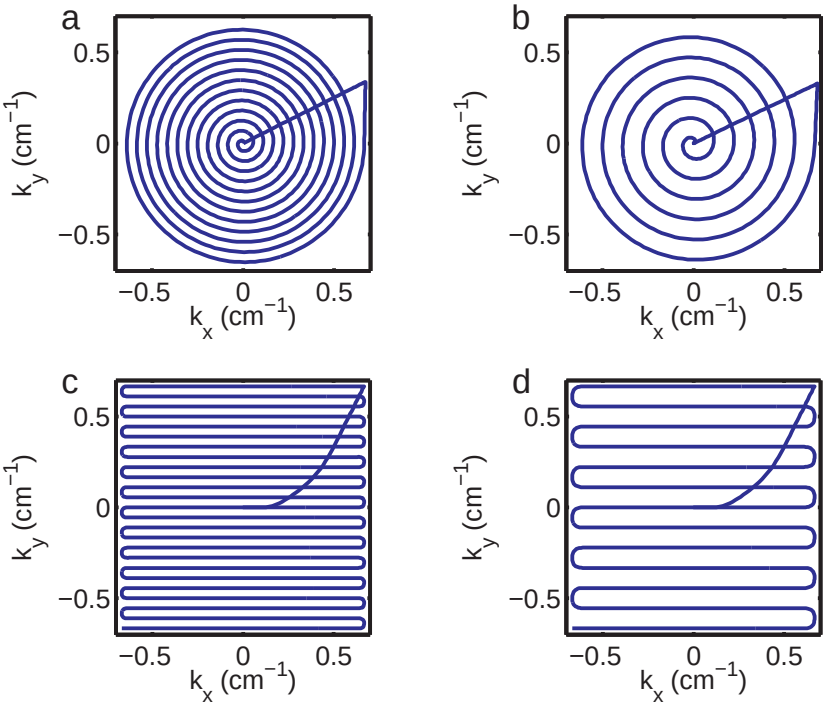

Figure 1.3: (a) A spiral trajectory with FOV = 18 cm, duration 5.1 ms. (b) A spiral trajectory with FOV = 9 cm, duration 2.8 ms. The spiral of (b) has a shorter duration due to wider gaps between rungs in the radial direction. In parallel excitation, multiple coils are used with a reduced trajectory such as (b), and the blurring effect of localized transmit sensitivities is exploited to push energy out into regions not traversed by the trajectory. (c) A fully sampled EP trajectory with FOV = 18 cm, duration 19.8 ms. (b) An EP trajectory with FOV = 9 cm, duration 10.6 ms.

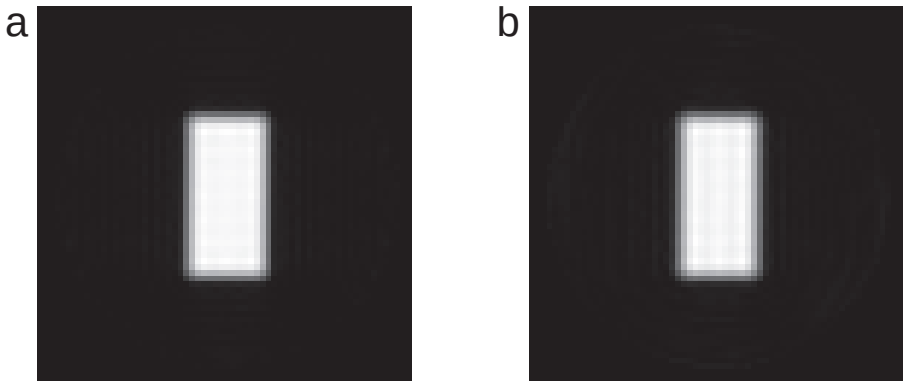

Figure 1.4: Simulation of eight-channel parallel excitation without acceleration (a), and with a speedup factor of 4 (b). The desired pattern was a rectangular block of uniform 10° flip angle, centered in a circular ROI. Spiral excitation k-space trajectories were used with pulse lengths 6.7ms and 2ms. The pulses achieved the same excitation accuracy within the ROI, NRMSE = 0.003.

in Fig. 1.4, which shows simulated images corresponding to no acceleration (Fig. 1.4a), and a speedup factor of 4 (Fig 1.4b). The parallel excitation simulation assumed an eight-channel head transmit array, and both pulse sets were designed to excite a rectangular block of flip angle 10 degrees inside a circular region-of-interest (ROI), using spiral trajectories with different XFOV. From these images and their corresponding excitation error it is evident that excitation accuracy is maintained despite a reduction in pulse length from 6.7ms to 2ms.

B_1^+ Inhomogeneity Compensation

The problem of B_1^+ inhomogeneity in MRI at high fields is well known [18, 19]. Zhang et al [20] have recently proposed that application of parallel excitation to the shortening of multi-dimensional selective excitation pulses for B_1^+ inhomogeneity compensation. Parallel excitation is well-suited to this problem because B_1^+ inhomogeneity is captured as a feature of the measured transmit sensitivity patterns. Thus a homogeneous excitation may be achieved with RF pulses designed using these sensitivity patterns and a homogeneous desired excitation pattern. Figure 1.5b shows an experimental image obtained

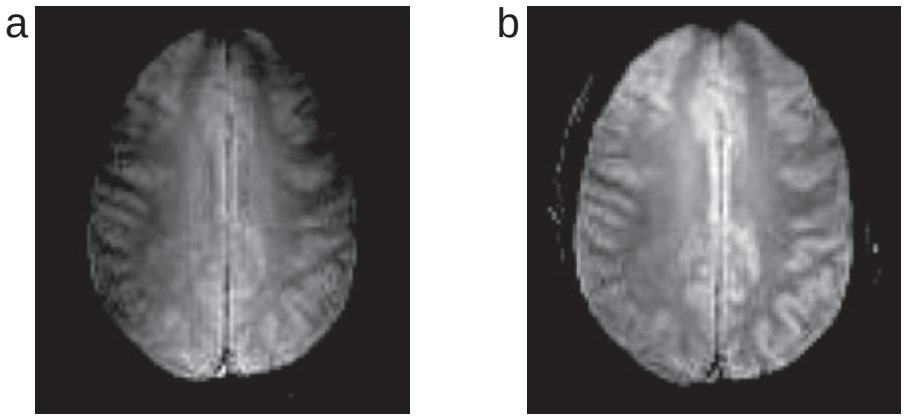

Figure 1.5: Standard slice-selective excitation using multiple transmitters (a) and parallel excitation for B_1^+ inhomogeneity compensation (b) at 3T. In (a), B_1^+ inhomogeneity has the effect of creating a central region of high intensity. In (b), a more homogeneous excitation is achieved. Images courtesy of V.A. Stenger.

at 3T that demonstrates the use of parallel excitation for B_1^+ inhomogeneity compensation. Pulses in this experiment were designed using a 'fast-k_z' trajectory [15] and the spatial domain method we describe in Chapter II. The experiment was performed using the pseudo-parallel excitation method described in Chapter II and Ref [21]. It can be seen that parallel excitation using these pulses results in a more homogeneous excitation (Fig 1.5b) than excitation using a standard slice-selective excitation with multiple transmit coils (Fig 1.5a).

SAR Management

Zhu [2] has shown that parallel excitation can be employed for the purpose of SAR management, which is of great concern at high field strengths. In a given parallel excitation experiment, assuming that the speedup factor is less than the number of coils, the parallel RF pulse design problem is underdetermined, i.e., there are extra degrees of freedom in pulse design that can be exploited to optimize other metrics while maintaining high excitation accuracy. One such metric of practical interest is a measure of SAR,

which could be employed to favor pulses with low average SAR. For example, in a discrete setting, for a given vector $\boldsymbol{b}$ of RF pulse samples, SAR may be quantified as:

$$SAR_{ave} = \boldsymbol{b}'\boldsymbol{F}\boldsymbol{b}. \tag{1.38}$$

The matrix $\boldsymbol{F}$ in Eq. 1.38 relates the RF pulse samples to the squared absolute value of the electric fields in the sample, and is based on the application of the quasi-static approximations to Maxwell's equations, whereby it may be assumed that the electric field in the sample volume scales linearly with the applied current in the coils. Such a metric might be employed in an optimization-based RF pulse design process by enforcing a maximum allowable norm-squared excitation error, while minimizing with respect to average SAR. Zhu [2] reported a 38% decrease in average SAR between RF pulses designed by minimizing excitation error alone and pulses designed with a maximum SAR constraint, for a nine-channel transmit array with a speedup factor of 4.

1.5 Current Approaches to Small-tip-angle Parallel Excitation Pulse Design

This section is based on materials from Ref. [17]

Several methods exist for the design of small-tip-angle RF pulses in parallel excitation [1, 2, 22]. The pioneering pulse design methods were introduced by Katscher et al [1], and Zhu [2]. These were followed by our method [23], and a method introduced by Griswold et al [22]. Our method will be visited in Chapter II. We now provide a brief review of the other methods.

1.5.1 Frequency-Domain Method (Transmit SENSE)

The method introduced by Katscher et al, dubbed transmit SENSE [1], is characterized by the explicit use of transmit sensitivity patterns in the pulse design process, and its formulation is based on a convolution in excitation k-space. It allows usage of arbitrary

k-space trajectories. Consider the case of parallel excitation with R coils, each of which is driven by an independent RF pulse waveform $b_r(t)$, and produces an excitation pattern $p_r(\boldsymbol{x})$. Assuming all pulses excite small-tip-angles, the total excitation pattern produced by playing them simultaneously is given by a linear superposition of their excitation patterns:

$$p(\boldsymbol{x}) = \sum_{r=1}^{R} s_r(\boldsymbol{x})\, p_r(\boldsymbol{x}), \tag{1.39}$$

where $s_r(\boldsymbol{x})$ is coil r's transmit sensitivity pattern. To derive the transmit SENSE method, we first Fourier transform (1.39) to the k-space domain, in which the multiplications $s_r(\boldsymbol{x})\, p_r(\boldsymbol{x})$ become convolutions:

$$\tilde{p}(\boldsymbol{k}) = \sum_{r=1}^{R} \tilde{s}_r(\boldsymbol{k}) \otimes \tilde{p}_r(\boldsymbol{k}), \tag{1.40}$$

where $\tilde{s}_r(\boldsymbol{k})$ is the Fourier transform of coil r's sensitivity pattern, $\tilde{p}_r(\boldsymbol{k})$ is the Fourier transform of coil r's excitation pattern, and the operator $\otimes$ denotes a convolution. This equation can be discretized in $\boldsymbol{k}$, forming a length-N_s vector $\tilde{\boldsymbol{p}}$ that contains samples along a fully sampled grid $\{\boldsymbol{k}_s\}_{s=1}^{N_s}$, R circulant convolution matrices $\tilde{\boldsymbol{S}}_r$ of size $N_s \times N_t$, and R length-N_t vectors $\tilde{\boldsymbol{p}}_r$ containing samples along a common accelerated k-space trajectory $\{\boldsymbol{k}_t\}_{t=1}^{N_s}$. There are no restrictions placed on the choice of the fully-sample grid and the accelerated trajectory, though for simplicity the fully-sampled grid $\{\boldsymbol{k}_s\}_{s=1}^{N_s}$ is generally Cartesian. The circulant convolution matrices $\tilde{\boldsymbol{S}}_r$ may be constructed by computing the discrete Fourier transform of the measured transmit sensitivity patterns, and interpolating each onto a grid of points given by $(\boldsymbol{k}_s - \boldsymbol{k}_t)$. The result of the discretization procedure is a sum of matrix/vector products given by:

$$\tilde{\boldsymbol{p}} = \sum_{r=1}^{R} \tilde{\boldsymbol{S}}_r \tilde{\boldsymbol{p}}_r. \tag{1.41}$$

We may replace the summation in Eq. 1.41 by concatenating the R convolution matrices to form a size-$N_s \times RN_t$ matrix $\tilde{\boldsymbol{S}}_{full}$, and concatenating the transforms of the excitation

patterns, resulting in the length-RN_t vector $\tilde{\boldsymbol{p}}_{full}$:

$$\tilde{\boldsymbol{p}} = \begin{bmatrix} \tilde{\boldsymbol{S}}_1 & \cdots & \tilde{\boldsymbol{S}}_R \end{bmatrix} \begin{bmatrix} \tilde{\boldsymbol{p}}_1 \\ \vdots \\ \tilde{\boldsymbol{p}}_r \end{bmatrix} = \tilde{\boldsymbol{S}}_{full}\tilde{\boldsymbol{p}}_{full}. \tag{1.42}$$

Using this expression, a regularized least-squares cost function can be defined and minimized to yield the Fourier transforms of the individual coils' excitation patterns:

$$\hat{\tilde{\boldsymbol{p}}}_{full} = \underset{\tilde{\boldsymbol{p}}_{full}}{\operatorname{argmin}} \left\{ \left\| \tilde{\boldsymbol{S}}_{full}\tilde{\boldsymbol{p}}_{full} - \tilde{\boldsymbol{p}}_{des} \right\|^2 + R\left(\tilde{\boldsymbol{p}}_{full}\right) \right\}, \tag{1.43}$$

where $\tilde{\boldsymbol{p}}_{des}$ is a length-N_s vector containing samples of the Fourier transform of the desired excitation pattern, and $R\left(\tilde{\boldsymbol{p}}_{full}\right)$ denotes a general regularization term that can be used to control peak and integrated RF power [1]. The vector of RF pulse samples for coil r, $\hat{\boldsymbol{b}}_r$, can be derived from $\hat{\tilde{\boldsymbol{p}}}_r$ by multiplication with the Jacobian determinant for k-space density and velocity compensation [1]. As will be shown in Chapter II, our spatial-domain pulse design method is most closely related to this method, and even produces identical pulses under certain conditions. However, we will also show that our method has several practical advantages.

1.5.2 Removal-of-aliasing Method

The method introduced by Zhu [2] makes explicit use of transmit sensitivity patterns, but is formulated as an optimization problem in the spatial domain. In this method, one considers the aliasing pattern in the spatial domain that results from undersampling the excitation k-space trajectory, and solves for the necessary excitation patterns for each coil. It is assumed that the k-space trajectory is undersampled in one dimension by a speedup factor that is equal to $FOV/XFOV$, the ratio of a field-of-view that covers the object to the field-of-view of the excitation k-space trajectory. Because the method is based on the removal of spatial-domain aliasing, aliases must be coherent and regular, which restricts

the method to Cartesian echo-planar trajectories. For example, consider the case of a two-dimensional Cartesian excitation trajectory that is undersampled in the y-dimension. The aggregate excitation pattern can be expressed as:

$$m(x,y) = \sum_{r=1}^{R} s_r(x,y) \sum_{j=-\infty}^{\infty} m_r(x, y - jXFOV), \tag{1.44}$$

where $m_r(x,y)$ is pattern excited by the r-th coil using the fully-sampled trajectory. Because $XFOV < FOV$, undesired replicates of the excited patterns will be placed within the field-of-view. Now, consider excitation patterns of the form $m_r(x,y) = h_r(x,y)\, m_{des}(x,y)$. Substituting this form into Eq. 1.44 and re-arranging gives:

$$m(x,y) = \sum_{j=-\infty}^{\infty} m_{des}(x, y - jXFOV) \sum_{r=1}^{R} h_r(x, y - jXFOV)\, s_r(x,y). \tag{1.45}$$

We can see that the excited pattern can be made equal to the desired pattern if, over the field-of-view, the following holds true:

$$\sum_{r=1}^{R} h_r(x, y - jXFOV)\, s_r(x,y) = \begin{cases} 1, & j = 0 \\ 0, & \text{otherwise} \end{cases} \tag{1.46}$$

In words, the excited pattern will be equal to the desired one if all but the central replicate of the excitation pattern have zero weight applied to them, where the weight of a given replicate is equal to the sum over coils of the product of each coil's sensitivity pattern at the replicate's position with an additional coil-dependent excitation pattern $h_r(x,y)$. To enforce this equality, we can design $h_r(x,y)$ to satisfy a system of equations within the field-of-view:

$$\begin{bmatrix} s_1(x,y) & \cdots & s_R(x,y) \\ \vdots & & \vdots \\ s_1(x, y + jXFOV) & \cdots & s_R(x, y + jXFOV) \\ \vdots & & \vdots \end{bmatrix} \begin{bmatrix} h_1(x,y) \\ h_2(x,y) \\ \vdots \\ h_R(x,y) \end{bmatrix} = \begin{bmatrix} 1 \\ 0 \\ \vdots \\ 0 \end{bmatrix}, \tag{1.47}$$

which is a system of $FOV/XFOV$ equations with R unknowns (typically $FOV/XFOV \leq R$). Least-squares solutions to Eq. 1.47 can be obtained via pseudo-inverse or other methods, yielding the appropriate excitation pattern for each coil, $m_r(x,y) = h_r(x,y)\, m_{des}(x,y)$, which can then be used to calculate the RF pulse along the accelerated trajectory using the excitation k-space perspective under the small-tip-angle approximation.

It should be noted that this formalism is very similar to the solution of the receive SENSE problem using an undersampled Cartesian trajectory [3]. Similar to SENSE, the number of equations 1.47 can be less than $FOV/XFOV$ at spatial locations, where, due to object shape, there exist fewer than $FOV/XFOV$ replicas overlapping. Likewise, if a more complex undersampling pattern is used (for example, in three-dimensional parallel excitation), then a more complex pattern of overlapping aliases can be incorporated into this expression, albeit leading to larger matrices to be inverted.

1.5.3 Transmit GRAPPA

Griswold et al [22] proposed a k-space domain method that is analogous to GRAPPA imaging. Compared to other parallel pulse design methods, it is unique in that it does not require prior determination of sensitivity patterns. Instead, it involves an extra calibration step in the pulse design process. It also appears to be restricted to echo-planar k-space trajectories that are accelerated via undersampling in one dimension by a speedup factor equal to the ratio $FOV/XFOV$. In addition, the method is based on the assumption that a relatively uniform transmit (B_1^+) field may be produced via simultaneous excitation on all coils. For example, this may require that, for a circular array of transmit coils, the default coil phase varies with angular position so as to produce an approximation to circular polarization. The method begins with an initial 2D RF pulse, designed using the excitation k-space perspective, that produces a desired pattern $m_{des}(\boldsymbol{x})$ using a fully-sampled k-space trajectory and uniform transmit sensitivity. Considering the aforementioned as-

sumption of a uniform B_1^+ field when using all coils, the desired pattern $m_{des}(\boldsymbol{x})$ can be excited by playing out the initial pulse on all coils simultaneously. The initial pulse can be decomposed into its undersampled parts by taking every $FOV/XFOV = C$-th line in excitation k-space:

$$b(k_x, k_y) = \sum_{c=1}^{C} b^c(k_x, k_y). \tag{1.48}$$

Let $m_r^c(x, y)$ be the pattern excited by the r-th coil with the pulse corresponding to the c-th k-space segment $b^c(k_x, k_y)$ and let the aggregate pattern for all coils produced by simultaneous excitation along the c-th k-space segment be $m^c(x, y) = \sum_{r=1}^{R} m_r^c(x, y)$. It follows that the combined excitation along all segments and across all coils will produce the desired excitation pattern:

$$m_{des}(x, y) = \sum_{c=1}^{C} m^c(x, y). \tag{1.49}$$

The basic idea behind transmit GRAPPA is to determine what weighted combination of RF pulses, transmitted along a single k-space segment (e.g., $c = 1$), will excite m_{des}.

More specifically, the design method will attempt to determine what RF pulses for each of the coils, transmitted along segment $c = 1$, will produce the other segments' excitation patterns, $m^c(x, y), c = 2, \ldots, C$. Thus, the $m^c(x, y)$ represent the *targets* of the parallel excitation scheme and are half of the required calibration data for transmit GRAPPA. These target patterns, $m^c(x, y)$, are determined experimentally by transmitting pulse segment b^c via all coils simultaneously. This acquisition is repeated for excitation along all segments $c = 2, \ldots, C$. Next, calibration data representing the *building blocks* for exciting $m^c(x, y)$ must also be obtained. As a matter of convenience, one can choose the first segment of the initial pulse b^1 as the building block. By exciting this pulse individually on each of the R coils, one can acquire $m_r^1(x, y), r = 1, \ldots, R$, which form the other half of the required calibration data. If necessary, one can excite a richer set of building

blocks, the use of which may yield a more accurate fit to the target k-space data. Finally, the relationship between the segment-1 excitation patterns $m_r^1(x,y)$ and the target patterns $m^c(x,y)$ is determined to build the final RF pulses. In practice, this relationship is examined in the k-space domain and, in a manner analogous to receive GRAPPA, a linear combination of RF pulses from the individual coils (the building blocks) with shifts in k-space form the pulses that produce the pattern for each target segment, $m^c(x,y)$.

The final RF pulses will be in the form:

$$\tilde{b}_r = \sum_{c=1}^{C} \tilde{b}_r^c, \tag{1.50}$$

where $\tilde{b}_r^c, r = 1,\ldots,R$ is the set of RF pulses that, when transmitted simultaneously along segment 1, will produce the excitation pattern for segment c, i.e., $m^c(x,y)$. By Eq. 1.49, simultaneous excitation with $\tilde{b}_r, r = 1,\ldots,R$ will produce m_{des}. The subpulses $\tilde{b}_r^c$ are constructed from weighted combinations of shifted versions of the *building block* RF pulse:

$$\tilde{b}_r^c(k_x,k_y) = \sum_{p,q} a_r^c(p,q)\, b^1(k_x - p\Delta k, k_c - qC\Delta k), \tag{1.51}$$

where p and q are integer shifts that map out a neighborhood in excitation k-space, Δk are the fundamental k-space shifts, and $a_r^c(p,q)$ are the GRAPPA coefficients. In analogy with receive GRAPPA, the underlying assumption is that the transmit patterns blur the RF pulse energy into neighboring lines in k-space. The GRAPPA coefficients are determined by finding the coefficients that best fit the following relationship:

$$M^c(k_x,k_y) = \sum_{r=1}^{R}\sum_{p,q} a_r^c(p,q)\, M_r^1(k_x - p\Delta k, k_c - qC\Delta k), \tag{1.52}$$

where M^c and M_r^1 are the acquired k-space data associated with the calibration excitation patterns $m^c, c = 2,\ldots,C$ and $m_r^1, r = 1,\ldots,R$, respectively. Thus, the coefficients that are used to construct the *target* RF pulses from the *building block* RF pulses are obtained from a fitting procedure that is performed on images of the excitation patterns that

the target and building block pulses produce. The method therefore obviates the need for estimates of transmit sensitivity patterns, because they are manifest in the linear transformation from RF pulses to excitation patterns. Interestingly, while the shifts in (1.51) are in excitation k-space and the shifts in (1.52) are in acquisition k-space, these shifts are the same provided the field of view of the acquired data and the initial fully-sampled RF pulse is the same. Thus, only a few acquisition lines are necessary to determine the transmit GRAPPA coefficients.

1.6 Current Approaches to Large-Tip-Angle Parallel Excitation Pulse Design

Pulse design is more challenging at large-tip-angles, due to non-linearity of the Bloch equation. Many techniques exist for large-tip-angle one-dimensional pulse design that extend readily to parallel excitation, such as simulated annealing [24] and optimal control [25]. To date, three approaches have been reported for large-tip-angle pulse design. The first was a method by Ulloa et al [26] that optimizes the complex weights applied to a series of sinc pulses along a fast-k_z trajectory [27], using a global search routine and the Bloch equation. An improvement to this method was proposed by Setsompop et al [28], who showed that Powell optimization [29] could be used to reduce computation time. Neither of these methods are gradient-based. Xu et al [30] proposed an extension of the one-dimensional optimal control pulse design [25] algorithm to the parallel case. This gradient-based method has been shown to be robust, and does not require pulse parameterization. Because we will compare our fast parallel optimal control method to this method in Chapter IV, we review its derivation here.

Instead of deriving the optimal control algorithm for the Bloch equation directly, we will derive it for a generic one-dimensional problem and then make appropriate substitu-

tions. Consider a linear system defined by the differential equation

$$\dot{x} = f\left[u\left(t\right), x\left(t\right), t\right], \tag{1.53}$$

where $u\left(t\right)$ is a "control", such as an RF pulse. Suppose we have an initial condition $x\left(0\right)$, and we wish to design $u\left(t\right)$ to drive x to a desired end-state at time T. We can define a cost function for this problem:

$$J\left(u\left(t\right)\right) = \phi\left(x\left(T\right)\right) + \int_0^T L\left(u\left(t\right)\right) dt, \tag{1.54}$$

where ϕ is an error function that measures the distance between $x\left(T\right)$ and the desired end-state, and L is a differentiable penalty function, such as Tikhonov regularization, chosen to discourage large values of some characteristic of the control $u\left(t\right)$. We begin by adjoining the differential equation governing $x\left(t\right)$ to the cost function using the Lagrange multiplier function $\lambda\left(t\right)$,

$$\bar{J} = \phi\left(x\left(T\right)\right) + \int_0^T L\left(u\left(t\right)\right) + \lambda^T\left(t\right)\left\{f\left[u\left(t\right), x\left(t\right), t\right] - \dot{x}\right\} dt. \tag{1.55}$$

Integrating $\lambda^T\left(t\right)\dot{x}$ by parts yields

$$\begin{aligned}\bar{J} = \phi\left(x\left(T\right)\right) - \lambda^T\left(T\right)x\left(T\right) + \lambda^T\left(0\right)x\left(0\right) + \\ + \int_0^T L\left(u\left(t\right)\right) + \lambda^T\left(t\right)f\left[u\left(t\right), x\left(t\right), t\right] + \dot{\lambda}^T\left(t\right)x\left(t\right) dt.\end{aligned} \tag{1.56}$$

Our desire is to find the stationary point of $\bar{J}$. Consider perturbations in $\bar{J}$ due to perturbations in $u\left(t\right)$. Perturbations in $\bar{J}$ depend on perturbations in $u\left(t\right)$ both explicitly, and implicitly through $x\left(t\right)$:

$$\begin{aligned}\delta\bar{J} = \left[\left(\frac{\partial\phi}{\partial x} - \lambda^T\right)\delta x\right]_{t=T} + \left[\lambda^T\delta x\right]_{t=0} + \\ + \int_0^T \left[\frac{\partial L}{\partial u} + \lambda^T\frac{\partial f}{\partial u}\right]\delta u + \left(\lambda^T\frac{\partial f}{\partial x} + \dot{\lambda}^T\right)\delta x dt.\end{aligned} \tag{1.57}$$

It would be difficult to determine perturbations $\delta x\left(t\right)$ produced by $\delta u\left(t\right)$, so we *choose* $\lambda\left(t\right)$ to cause the coefficients if $\delta x\left(t\right)$ to vanish. This will occur if:

$$\dot{\lambda}^{T}=-\lambda^{T}\left(t\right)\frac{\partial f}{\partial x}, \tag{1.58}$$

$$\lambda^{T}\left(T\right)=\frac{\partial\phi}{\partial x\left(T\right)}. \tag{1.59}$$

With these definitions substituted into Eq. 1.57, $\delta\bar{J}$ becomes

$$\delta\bar{J}=\left[\lambda^{T}\delta x\right]_{t=0}+\int_{0}^{T}\left(\frac{\partial L}{\partial u}+\lambda^{T}\frac{\partial f}{\partial u}\right)\delta u dt. \tag{1.60}$$

Because the initial state $x\left(0\right)$ is independent of the control, $\delta x\left(0\right)=0$, and we are left with:

$$\delta\bar{J}=\int_{0}^{T}\left(\frac{\partial L}{\partial u}+\lambda^{T}\frac{\partial f}{\partial u}\right)\delta u dt. \tag{1.61}$$

At a stationary point, $\delta\bar{J}$ will be 0 for arbitrary δu. This occurs if:

$$\frac{\partial L}{\partial u}+\lambda^{T}\frac{\partial f}{\partial u}=0,\qquad 0\leq t\leq T. \tag{1.62}$$

To summarize, to determine $u\left(t\right)$ at a stationary point of $\bar{J}$, we can equivalently determine the $u\left(t\right)$ that satisfies Eq. 1.62, where λ satisfies Eqs. 1.58 and 1.59 and x satisfies Eq. 1.53, with $x\left(0\right)$ given. To solve this problem iteratively, we can use an initial guess $u^{i}\left(t\right)$ to integrate x forward and λ backward using Eqs. 1.53 and 1.58, and then set

$$u^{i+1}\left(t\right)=u^{i}\left(t\right)-\mu\left[\lambda^{T}\frac{\partial f}{\partial u^{i}}+\frac{\partial L}{\partial u^{i}}\right]. \tag{1.63}$$

To see why this will decrease $\bar{J}$, if μ is sufficiently small, the perturbation made to δu^{i} will produce a perturbation in $\bar{J}$ of:

$$\delta\bar{J}=-\mu\int_{0}^{T}\left[\lambda^{T}\frac{\partial f}{\partial u^{i}}+\frac{\partial L}{\partial u^{i}}\right]^{2}dt\leq 0, \tag{1.64}$$

so $\bar{J}$ will decrease.

Now, in the parallel excitation case, we have the cost function

$$\Psi\left(b_1,\ldots,b_R\right)=\frac{1}{2}\left\|\bar{\boldsymbol{m}}_{des}-\bar{\boldsymbol{m}}\left(T;b_1,\ldots,b_R\right)\right\|_{\boldsymbol{W}}^2+\frac{\beta}{2}\sum_{r=1}^{R}\left\|b_r\right\|^2, \tag{1.65}$$

where $\bar{\boldsymbol{m}}$ is a vector of length-$3N_s$ that contains the stacked $\boldsymbol{m}=\left(m_x,m_y,m_z\right)^T$ vectors for each spatial location, and N_s is the number of spatial locations over which the desired pattern is specified. The size-$3N_s\times 3N_s$ diagonal weighting matrix $\boldsymbol{W}$ can be used to specify an ROI, or to design pulses on a subset of the three magnetization components, m_x, m_y, and m_z. Compared to (1.54), the first term in (1.65) replaces ϕ, and the second term replaces the integrated penalty term. At each spatial location $\boldsymbol{x}$, $\boldsymbol{m}$ satisfies the Bloch equation for parallel excitation:

$$\dot{\boldsymbol{m}}=\gamma\begin{pmatrix}0 & \boldsymbol{G}\left(t\right)\cdot\boldsymbol{x} & -\Im\left\{b_{tot}\left(\boldsymbol{x},t\right)\right\}\\ -\boldsymbol{G}\left(t\right)\cdot\boldsymbol{x} & 0 & \Re\left\{b_{tot}\left(\boldsymbol{x},t\right)\right\}\\ \Im\left\{b_{tot}\left(\boldsymbol{x},t\right)\right\} & -\Re\left\{b_{tot}\left(\boldsymbol{x},t\right)\right\} & 0\end{pmatrix}\boldsymbol{m}, \tag{1.66}$$

where $b_{tot}\left(\boldsymbol{x},t\right)=\sum_{r=1}^{R}s_r\left(\boldsymbol{x}\right)b_r\left(t\right)$. We then separate the matrix components to obtain

a sum of matrices that are weighted by the real and imaginary parts of the RF:

$$
\begin{aligned}
(1.67)\quad \dot{\boldsymbol{m}} = \gamma & \begin{pmatrix} 0 & \boldsymbol{G}(t)\cdot\boldsymbol{x} & 0 \\ -\boldsymbol{G}(t)\cdot\boldsymbol{x} & 0 & 0 \\ 0 & 0 & 0 \end{pmatrix} \boldsymbol{m} + \\
& + \gamma \sum_{r=1}^{R} \begin{pmatrix} 0 & 0 & -\Im\{s_r(\boldsymbol{x})\} \\ 0 & 0 & \Re\{s_r(\boldsymbol{x})\} \\ \Im\{s_r(\boldsymbol{x})\} & -\Re\{s_r(\boldsymbol{x})\} & 0 \end{pmatrix} \boldsymbol{m}\Re\{b_r(t)\} + \\
& + \gamma \sum_{r=1}^{R} \begin{pmatrix} 0 & 0 & -\Re\{s_r(\boldsymbol{x})\} \\ 0 & 0 & -\Im\{s_r(\boldsymbol{x})\} \\ \Re\{s_r(\boldsymbol{x})\} & \Im\{s_r(\boldsymbol{x})\} & 0 \end{pmatrix} \boldsymbol{m}\Im\{b_r(t)\} \\
& = \gamma\boldsymbol{\Omega}(\boldsymbol{x},t)\,\boldsymbol{m} + \gamma \sum_{r=1}^{R} \boldsymbol{S}^{r}_{real}(\boldsymbol{x})\,\boldsymbol{m}\Re\{b_r(t)\} + \gamma \sum_{r=1}^{R} \boldsymbol{S}^{r}_{imag}(\boldsymbol{x})\,\boldsymbol{m}\Im\{b_r(t)\}.
\end{aligned}
$$

To combine all spatial locations into one equation, we stack the length-3 vectors $\dot{\boldsymbol{m}}$ and $\boldsymbol{m}$ and form block-diagonal matrices from the size-3×3 matrices $\boldsymbol{\Omega}(\boldsymbol{x},t)$, $\boldsymbol{S}^{r}_{real}(\boldsymbol{x})$, and

$\boldsymbol{S}^r_{imag}(\boldsymbol{x})$, yielding:

$$\dot{\bar{\boldsymbol{m}}} = \gamma \begin{pmatrix} \boldsymbol{\Omega}(\boldsymbol{x}_1,t) & \dots & 0 \\ \vdots & \ddots & \vdots \\ 0 & \dots & \boldsymbol{\Omega}(\boldsymbol{x}_{N_s},t) \end{pmatrix} \bar{\boldsymbol{m}} + \tag{1.68}$$

$$+\gamma \sum_{r=1}^{R} \begin{pmatrix} \boldsymbol{S}^r_{real}(\boldsymbol{x}_1) & \dots & 0 \\ \vdots & \ddots & \vdots \\ 0 & \dots & \boldsymbol{S}^r_{real}(\boldsymbol{x}_{N_s}) \end{pmatrix} \bar{\boldsymbol{m}} \Re\{b_r(t)\} +$$

$$+\gamma \sum_{r=1}^{R} \begin{pmatrix} \boldsymbol{S}^r_{imag}(\boldsymbol{x}_1) & \dots & 0 \\ \vdots & \ddots & \vdots \\ 0 & \dots & \boldsymbol{S}^r_{imag}(\boldsymbol{x}_{N_s}) \end{pmatrix} \bar{\boldsymbol{m}} \Im\{b_r(t)\}$$

$$= \gamma \bar{\bar{\boldsymbol{\Omega}}}(t)\bar{\boldsymbol{m}} + \gamma \sum_{r=1}^{R} \bar{\bar{\boldsymbol{S}}}^r_{real} \bar{\boldsymbol{m}} \Re\{b_r(t)\} + \gamma \sum_{r=1}^{R} \bar{\bar{\boldsymbol{S}}}^r_{imag} \bar{\boldsymbol{m}} \Im\{b_r(t)\} \quad .$$

We are now in a position to define the optimal control algorithm for parallel excitation pulse design. At each iteration i, we simulate the current set of pulses $\{b^i_1(t), \dots, b^i_R(t)\}$ using a Bloch simulator to obtain $\bar{\boldsymbol{m}}$ for $0 \le t \le T$. We then perform a reverse Bloch simulation to obtain the stacked (length-$3N_s$) Lagrange multiplier vector, $\bar{\boldsymbol{\lambda}}^T$, for $0 \le t \le T$, with the boundary condition

$$\bar{\boldsymbol{\lambda}}^T(T) = \left(\bar{\boldsymbol{m}}(T; b_1, \dots, b_R) - \bar{\boldsymbol{m}}_{des}\right)^T \boldsymbol{W}. \tag{1.69}$$

We then update the pulses. The update for the real part of the pulse for coil r will have the form:

$$\Re\left\{b^{i+1}_r(t)\right\} = \Re\left\{b^i_r(t)\right\} - \mu\left[\gamma \bar{\boldsymbol{\lambda}}^T(t)\, \bar{\bar{\boldsymbol{S}}}^r_{real} \bar{\boldsymbol{m}}(t) + \beta \Re\left\{b^i_r(t)\right\}\right]. \tag{1.70}$$

It is interesting to note that we could also arrive at this update equation by applying gradient descent directly to the cost function (1.65).

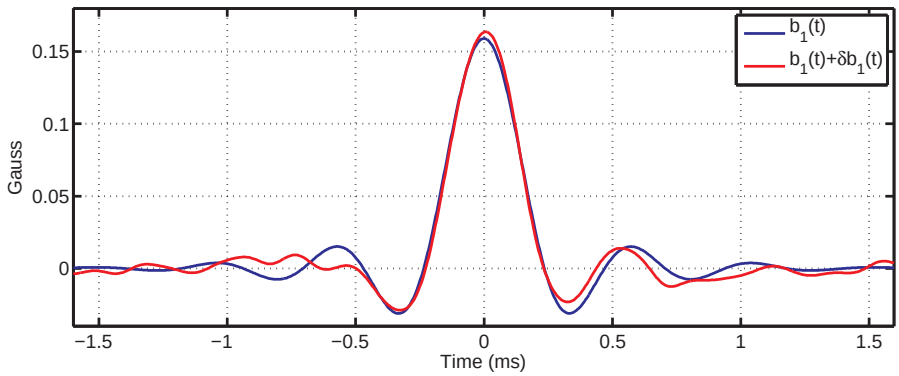

Figure 1.6: A large-tip-angle pulse $b_1(t)$, and a perturbed pulse $b_1(t) + \delta b_1(t)$. In subsequent chapters, we introduce fast multidimensional large-tip-angle pulse design algorithms that employ linear models for the difference between the excitation patterns produced by the two pulses.

1.7 Our Approach to Large-Tip-Angle Parallel Excitation Pulse Design

In the previous section, we reviewed current methods for large-tip-angle parallel RF pulse design. These methods either require unacceptably long computation times, or achieve reduced computation times by parameterizing the pulses to be designed. Previous to this research project, there were no existing 'fast' methods for multi-dimensional large-tip-angle RF pulse design, in either parallel or conventional excitation. In the large-tip-angle regime, the Bloch equation is nonlinear, so magnetization responds nonlinearly to an applied RF pulse, and the k-space formalism that enables Fourier-based small-tip-angle pulse design methods breaks down.

In Chapters III and IV we introduce two 'fast' parallel large-tip pulse design methods that achieve large reductions in compute time compared to previous methods, without requiring pulse parameterization. The approaches that these methods take to accelerating pulse computation can be unified under a single idea that we introduce here. Consider a large-tip-angle RF pulse $b_1(t)$, such as that shown in Fig. 1.6. The magnetization state following the application of this pulse can be represented as a nonlinear function of it, $\boldsymbol{F}$,

that is the solution to the Bloch equation:

$$\boldsymbol{m}(\boldsymbol{x}, T) = \boldsymbol{F}(b_1(t); \boldsymbol{m}_0(\boldsymbol{x})). \tag{1.71}$$

Now, consider a scenario in which $b_1(t)$ is perturbed via the addition of a pulse $\delta b_1(t)$, where $\delta b_1(t)$ is of small magnitude (Fig. 1.6). While the magnetization state following the application of $b_1(t) + \delta b_1(t)$ will again be a nonlinear function of it, it is reasonable to expect that the difference between the magnetization state following the application of $b_1(t)$ alone, and that following $b_1(t) + \delta b_1(t)$ will be small, and possibly well-modelled by a linear function. Therefore, in this project we make linear approximations to the Bloch equation solution for $b_1(t) + \delta b_1(t)$ of the form:

$$\boldsymbol{m}(\boldsymbol{x}, T) + \delta\boldsymbol{m}(\boldsymbol{x}, T) \approx \boldsymbol{F}(b_1(t); \boldsymbol{m}_0(\boldsymbol{x})) + \boldsymbol{L}(\delta b_1(t); b_1(t), \boldsymbol{m}_0(\boldsymbol{x})), \tag{1.72}$$

where $\boldsymbol{L}$ is a linear function of $\delta b_1(t)$, and $\delta\boldsymbol{m}(\boldsymbol{x}, T)$ is the perturbation in the final magnetization state created by the addition of $\delta b_1(t)$ to $b_1(t)$. The difference between the methods of Chapters III and IV lies in their choice of $\boldsymbol{L}$. Both will use exact Bloch simulations of $b_1(t)$ to obtain $\boldsymbol{m}(\boldsymbol{x}, T)$, and both will use Fourier-like choices of $\boldsymbol{L}$, to enable fast computation. There are alternative approaches to linearizing the Bloch equation; we previously implemented a time-segmentation scheme that breaks up a large-tip-angle RF pulse into small time segments, over which excitation is approximated as linear [31]. The drawback to that approach is that the error associated with each segment's approximation is compounded when combined with those of the others', resulting in a model of insufficient accuracy. The approach described here has been much more successful.

1.8 Contributions

The contributions made in this research project are:

1: A novel small-tip-angle pulse design method. To improve upon current methods, the new method is model-based, applies to general excitation k-space trajectories, allows compensation for off-resonance and other non-idealities, and permits fast computation using non-uniform fast Fourier transforms. We test this methods in simulation and experiments.

2: Using simulation studies, an exploration of the performance of small-tip-angle-designed parallel excitation pulses at large-tip-angles. We identify causes for degraded performance of parallel pulses compared to single-channel pulses, and opportunities to improve large-tip-angle performance of parallel pulses.

3: An exploration of new approximations to the Bloch equation that facilitate fast RF large-tip-angle pulse design. We seek approximations that lead to linear, Fourier relationships between RF pulses and the magnetization or flip angle pattern excited by those pulses.

4: Two novel large-tip-angle pulse design methods that make use of linear approximations to the Bloch equation. These are general, fast methods. We test them in simulations and single-channel experiments involving excitation, inversion, and refocusing pulse designs. We compare the new methods to conventional large-tip-angle parallel pulse design methods. Because the new methods are based on linear approximations, they are evaluated for robustness to design parameters.

CHAPTER II

Small-tip-angle parallel RF pulse design

2.1 Introduction

In this chapter we propose a parallel RF pulse design method that is closely related to transmit SENSE [1], but is formulated in the spatial domain. It is a multi-coil generalization of the iterative pulse design method proposed by Yip et al [9], and is based on the minimization of a quadratic cost function that consists of an excitation error term, which quantifies excitation error in the spatial domain, and a choice of regularization terms. The regularization terms may be used to control the integrated and peak RF power. The minimization problem may be solved iteratively via the conjugate gradient (CG) method [12], or via brute-force inversion. We demonstrate that the new approach is approximately equivalent to [1] under special conditions, but it has several new advantages. It allows for spatially variant excitation error weighting and thus region of interest (ROI) specification. Main field inhomogeneity is easily incorporated in the design. Unlike [1], it does not require computation of a Jacobian determinant for compensation of k-space velocity and density, nor does it require interpolation between excitation k-space trajectories. It also enables fast pulse computation using the Conjugate Gradient algorithm with non-uniform fast Fourier transform's [14].

To date, all RF pulse design methods for parallel excitation are based on the assump-

This chapter is based on materials from Ref. [23].

tion of small-tip-angle excitation. Beyond the small-tip-angle regime, it is expected that the non-linearity of the Bloch equation will have an adverse effect on the performance of pulses designed using these methods. Because it is often desirable to use large-tip-angle pulses, we investigated the behavior, in terms of excitation error, of pulses designed using the proposed spatial domain method as they are scaled to produce relatively large tip angles, up to 90. We also investigated the utility of Tikhonov regularization on integrated pulse power [9] in mitigating this error.

In the following section we formulate small-tip-angle RF pulse design for multi-coil parallel excitation in the spatial domain as an optimization problem. We then present Bloch equation simulation results that show quantitatively the benefits of the proposed method, in terms of excitation accuracy, at high speedup factors or when off resonance is present. We then present results of our investigation into the large-tip-angle behavior of pulses designed using the spatial domain method. Finally, we present experimental results using a method we developed that exploits the linearity of small-tip-angle excitation and the MR signal equation to swap the roles of transmitters and receivers.

2.2 Theory

The spatial domain design approach is an extension of the single-coil iterative RF pulse design method introduced by Yip et al [9]. Assuming small tip angles, the transverse plane excitation pattern produced by a single coil can be approximated by the Fourier integral of an excitation k-space trajectory (10), $\boldsymbol{k}(t) = \begin{bmatrix} k_x(t) & k_y(t) & k_z(t) \end{bmatrix}$, weighted by a complex RF pulse $b(t)$ and spatially weighted by the coils complex transmit sensitivity $s(\boldsymbol{x})$:

$$m(\boldsymbol{x}) \approx i\gamma m_0 s(\boldsymbol{x}) \int_0^T b(t)\, e^{i\gamma \Delta B_0(\boldsymbol{x})(t-T)} e^{i\boldsymbol{x}\cdot\boldsymbol{k}(t)} dt, \tag{2.1}$$

where γ is the gyromagnetic ratio, m_0 is the equilibrium magnetization magnitude, T is the pulse length, and $e^{i\gamma\Delta B_0(\boldsymbol{x})(t-T)}$ represents the phase accrued due to main field inhomogeneity defined by the field map $\Delta B_0(\boldsymbol{x})$. The trajectory $\boldsymbol{k}(t)$ is defined as the time-reversed integration of the gradient waveforms [7]. Exploiting linearity in the small-tip-angle regime, the excitation patterns from multiple coils can be spatially superposed to form an aggregate pattern:

$$m(\boldsymbol{x}) \approx i\gamma m_0 \sum_{r=1}^{R} s_r(\boldsymbol{x}) \int_0^T b_r(t)\, e^{i\gamma\Delta B_0(\boldsymbol{x})(t-T)} e^{i\boldsymbol{x}\cdot\boldsymbol{k}(t)} dt, \tag{2.2}$$

where R is the number of transmit coils, each with sensitivity pattern $s_r(\boldsymbol{x})$ and unique RF pulse $b_r(t)$. Discretizing time to N_t samples and space to N_s samples, we may write:

$$\boldsymbol{m} = \sum_{r=1}^{R} \boldsymbol{D}_r \boldsymbol{A} \boldsymbol{b}_r, \tag{2.3}$$

where $\boldsymbol{m}$ is the length-N_s vector of spatial samples of the aggregate excitation pattern, $\boldsymbol{D}_r = diag\{s_r(\boldsymbol{x}_i)\}$ is a diagonal matrix containing samples of the sensitivity pattern of coil r, and $\boldsymbol{b}_r$ is a length-N_t vector of RF pulse samples for coil r. The (i,j)-th element of the $N_s \times N_t$ system matrix $\boldsymbol{A}$ is given by:

$$a_{ij} = i\gamma m_0 \Delta t e^{i\gamma\Delta B_0(\boldsymbol{x}_i)(t_j-T)} e^{i\boldsymbol{x}_i\cdot\boldsymbol{k}(t_j)}. \tag{2.4}$$

Equation 2.4 can be rewritten via horizontal concatenation of the matrices $\boldsymbol{D}_r\boldsymbol{A}$ and vertical concatenation of the vectors $\boldsymbol{b}_r$, resulting in:

$$\boldsymbol{m} = \begin{bmatrix} \boldsymbol{D}_1\boldsymbol{A} & \cdots & \boldsymbol{D}_R\boldsymbol{A} \end{bmatrix} \begin{bmatrix} \boldsymbol{b}_1 \\ \vdots \\ \boldsymbol{b}_R \end{bmatrix} = \boldsymbol{A}_{full}\boldsymbol{b}_{full}. \tag{2.5}$$

Given a vector $\boldsymbol{m}_{des}$ containing N_s samples of a desired pattern at the spatial locations $\boldsymbol{x}_i$, the RF pulses can be designed via solving the following minimization problem:

$$\hat{\boldsymbol{b}}_{full} = \underset{\boldsymbol{b}_{full}}{\operatorname{argmin}} \left\{ \|\boldsymbol{A}_{full}\boldsymbol{b}_{full} - \boldsymbol{m}_{des}\|_{\boldsymbol{W}}^2 + R(\boldsymbol{b}_{full}) \right\}, \tag{2.6}$$

where $\boldsymbol{W}$ is an $N_s \times N_s$ diagonal matrix containing a spatial error weighting that one can use to specify spin-free regions as "dont-care" regions, and $R\left(\boldsymbol{b}_{full}\right)$ denotes a general regularization term that is a function of the RF samples. Integrated RF power may be controlled via a Tikhonov regularization term $R\left(\boldsymbol{b}_{full}\right) = \beta \boldsymbol{b}'_{full}\boldsymbol{b}_{full}$, where prime denotes complex conjugate transpose, and β is a tuning parameter. As shown later in this work, this term is useful for mitigating increased excitation error when RF pulses are scaled to achieve large tip angles. Peak RF power may be controlled via $R\left(\boldsymbol{b}_{full}\right) = \boldsymbol{b}'_{full}\boldsymbol{\Lambda}\boldsymbol{b}_{full}$, where $\Lambda = diag\left(\lambda_j\right)$, with λ_j, $j = 0, \ldots, R \cdot N_t - 1$ denoting regularization parameters used to control the magnitude of individual RF pulse samples [9]. The minimization problem can be solved by brute-force inversion or efficiently by the CG method, in a manner similar to the single-coil pulse design method proposed in [9].

In the special case in which a field map is not incorporated in the system matrix, error weighting is not specified, and Tikhonov regularization is used, our proposed method and the frequency domain approach of transmit SENSE [1] are approximately equivalent (see Appendix). However, in general, our method offers the extra advantages of region-of-interest (ROI) specification via the $\boldsymbol{W}$ matrix, and better system modeling via field map incorporation in the system matrix $\boldsymbol{A}$, which improve excitation accuracy. Computation is also reduced compared to the frequency domain method because there is no need in our method to transform the desired pattern and sensitivity patterns to the frequency domain, nor does it require computation of a Jacobian determinant for k-space sampling density and velocity compensation, or interpolation between k-space trajectories.

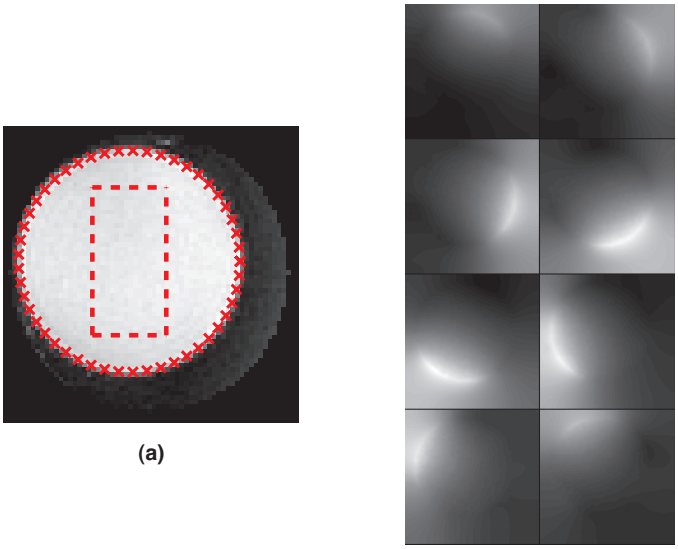

(a) (b)

Figure 2.1: (a) The ROI mask (dashed circle) for NRMSE calculation and pulse design was obtained by thresholding the body coil image of a phantom. The desired excitation pattern (dashed rectangle) was centered in the ROI, of uniform tip angle, zero phase, and dimensions 5×10 cm. (b) Receive coil sensitivity patterns (magnitude) of an 8-channel head array, as measured on a spherical phantom. These patterns are used in the numerical simulations of parallel excitation.

2.3 Methods

2.3.1 Pulse Design

RF pulses were computed in MATLAB 7.0.4 (MathWorks, Inc., Natick, MA), on a 2.0 GHz Pentium 4 computer with 1 Gb of RAM, using the CG algorithm initialized with a zero pulse and run for 60 iterations [9, 12]. Except in Simulation III, no Tikhonov regularization was used. In all cases, a single-shot spiral-out excitation k-space trajectory was used with the following parameters: maximum amplitude = 4 G/cm, maximum slew rate = 18000 G/cm/s, and sampling period 4 μs. To accelerate excitation, we used trajectories that radially undersampled k-space, resulting in reduction of the excitation field of view (XFOV) of individual coils excitation patterns. We define *speedup factor* as the ratio of the FOV of the desired pattern to the reduced XFOV of the individual coils excitation patterns. This convention is adopted because, regardless of k-space trajectory used, acceleration in

parallel excitation is always achieved via undersampling in the FOV dimension. Alternative definitions, such as the ratio of unaccelerated and accelerated pulse lengths, would make performance comparisons across k-space trajectories more difficult, as the savings in pulse length would be specific to the trajectory used and the hardware on which they are implemented. k-space trajectories were chosen to achieve a spatial resolution of 0.625 cm. The desired excitation pattern (Fig. 3.1a) was a 5×10 cm rectangle of uniform tip angle (magnitude 0.1, corresponding to tip angle of 6°) and zero phase. The pattern was defined on a 64×64 Cartesian grid in a 20×20 cm region.

To obtain transmit sensitivity patterns, we estimated the receive sensitivity patterns (Fig. 3.1b) of an 8-channel head coil array (MRI Devices), and make the assumption that the resulting patterns represent reasonable transmit sensitivity patterns, though perhaps not exactly those of the head array coil used. The sensitivity patterns were estimated by imaging a spherical phantom with a Gradient Echo (GRE) spiral sequence with a slice-selective sinc pulse, using both the head coil array and the body coil. The head coil array images were divided by the body coil image, and then smoothed in an iterative penalized least-squares fashion, as described in [32], to yield the final sensitivity patterns. Nonzero coil sensitivity outside the phantom can be attributed to the smoothing operation in the sensitivity estimation process. The body coil image was thresholded (at 0.3 of its maximum magnitude) to derive an ROI (Fig. 3.1a) that defined a spatial error weighting function in which the care region had error weighting 1, and the dont care region outside the ROI had error weighting 0.

2.3.2 Numerical Simulations

We performed Bloch equation simulations to test pulse design methods. Simulations were performed over a 128×128 transverse grid covering a 20×20 cm region. Relaxation effects were ignored. Normalized root-mean-square excitation error (NRMSE)

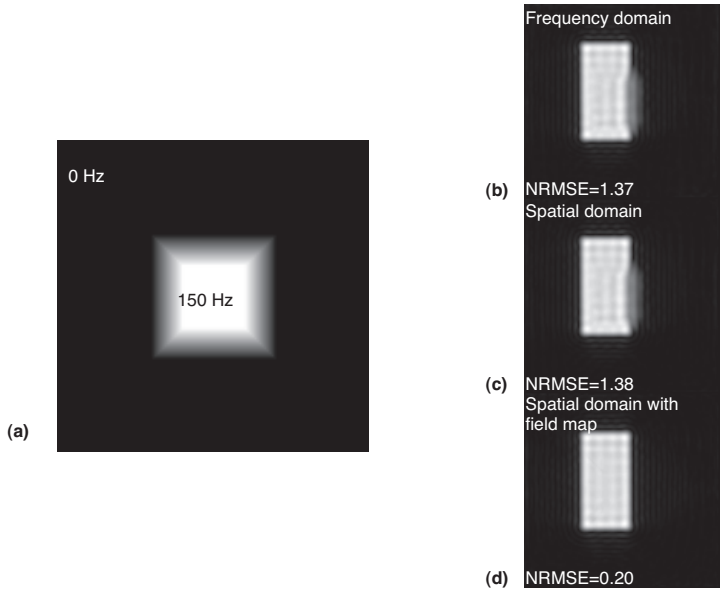

Figure 2.2: (a) Field map used in simulation of off-resonance correction. The magnitude of the center flat region (white) is 150 Hz, while the outer region (black) is 0 Hz. (b,c,d) Excitation patterns resulting from pulses designed using a speedup factor of 2, corresponding to an XFOV of 10 cm and a 3.8 ms RF pulse length. Note the distortion on the right side of the excitation pattern resulting from frequency domain-designed pulses (b) and spatial domain-designed pulses without field map incorporation (c) at this peak off resonance.

was calculated for each result from the Bloch simulator ($\boldsymbol{m}_{bl}$). It was defined as $\|\boldsymbol{m}_{bl} - \boldsymbol{d}_{bl}\|_{\boldsymbol{W}_{bl}} / \|\boldsymbol{d}_{bl}\|_{\boldsymbol{W}_{bl}}$, where $\boldsymbol{d}_{bl}$ and $\boldsymbol{W}_{bl}$ are the desired pattern and error weighting interpolated to the Bloch simulation grid, respectively. The ROI for NRMSE calculation was the same as that used in pulse design. Transmit sensitivity patterns used in simulation were also obtained via interpolating those used in pulse design.

Simulation I: off resonance correction

In simulation I we evaluated our design methods ability to correct for off resonance during excitation. In the Bloch simulator, we incorporated a field map with flat regions in the center (+150 Hz) and background (0 Hz), bridged by a linear transition region (Figure 2.2a). The frequency offset of the center region represents a typical field map value at 3T. We compared the performance of our method *with* and *without* field map incorporation to the performance of pulses designed with the frequency domain method of transmit

SENSE [1], in terms of NRMSE within the ROI. The applied spiral trajectory radially undersampled k-space, yielding a speedup factor of 2 and a pulse length of 3.8 ms.

Simulation II: speedup factor

In simulation II we tested our design methods performance as a function of speedup factor, *with* and *without* ROI specification, and compared this to the performance of pulses designed with the frequency domain method. NRMSE was calculated over the ROI. The speedup factor was varied from one, corresponding to no reduction in XFOV, to twenty, corresponding to a twenty-fold reduction in XFOV. As speedup factor was incremented from 1 to 20, pulse length was reduced from 6.9 ms to 0.25 ms.

Simulation III: tip angle

In this simulation we studied the relationships between speedup factor, Tikhonov regularization, and excitation accuracy of RF pulses at large tip angles. For a given speedup factor and Tikhonov regularization parameter value β, RF pulses were designed using our spatial domain method with ROI specification. The pulses were then scaled to alter the tip angle achieved, and simulated in the Bloch simulator. We calculated the average tip angle inside the resulting excited block, and NRMSE inside the ROI with respect to a desired pattern that was scaled to the calculated average tip angle. This process was repeated over a range of speedup factors, scaling factors, and regularization parameter values.

2.3.3 Scanner Experiments

We employed an experimental method based on a rearrangement of the MR signal equation to validate our pulse design method on the scanner [21]. Exploiting linearity in the small-tip regime, we swapped the roles of the non-uniform transmit sensitivity patterns of the transmit coil array with the uniform receive sensitivity pattern of the body coil in the signal equation. Neglecting off-resonance and T1 and T2 decay, the signal received during

readout subsequent to small-tip parallel excitation is given by a substitution of Equation 2.2 into the MR signal equation:

$$s(t) \approx \int \left\{ i\gamma m_0(\boldsymbol{x}) \sum_{r=1}^{R} s_r(\boldsymbol{x}) \int_0^T b_r(t') e^{i\boldsymbol{x}\cdot\boldsymbol{k}_t(t')} dt' \right\} e^{i\boldsymbol{x}\cdot\boldsymbol{k}_r(t)} d\boldsymbol{x}, \tag{2.7}$$

where $s_r(\boldsymbol{x})$ is coil r's transmit sensitivity pattern, and $\boldsymbol{k}_t(t)$ and $\boldsymbol{k}_r(t)$ are the transmit and receive k-space trajectories, respectively. This equation can be rearranged, bringing the summation over coils outside of the signal integral:

$$s(t) \approx \sum_{r=1}^{R} \left[\int s_r(\boldsymbol{x}) \left\{ i\gamma m_0(\boldsymbol{x}) \int_0^T b_r(t') e^{i\boldsymbol{x}\cdot\boldsymbol{k}_t(t')} dt' \right\} e^{i\boldsymbol{x}\cdot\boldsymbol{k}_r(t)} d\boldsymbol{x} \right]. \tag{2.8}$$

The resulting equation demonstrates that, in the case of linear small-tip excitation, the signal received subsequent to simultaneous transmission is equivalent to the signal obtained via serial transmission using each transmit coil driven in isolation, followed by a summation of the resulting signals offline, where the isolated-transmit signals are represented in Equation 2.8 by the quantity inside the square brackets. Furthermore, the signal $s(t)$ is equivalent to that obtained via serial transmission using a volume coil with uniform transmit sensitivity and reception using receive coils with sensitivity patterns $s_r(\boldsymbol{x})$, where the excited pattern is represented in Equation 2.8 by the quantity inside the curly braces. Thus, in this experiment we make use of the body coil for transmission and a head array coil for reception. The experiment proceeds as follows: the head arrays receive sensitivity patterns are measured, and are used in the design of the parallel excitation pulses. The RF pulse designed for coil r is then played out on the body coil, and coil r is used for reception to produce an image. The process is repeated for all coils in the array, and assuming linearity under the small-tip-angle approximation, the resulting imaged excitation patterns are added together offline to obtain the final combined excitation pattern. Assuming that the receive sensitivity patterns $s_r(\boldsymbol{x})$ are equivalent to the transmit sensitivity patterns of some hypothetical transmit array, this method is equivalent to parallel transmission using

such a transmit array. In general, this approach may not produce transmit patterns that are realizable in arbitrary objects, but it does allow for testing of the pulse design method. The procedure is useful for validating pulse design methods without requiring parallel transmit hardware that is still in the early stages of development.

We performed scanner experiments on a GE 3T Signa Excite Scanner (GE Healthcare, Milwaukee, WI), using a spherical homogeneous copper sulfate phantom. ROI, field map, and sensitivity patterns were determined from images acquired using a gradient-echo (GRE) spiral-out sequence. A spin-echo (SE) spiral-out pulse sequence was used to image excitation patterns, in which the slice selective sinc pulse was replaced by the parallel excitation pulse. Slice selection was performed by the 180-degree pulse. Imaging parameters for all sequences were as follows: slice thickness = 4.0 mm, FOV = 20 cm; reconstructed matrix size = 64×64; Repetition Time (TR) = 2 s; Echo Time (TE) = 40 ms (SE), 20 ms (GRE). Four acquisition interleaves were used in all sequences to reduce readout time, thereby minimizing the effects of off resonance during acquisition. In both experiments, tip angles of patterns being compared were matched by normalizing parallel excitation pulses by the same value that ensured flip angles did not exceed 20 degrees. For the parallel excitation pulses, gradient waveforms for excitation were shifted forward by 150 μs to compensate for delay between RF and gradient channels. Images were reconstructed using a fast implementation of the off-resonance compensated conjugate phase method [33]. It used field maps estimated from two images acquired with a TE difference of 0.25 ms [34].

Experiment I: off resonance correction

This experiment validated the spatial domain methods ability to correct for distortion due to off resonance during excitation. Three small ferromagnetic metal pieces were attached to the phantom surface to create main field inhomogeneity. With pulse lengths of 3.5ms, 5.2ms and 6.9ms, corresponding to speedup factors of 2, 4/3, and 1, pulses were

designed using the spatial domain method *with* and *without* field map incorporation. The field map was estimated from two GRE images [34], with TE values of 20ms and 20.25ms. We masked the field map with the ROI, and then smoothed it using a regularized weighted least-squares method [32] before incorporation into the design process.

Experiment II: Region of Interest specification

In Experiment II we evaluated the performance of the spatial domain method *with* and *without* ROI specification at high speedup factors. We used a speedup factor of 4, corresponding to a pulse length of 1.8ms and XFOV of 5cm. The resulting excitation patterns were visually compared to evaluate performance in terms of uniformity within the excited block and erroneous excitation in the background.

2.4 Results

2.4.1 Simulation I: off resonance correction

Figure 2.2 shows excitation patterns produced using the frequency domain method and the spatial domain method with and without field map incorporation. It can be seen that pulses designed using the frequency domain method and the spatial domain method without field map incorporation produced distorted excitation patterns in both the transition region and the flat region of the field map, and their corresponding error is much higher than that of the spatial domain method with field map incorporation.

2.4.2 Simulation II: speedup factor

Figure 2.3 contains a plot of the NRMSE vs. speedup factor for the frequency domain method and the spatial domain method with and without ROI specification. All three achieved similar excitation error for speedup factors up to about 4, corresponding to an XFOV of 5 cm. However, the spatial domain method with ROI specification was able to achieve much lower error compared to the frequency domain method and the spatial

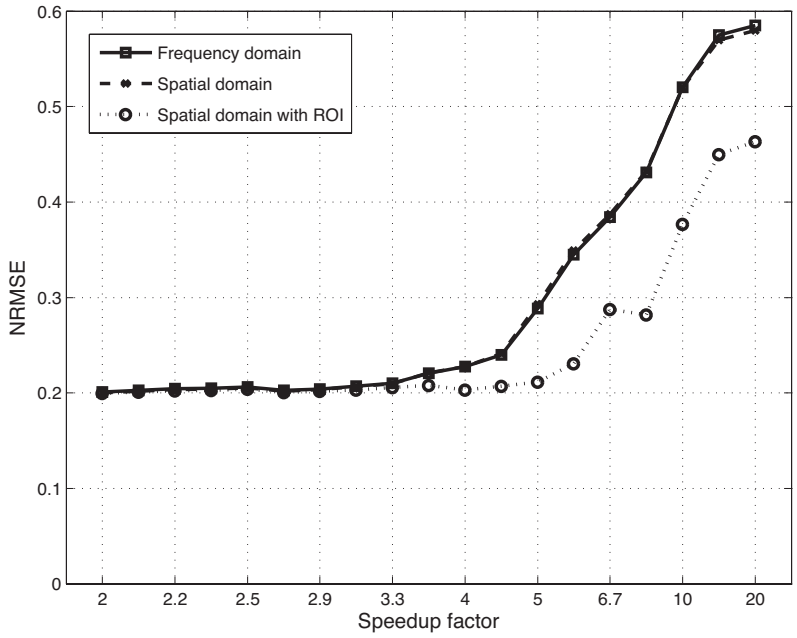

Figure 2.3: Excitation error as a function of speedup factor for the three different pulse design methods. With 8 coils, comparable NRMSE is achieved by the three design methods for speedup factors below 4. For speedup factors above 4, the spatial domain method with ROI specification achieves significantly lower error than the frequency domain method and the spatial domain method without ROI specification.

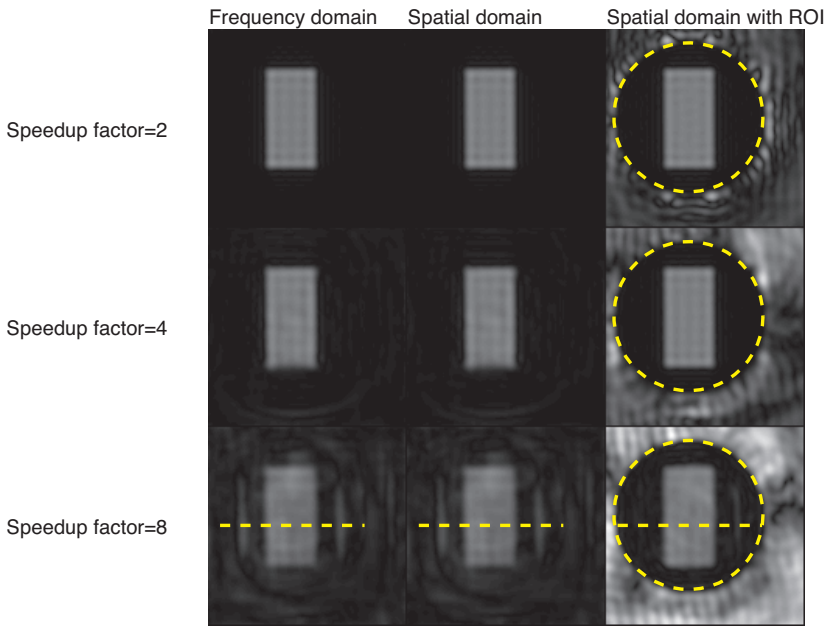

Figure 2.4: Excitation patterns resulting from pulses designed for speedup factors of 8, 4, and 2. A more accurate excitation is achieved by the spatial domain method with ROI specification (indicated by dashed circle) for large speedup factors, while pulses designed using the spatial domain method without ROI specification and the frequency domain method perform similarly over the range of speedup factors. The dashed line indicates the positions of the profiles in Fig. 2.5.

domain method without ROI specification for speedup factors beyond 4. This lower error at high speedup factors for the excitation error-weighted pulses is due to an effective reduction in FOV of the desired excitation pattern via ROI specification. Figure 2.4 shows excitation patterns at speedup factors of 2, 4, and 8. Comparing patterns resulting from pulses designed with and without ROI specification, it is seen that 'aliased' excitation that is pushed outside the desired patterns FOV when ROI specification *is not* used is allowed inside the desired patterns FOV, but outside the ROI, when ROI specification *is* used. The benefit of ROI specification is most visible in the patterns at a speedup factor of 8, where we can see a more accurate excitation pattern resulting from pulses designed with ROI specification than in the other two cases. Figure 2.5 contains profiles through the three methods' excitation patterns at this speedup factor, taken across the narrow dimension of the desired pattern and within the ROI. From this plot it is evident that, compared to the

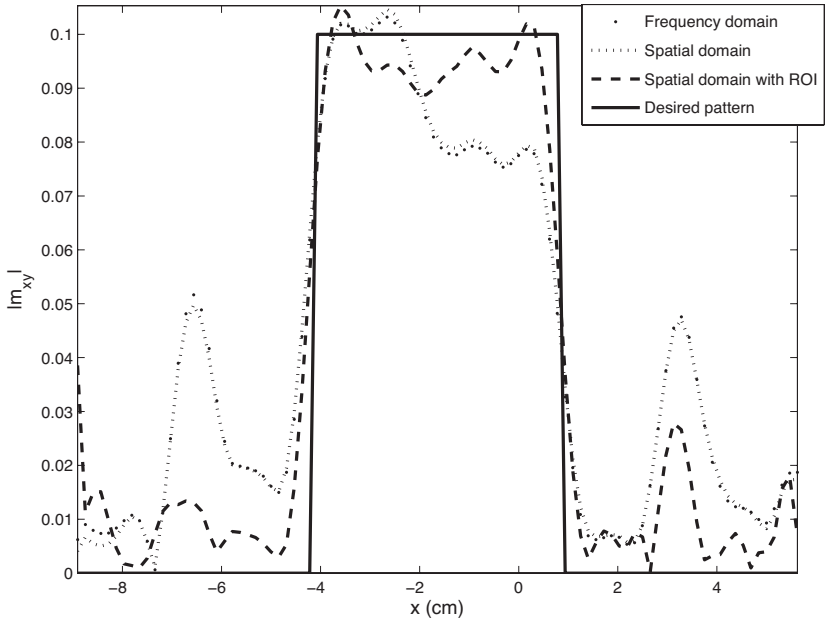

Figure 2.5: Profile through the center of the excitation pattern resulting from pulses designed with speedup factor 8. A more accurate excitation across the block, as well as reduced erroneous excitation outside the block, is achieved by the spatial domain method with ROI specification. Arrows indicate areas where the spatial domain method with ROI specification (dashed arrows) achieved significantly higher accuracy than the frequency domain method and spatial domain method without ROI specification (solid arrows).

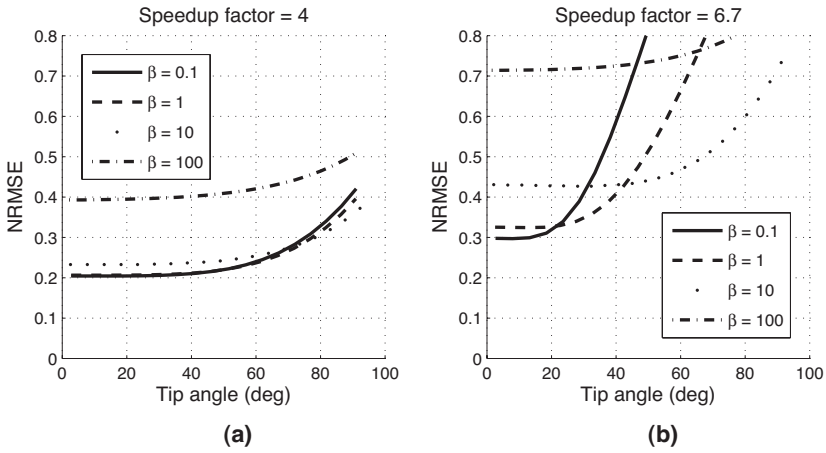

Figure 2.6: Excitation error vs. average tip angle for speedup factors 4 (a) and 6.7 (b). For the lower speedup factor of 4 (a), reasonable excitation accuracy is maintained over a range of tip angles up to $90°$. At a higher speedup factor of 6.7 (b), large-tip-angle performance is heavily degraded. In general, for small-tip-angle excitation, lowest error is achieved using small Tikhonov regularization. As pulses are scaled to achieve larger tip angles, it becomes desirable to design with larger regularization. The advantage of larger regularization at large-tip-angles is more pronounced for high speedup factors (b) than for low speedup factors (a).

other two methods, the spatial domain method with ROI specification results in an excitation pattern that more accurately matches the desired pattern inside and outside the block.

2.4.3 Simulation III: tip angle

Figure 2.6 plots excitation error versus average tip angle for pulses designed with the spatial domain method at speedup factors of 4 (Fig. 2.6a) and 6.7 (Fig. 2.6b). It can be seen that excitation accuracy degrades with increasing tip angle for both speedup factors. However, such performance degradation as a function of increasing tip angle is more rapid at high speedup factors. This is evidenced by the fact that error curves increase much more rapidly for speedup factor 6.7 than for speedup factor 4.

We find that large-tip-angle excitation error can be mitigated, particularly at high speedup factors, by increasing Tikhonov regularization in the pulse design cost function. Large Tikhonov regularization causes pulses with low integrated power to be favored in the

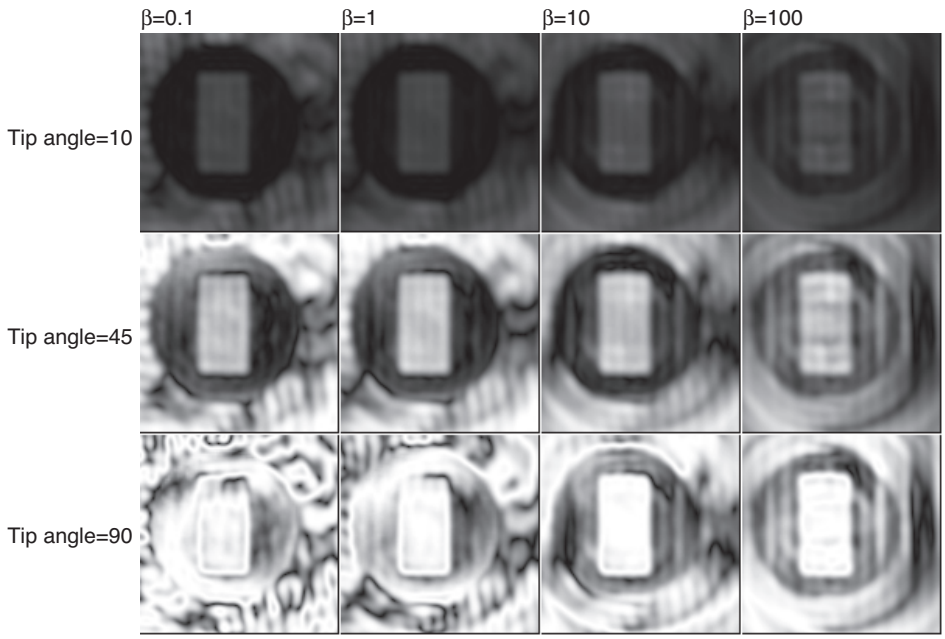

Figure 2.7: Tikhonov regularization parameter vs. tip angle for speedup factor 6.7. Increasing the Tikhonov regularization (β) in the cost function improves excitation accuracy at large tip angles. Tip angles are calculated as the average tip angle over the region corresponding to the desired excitation pattern.

design process over pulses with low small-tip-angle excitation error. The efficacy of Tikhonov regularization is quantified in Figure 2.6. For a relatively small speedup factor of 4 (Fig. 2.6a), Tikhonov regularization has some effect on large-tip-angle excitation accuracy, and it is desirable to use large β when designing for large tip angles. At a higher speedup factor of 6.7 (Fig. 2.6b), the effect of increased Tikhonov regularization is much more pronounced. In this case we see that for small-tip-angle excitation, it is desirable to use small β to achieve low error, however, for these values the error increases drastically with increasing tip angle. For large β, the error is higher at small tip angles, but as pulses are scaled to produce large tip angles, the error curves remain flatter, and excitation error is much lower compared to when small β is used. Figure 2.7 further illustrates this behavior, and shows that for speedup factor 6.7 and small Tikhonov parameter value $\beta = 0.1$, the excitation pattern becomes increasingly distorted as average tip angle increases, to the point

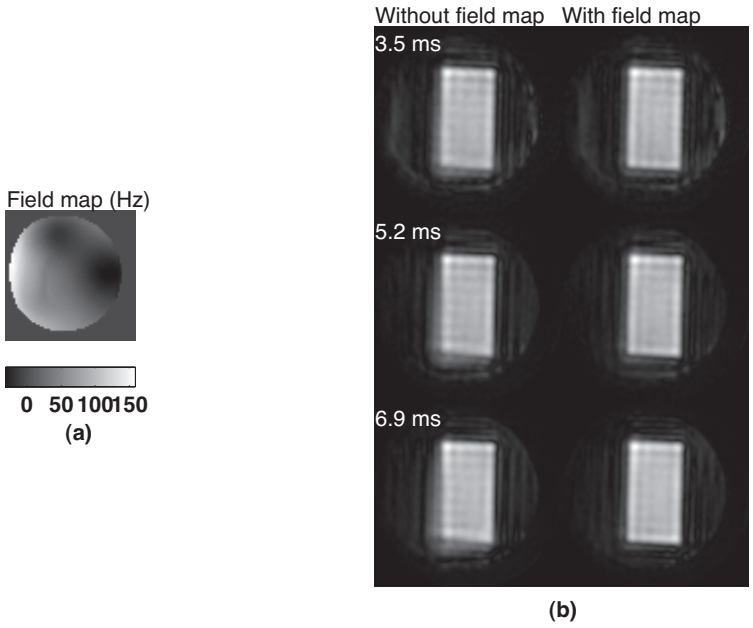

Figure 2.8: Excitation patterns (b) resulting from pulses designed with and without incorporation of a field map (a), for pulse lengths of 3.5 ms (speedup factor 2), 5.2 ms (speedup factor 4/3), and 6.9 ms (speedup factor 1). Pulses designed without field map incorporation yielded excitation patterns with increasing blur with respect to pulse length, while pulses designed with field map incorporation yielded excitation patterns which remained well-defined over all pulse lengths.

of being unrecognizable at $90°$. The erroneous excitation begins to appear around the inner perimeter of the ROI, in areas of high transmit sensitivity pattern magnitude. In contrast, pulses designed with larger β produce patterns with reduced distortion at $90°$, with best accuracy attained using the largest Tikhonov parameter value simulated, $\beta = 100$. For $45°$ tip angle, though, $\beta = 10$ provides the best accuracy, indicating that the best choice of β is a function of tip angle.

2.4.4 Experiment I: off resonance

The estimated field map (Fig. 2.8a) revealed global field distortion caused by the attached metal, with a maximum field offset of 150 Hz occurring in the lower left side of the slice of interest. Fig. 2.8b shows the resulting excitation patterns from pulses designed both with and without off-resonance incorporation in the design, at three different speedup

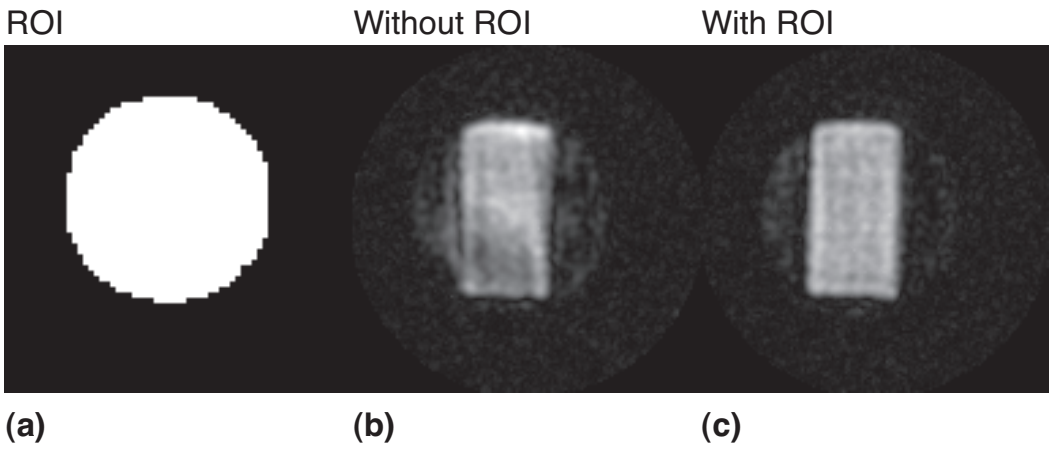

Figure 2.9: (a) ROI defined by thresholding body coil image. (b,c) At a speedup factor of 4, incorporation of ROI (c) resulted in improved uniformity inside the block, and suppressed error in the background, compared to pulses designed without ROI specification (b).

factors of 2, 4/3 and 1, corresponding to pulse lengths of 3.5ms, 5.2ms, and 6.9ms. With increasing pulse length, off-resonance during excitation resulted in excitation patterns with an increasingly distorted and blurred lower left corner when a field map was not incorporated into the design. When a field map is used, however, the definition of the excitation pattern is maintained with increasing pulse length, and erroneous excitation outside the block is reduced due to decreasing speedup factor.

2.4.5 Experiment II: Region of Interest specification

Incorporation of the ROI (Fig. 2.9a) into the design process results in higher excitation accuracy within the ROI. Figure 2.9b shows the excitation patterns resulting from pulses designed with and without ROI specification. The pattern with ROI specification is more uniform over the block, and contains less erroneous excitation around the perimeter of the block. Thus, ROI specification has resulted in a more accurate excitation pattern at this speedup factor of 4.

2.5 Discussion and Conclusions

In this chapter we have presented a spatial domain method for the design of RF pulses in multi-coil parallel excitation and have verified it with both simulations and MR phantom experiments. The new design method is formulated as a minimization problem, in which the resulting RF pulses are the minimizer of a quadratic cost function comprising a weighted norm-squared error term and regularization terms, the latter of which may be used to control the integrated RF power, peak RF power, and waveform smoothness. The minimization problem may be solved iteratively via the conjugate gradient (CG) method, or via brute-force inversion.

In some cases, the new design approach produces RF pulses of similar quality to the frequency domain method of transmit SENSE [1], e.g., in the special case that Tikhonov regularization is used, but neither ROI specification nor main field inhomogeneity compensation are incorporated in the design process. In general, though, it has some important advantages over that method. It allows for a spatially varying excitation error weighting such as region of interest (ROI) specification, which we have shown leads to increased excitation accuracy at high speedup factors. This is because error outside the ROI does not contribute to the norm-squared error term of the design cost function, thereby providing more degrees of freedom to achieve higher excitation accuracy inside the ROI. ROI specification effectively decreases the FOV of the desired excitation pattern, and thus decreases the effective speedup factor. In a given imaging experiment, an ROI can be determined automatically in the pulse design process by thresholding prescan images obtained for sensitivity mapping to yield an ROI corresponding to spatial locations containing tissue. The new design method also allows for compensation of magnetic field inhomogeneities via incorporation of an extra phase term in the design system matrix, which we have shown in

our simulations and experiments increases excitation accuracy in the presence of magnetic field inhomogeneities, by allowing each spatial point to effectively experience a unique k-space trajectory. In Experiment I it was shown that in the presence of field inhomogeneities, the new method maintains excitation accuracy at lower speedup factors, compared to methods that do not account for the effects of off resonance. The method does not require computation of k-space traversal speed and density compensation functions, nor does it require interpolation in the design process, unlike [1]. It enables fast pulse computation using the Conjugate Gradient algorithm with non-uniform fast Fourier transform's [14]. Compared to the design methods proposed in [2,22], the new design approach allows the use of arbitrary k-space trajectories and provides additional design controls. Though not presented here, simulations performed using an EPI trajectory yielded results consistent with those obtained using a spiral trajectory.

We also investigated the behavior, in terms of excitation accuracy, of pulses designed using the proposed method as they are scaled to produce tip angles up to 90°. It was shown that excitation patterns became heavily distorted at these tip angles due to Bloch equation non-linearity, and that the distortion becomes worse as the speedup factor is increased. One interpretation of this result is that at high speedup factors XFOV is small, and each coil plays an increased role in canceling aliased excitation produced by other coils. Thus, the individual coil excitation patterns are less localized, and each coil excites larger tip angles over a larger region of space compared to small speedup factors. As pulses are scaled up, the largest tip angles in the individual coil excitation patterns leave the small-tip-angle regime earliest and fail to combine effectively to cancel aliased excitation, thereby producing the observed distortion. Thus, the linear small-tip-angle assumption that the total tip angle produced by each individual coil commutes with the tip angles produced by the other coils is broken. A second interpretation is lent by the analysis used to derive the linear class

of large-tip-angle pulses [8]. Pulses of this class may be linearly scaled to produce large tip angles, provided that they meet three conditions; namely that the deposition of energy in k-space is Hermitian symmetric, that RF magnitude is approximately zero compared to gradient field magnitude, and that the excitation k-space trajectory may be approximately decomposed into individually refocused trajectories. In our tip angle simulation, k-space energy deposition is approximately Hermitian symmetric, so the first condition is met. However, at high speedup factors in parallel excitation, k-space coverage is sparse which results in increased RF magnitude, so the second approximation becomes inaccurate. Also at high speedup factors the distance between individual spiral arcs increases, so the third approximation also becomes inaccurate. In the simulation we demonstrated the utility of Tikhonov regularization in mitigating increased excitation error at large tip angles and high speedup factors. The demonstrated error behavior with respect to Tikhonov regularization parameter may be understood from the first perspective above by considering that increasing the parameter in the design process causes pulses with low integrated RF power to be favored over those with low norm-squared excitation error. These pulses produce individual coil excitation patterns with smaller tip angles in general, but whose combination still yields the desired average excited tip angle. Because these pulses combine more constructively, they are less susceptible to the adverse effects of Bloch equation non-linearity. Thus, combination and aliased excitation cancellation performance is relatively well maintained as they are scaled to produce large tip angles. From the linear class perspective, Tikhonov regularization results in pulses with lower magnitude, and thus the second approximation is more accurate when it is used. Thus, we conclude that at high speedup factors and large tip angles, it is desirable in terms of excitation error to use a large Tikhonov regularization parameter. Although the appropriate choice of Tikhonov parameter is complicated by the non-linear nature of the effect we wish to mitigate, we

have found that a metric which quantifies the inaccuracy of the second approximation of the linear class formulation can be useful in predicting the accuracy of a given pulse at large tip angles, and may thus serve as a guideline for choosing an appropriate parameter. The metric we have tested is the average, over the pulse duration, of the ratio of instantaneous total RF magnitude (averaged over the sample) to gradient magnitude, and we have found that the larger this metric, the more inaccurate pulses are as they are scaled to large tip angles. One could incorporate this metric into a practical imaging experiment by initially designing pulses with a small Tikhonov regularization parameter, and repeating the pulse design process with larger parameters until the metric falls below a certain safe number, the value of which may be a function of the desired excitation pattern, k-space trajectory, and tip angle. In general, though, while we have shown that acceleration worsens the large tip-angle performance of small-tip-designed pulses, the results presented here are still surprisingly good for a range of speedup factors.

Appendix

The transmit SENSE [1] approach to RF pulse design in parallel excitation is formulated in the frequency, or k-space domain. Assuming small tip angles, the Fourier transform of an excitation pattern $\boldsymbol{m}(\boldsymbol{x})$ resulting from simultaneous excitation by R coils is given by:

$$p(\boldsymbol{k}) = \sum_{r=1}^{R} S_r(\boldsymbol{k}) \otimes p_r(\boldsymbol{k}), \tag{2.9}$$

where S_r is the Fourier transform of the transmit sensitivity pattern of coil r, p_r is the Fourier transform of the excitation pattern produced by coil r, and the operator $\otimes$ denotes a convolution. This equation may be discretized in $\boldsymbol{k}$, forming vectors from p and p_r, and circulant convolution matrices from samples of S_r. A regularized least-squares cost function may then be formed and minimized to yield the Fourier transforms of the individual

coils excitation patterns:

$$
\begin{aligned}
\Psi_{fd}\left(\boldsymbol{p}_{full}\right) &= \|\boldsymbol{S}_{full}\boldsymbol{p}_{full}-\boldsymbol{p}_{des}\|^2+\beta\|\boldsymbol{p}_{full}\|^2, \\
\boldsymbol{p}_{full} &= \begin{bmatrix} \boldsymbol{p}_1 & \cdots & \boldsymbol{p}_R \end{bmatrix}^T, \\
\boldsymbol{S}_{full} &= \begin{bmatrix} \boldsymbol{S}_1 & \cdots & \boldsymbol{S}_R \end{bmatrix}^T,
\end{aligned} \tag{2.10}
$$

where $\boldsymbol{p}_{des}$ is a vector containing samples of the Fourier transform of the desired excitation pattern. The $\boldsymbol{p}_{full}$ that minimizes Equation 2.10 is:

$$
\begin{aligned}
\hat{\boldsymbol{p}}_{full} &= \left(\boldsymbol{S}'_{full}\boldsymbol{S}_{full}+\beta\boldsymbol{I}\right)^{-1}\boldsymbol{S}'_{full}\boldsymbol{p}_{des} \\
&= \boldsymbol{S}'_{full}\left(\boldsymbol{S}_{full}\boldsymbol{S}'_{full}+\beta\boldsymbol{I}\right)^{-1}\boldsymbol{p}_{des},
\end{aligned} \tag{2.11}
$$

where we have used the push-through matrix identity. Thus, for coil r, the minimizing $\boldsymbol{p}_r$ is given by:

$$
\hat{\boldsymbol{p}}_r = \boldsymbol{S}'_r\left(\boldsymbol{S}_{full}\boldsymbol{S}'_{full}+\beta\boldsymbol{I}\right)^{-1}\boldsymbol{p}_{des}. \tag{2.12}
$$

The RF pulse for the r-th coil, $\boldsymbol{b}_r$, can be derived from $\boldsymbol{p}_r$ by multiplication with the Jacobian determinant for k-space density and velocity compensation [1].

The spatial domain and frequency domain methods are approximately equivalent when neither ROI nor magnetic field inhomogeneity compensation are incorporated into the design process, and when Tikhonov regularization that penalizes integrated RF power is used. In this special case, the cost function for the spatial domain method is:

$$
\Psi_{sd}\left(\boldsymbol{b}_{full}\right) = \|\boldsymbol{A}_{full}\boldsymbol{b}_{full}-\boldsymbol{m}_{des}\|^2+\beta\|\boldsymbol{b}_{full}\|^2, \tag{2.13}
$$

and the $\boldsymbol{b}_r$ that minimizes this cost function is given by:

$$
\boldsymbol{b}_r = \boldsymbol{A}'\boldsymbol{D}'_r\left(\boldsymbol{A}_{full}\boldsymbol{A}'_{full}+\beta\boldsymbol{I}\right)^{-1}\boldsymbol{m}_{des}. \tag{2.14}
$$

The matrix product $\boldsymbol{A}_{full}\boldsymbol{A}'_{full}$ is equal to a summation over coils of the product of the diagonal sensitivity matrices $\boldsymbol{D}_r$ with the system matrix $\boldsymbol{A}$, times its conjugate transpose:

$$\boldsymbol{A}_{full}\boldsymbol{A}'_{full} = \sum_{r=1}^{R} \boldsymbol{D}_r \boldsymbol{A}\boldsymbol{A}'\boldsymbol{D}'_r. \tag{2.15}$$

The (j,k)-th element of the matrix $\boldsymbol{A}\boldsymbol{A}'$ is given by:

$$[\boldsymbol{A}\boldsymbol{A}']_{j,k} = \sum_{i=1}^{N_k} e^{i2\pi \boldsymbol{k}_i \cdot (\boldsymbol{x}_j - \boldsymbol{x}_k)}. \tag{2.16}$$

Assuming Cartesian sampling in space, this matrix is Toeplitz, and is approximately circulant [35]. This allows us to write:

$$\boldsymbol{A}\boldsymbol{A}' \approx \boldsymbol{Q}'\boldsymbol{H}\boldsymbol{Q}, \tag{2.17}$$

where $\boldsymbol{H}$ is a diagonal matrix containing samples of the DFT of the first column of $\boldsymbol{A}\boldsymbol{A}'$, and $\boldsymbol{Q}$, $\boldsymbol{Q}'$ are orthonormal forward and inverse DFT matrices, respectively. We may then substitute this expansion into the solution for the RF pulse of coil r. At the same time, we insert DFT matrices on both sides of $\boldsymbol{D}_r$ and on the left of $\boldsymbol{m}_{des}$, which is allowed since $\boldsymbol{Q}'\boldsymbol{Q} = \boldsymbol{I}$, yielding:

$$\boldsymbol{b}_r \approx \boldsymbol{A}'\boldsymbol{Q}'\boldsymbol{Q}\boldsymbol{D}'_r\boldsymbol{Q}'\boldsymbol{Q} \left(\sum_{r=1}^{R} \boldsymbol{D}_r \boldsymbol{Q}'\boldsymbol{H}\boldsymbol{Q}\boldsymbol{D}'_r + \beta \boldsymbol{I} \right)^{-1} \boldsymbol{Q}'\boldsymbol{Q}\boldsymbol{m}_{des}. \tag{2.18}$$

We bring these DFT matrices into the inverse, yielding:

$$\boldsymbol{b}_r \approx \boldsymbol{A}'\boldsymbol{Q}'\tilde{\boldsymbol{S}}'_r \left(\sum_{r=1}^{R} \tilde{\boldsymbol{S}}_r \boldsymbol{H} \tilde{\boldsymbol{S}}'_r + \beta \boldsymbol{I} \right)^{-1} \boldsymbol{Q}\boldsymbol{m}_{des}. \tag{2.19}$$

where $\tilde{\boldsymbol{S}}_r = \boldsymbol{Q}\boldsymbol{D}_r\boldsymbol{Q}'$. The $\boldsymbol{Q}$ on the right side of this expression has the effect of transforming the desired excitation pattern into the frequency domain, and the product $\boldsymbol{A}'\boldsymbol{Q}'$ on the left side has the effect of performing Cartesian to k-space trajectory interpolation and multiplication by the Jacobian determinant. The circulant convolution matrix $\tilde{\boldsymbol{S}}_r$ is defined on a Cartesian grid of frequency locations, and thus the product $\boldsymbol{A}'\boldsymbol{Q}'\tilde{\boldsymbol{S}}'_r$ represents the combined action of the matrix $\boldsymbol{S}'_r$ in Eq. 2.12 and multiplication by the Jacobian

determinant. Furthermore, $\sum_{r=1}^{R} \tilde{\boldsymbol{S}}_r \boldsymbol{H} \tilde{\boldsymbol{S}}_r' \approx \boldsymbol{S}_{full} \boldsymbol{S}_{full}'$, and $\boldsymbol{Q}\boldsymbol{m}_{des} = \boldsymbol{p}_{des}$. Thus this final expression is equivalent to that for the minimizing RF pulse for coil r in the frequency domain method of transmit SENSE [1], under the approximation in Eq. 2.17. This approximate equivalence is established under the special conditions that neither ROI nor main field inhomogeneity compensation are incorporated in the design process, and that Tikhonov regularization is used.

CHAPTER III

Additive angle method for fast large-tip-angle parallel RF pulse design

3.1 Introduction

In Chapter II, we showed that RF pulses designed for accelerated parallel excitation using small-tip-angle methods [1, 2, 22, 23] produce inaccurate excitation patterns when scaled to large-tip-angles [23]. Although unaccelerated pulses designed with small-tip-angle [7] methods can produce accurate large-tip-angle excitation patterns if they satisfy the 'linear-class' conditions [8, 38], at high acceleration factors, increased pulse magnitudes violate the small-RF approximation used to derive the linear class. Several large-tip-angle pulse design methods have recently been proposed specifically for parallel excitation [26, 28, 30]. These methods either suffer from long computation times, or achieve shorter computation times via pulse parameterization, which limits the degrees of freedom in pulse design, and locks the designer into using certain classes of excitation k-space trajectories. The computational bottleneck of most large-tip-angle methods is the Bloch equation, which must be evaluated repeatedly to obtain the magnetization profile subsequent to excitation, and in some methods to calculate the gradient of a cost function with respect to RF pulse samples. In this chapter, we propose a large-tip-angle pulse design method that requires only a small number of Bloch equation simulations, significantly reducing computation time compared to other methods. Furthermore, our method is for-

This chapter is based on materials from Refs. [36] and [37].

mulated as a series of small-tip-angle pulse designs that can be performed rapidly using non-uniform fast Fourier transforms (NUFFT's) [15]. Our method is also simple to implement, using existing software for designing small-tip-angle parallel RF pulses.

The method we propose is based on a series of iterative updates to a large-tip-angle pulse. Initially, a pulse is designed using the small-tip-angle method of Chapter II. This pulse is then simulated using a Bloch equation simulator, and we expect that the flip angle pattern excited by the pulse will deviate significantly from the desired flip angle pattern. A small-tip-angle pulse is then designed to add to the first pulse, to bring the pattern excited by the summed pulses closer to the desired pattern. The summed pulse is seeded to the next iteration, and iterations continue until a convergence criterion is met. In the context of our approach to large-tip-angle pulse design (Section 1.7), this method's choice for the linear function $\boldsymbol{L}$ in Eq. 1.72 is the small-tip-angle equation. We show in simulations and experiments that this method produces $\frac{\pi}{2}$- and π-excitation pulses with significantly improved accuracy over pulses designed using small-tip-angle methods, for both spiral and echo-planar (EP) trajectories.

One-dimensional large-tip-angle RF pulse design methods have been proposed that are similar to the one we present here [39,40]. Ref. [40] proposes an iterative scheme to design large-tip-angle pulses. At each step in the design, the current pulse is Bloch-simulated, and a pulse is designed that adds to the current pulse, to bring the excited pattern closer to the desired one. In [40], the pulses are constrained to be real and time symmetric, to ensure that they all rotate magnetization about the same vector everywhere in space, and as a result their flip angles sum coherently. Our approach differs from this method in that we allow pulses to possess time-varying phase, so the vectors about which the pulses rotate magnetization can vary both spatially and between design iterations, and we employ the Fourier small-tip-angle approximation to accelerate pulse computation. Ref. [39] proposes

an iterative scheme to refine small-tip-angle pulses whose excited patterns are corrupted by scanner imperfections. In that method, pulses are designed using Fourier analysis. Our approach is perhaps most similar to that method, however, we introduce a modification that allows us to design accurate large-tip-angle pulses. Additionally, to our knowledge, this work also represents the first application of this class of pulse design methods to multidimensional pulse design for parallel excitation.

3.2 Theory

Consider parallel excitation pulse design for R coils. Assume we are given N_s samples of a desired tip angle pattern $\theta^{des}(\boldsymbol{x})$ and an initial set of pulses $\{\boldsymbol{b}_1, \ldots, \boldsymbol{b}_R\}$, where $\mathbf{b}_r$ is a length-N_t vector of pulse samples for the rth coil. If $\{\boldsymbol{b}_1, \ldots, \boldsymbol{b}_R\}$ are small-tip-angle pulses, the tip angle pattern they excite at spatial position $\boldsymbol{x}_i$ is well approximated by the extension of Eq. 1.14 to parallel excitation:

$$\theta(\boldsymbol{x}_i)\, e^{i\angle M_{xy}(\boldsymbol{x}_i)} \approx i\gamma\Delta t \sum_{r=1}^{R} s_r(\boldsymbol{x}_i) \sum_{j=1}^{N_t} b_{r,j} e^{i\boldsymbol{x}_i \cdot \boldsymbol{k}(t_j)}, i = 1, \ldots, N_s, \tag{3.1}$$

where $\theta(\boldsymbol{x})$ is the tip angle excited by the pulses, $\angle M_{xy}(\boldsymbol{x})$ is the phase of the resulting transverse magnetization, $s_r(\boldsymbol{x})$ is coil r's transmit sensitivity pattern, and $\boldsymbol{k}(t)$ is the excitation k-space trajectory defined by reverse integration of the gradient waveforms [7]. Further assume that $\{\boldsymbol{b}_1, \ldots, \boldsymbol{b}_R\}$ do not excite $\theta^{des}(\boldsymbol{x})$ accurately, and that the difference between the desired and excited patterns, $\theta^{new}(\boldsymbol{x}) \triangleq \theta^{des}(\boldsymbol{x}) - \theta(\boldsymbol{x})$, is a small-tip-angle pattern. Our goal is to design a new set of pulses $\left\{\tilde{\boldsymbol{b}}_1, \ldots, \tilde{\boldsymbol{b}}_R\right\}$ that, when added to the initial pulse set, results in a set that excites $\theta^{des}(\boldsymbol{x})$. To achieve this, we design $\left\{\tilde{\boldsymbol{b}}_1, \ldots, \tilde{\boldsymbol{b}}_R\right\}$ to satisfy:

$$\theta^{new}(\boldsymbol{x}_i)\, e^{i\angle M_{xy}(\boldsymbol{x}_i)} \approx i\gamma\Delta t \sum_{r=1}^{R} s_r(\boldsymbol{x}_i) \sum_{j=1}^{N_t} \tilde{b}_{r,j} e^{i\boldsymbol{x}_i \cdot \boldsymbol{k}(t_j)}, i = 1, \ldots, N_s, \tag{3.2}$$

where $\angle M_{xy}(\boldsymbol{x})$ is obtained from Eq. 3.1, i.e., it is the transverse phase induced by the initial pulses. Setting

$$d^{new}(\boldsymbol{x}) \triangleq \theta^{new}(\boldsymbol{x})\, e^{i\angle M_{xy}(\boldsymbol{x})}, \tag{3.3}$$

we design $\left\{\tilde{\boldsymbol{b}}_1, \ldots, \tilde{\boldsymbol{b}}_R\right\}$ using the iterative small-tip-angle parallel pulse design method of [23], which will calculate pulses that minimize the cost function:

$$\Psi\left(\tilde{\boldsymbol{b}}_1, \ldots, \tilde{\boldsymbol{b}}_R\right) = \left\| \sum_{r=1}^{R} \boldsymbol{S}_r \boldsymbol{A} \tilde{\boldsymbol{b}}_r - \boldsymbol{d}^{new} \right\|_{\boldsymbol{W}}^2 + \beta \sum_{r=1}^{R} \left\| \boldsymbol{b}_r + \tilde{\boldsymbol{b}}_r \right\|^2, \tag{3.4}$$

where $\boldsymbol{S}_r$ is a diagonal matrix containing samples of $s_r(\boldsymbol{x})$ and $\boldsymbol{A}$ is a non-uniform fast Fourier transform (NUFFT) matrix corresponding to $e^{i\mathbf{x}_i \cdot \boldsymbol{k}(t_j)}$ [14]. The term $\sum_{r=1}^{R} \boldsymbol{S}_r \boldsymbol{A} \tilde{\boldsymbol{b}}_r$ is a matrix/vector expression for the right-hand side of Eq. 3.2. $\boldsymbol{W}$ is a diagonal matrix containing a spatial error weighting that can be used to specify a region of interest (ROI) [23]. Integrated power of the total RF pulse may be controlled via the Tikhonov regularization term $\beta \sum_{r=1}^{R} \left\| \boldsymbol{b}_r + \tilde{\boldsymbol{b}}_r \right\|^2$, where β is a tuning parameter. We minimize $\Psi\left(\tilde{\boldsymbol{b}}_1, \ldots, \tilde{\boldsymbol{b}}_R\right)$ using the Conjugate Gradient (CG) method. Because of linearity of excitation in the small-tip-angle regime, and because the tip angle patterns excited by the new and initial pulses are in phase, $\left\{\boldsymbol{b}_1 + \tilde{\boldsymbol{b}}_1, \ldots, \boldsymbol{b}_R + \tilde{\boldsymbol{b}}_R\right\}$ will accurately excite the tip angle pattern $\theta^{des}(\boldsymbol{x})$. In short, we are given an initial pulse set that excites an erroneous tip angle pattern, and we design a set of correction pulses that excite the difference in tip angle between the erroneous and desired patterns. When the initial and correction pulses are summed, the result is a pulse set that excites an accurate pattern, in the small-tip regime.

Now consider the more challenging pulse design scenario in which $\theta^{des}(\boldsymbol{x})$ is a large-tip-angle desired pattern, and $\{\boldsymbol{b}_1, \ldots, \boldsymbol{b}_R\}$ are inaccurate initial large-tip-angle pulses. Eq. 3.1 no longer holds in this case, and we must use Bloch equation simulation to obtain $\theta(\boldsymbol{x})\, e^{i\angle M_{xy}(\boldsymbol{x})}$, where $\theta(\boldsymbol{x}) = \cos^{-1} \frac{M_z(\boldsymbol{x})}{M_0(\boldsymbol{x})}$. Furthermore, for larger tip-angles the right-hand side of Eq. 3.2 becomes an increasingly inaccurate model for the difference be-

tween the tip angles excited by $\{\boldsymbol{b}_1, \ldots, \boldsymbol{b}_R\}$ and $\left\{\boldsymbol{b}_1 + \tilde{\boldsymbol{b}}_1, \ldots, \boldsymbol{b}_R + \tilde{\boldsymbol{b}}_R\right\}$. Despite this, we have found empirically that if the initial pulses $\{\boldsymbol{b}_1, \ldots, \boldsymbol{b}_R\}$ excite angles smaller than $180°$, then the pulses $\left\{\boldsymbol{b}_1 + \tilde{\boldsymbol{b}}_1, \ldots, \boldsymbol{b}_R + \tilde{\boldsymbol{b}}_R\right\}$ will still excite a more accurate pattern. That is, while the linear model of Eq. 3.2 and the *true* difference in flip-angle patterns are significantly different when the initial pulses excite large-tip angles, the difference is not so great as to prevent an improvement in accuracy when $\left\{\tilde{\boldsymbol{b}}_1, \ldots, \tilde{\boldsymbol{b}}_R\right\}$ are designed using Eq. 3.2. In contrast to the linear small-tip-angle case, the desired level of accuracy generally cannot be reached with only one design of $\left\{\tilde{\boldsymbol{b}}_1, \ldots, \tilde{\boldsymbol{b}}_R\right\}$. To make further improvements, we adopt a fixed-point iterative procedure to update the initial pulses multiple times, until accuracy stops improving. It is usually necessary to incorporate the transverse magnetization phase term, $e^{i\angle M_{xy}(\boldsymbol{x})}$, into d^{new} so that the flip angle pattern produced by $\left\{\tilde{\boldsymbol{b}}_1, \ldots, \tilde{\boldsymbol{b}}_R\right\}$ adds with the intended sign. If the phase term is not incorporated, the algorithm may stop improving excitation accuracy before an acceptable error level is reached.

In summary, the additive angle pulse design method is an iterative technique that improves the accuracy of a large-tip-angle RF pulse. At each iteration, a Bloch equation simulation is performed to obtain $\theta(\boldsymbol{x})\, e^{i\angle M_{xy}(\boldsymbol{x})}$ for the initial pulses, and new pulses are designed to excite $\theta^{new}(\boldsymbol{x})\, e^{i\angle M_{xy}(\boldsymbol{x})}$ that are added to the initial pulses, where $\theta^{new}(\boldsymbol{x}) \triangleq \theta^{des}(\boldsymbol{x}) - \theta(\boldsymbol{x})$. The summed pulses then replace the initial pulses in the next iteration. Iterations continue until excitation accuracy ceases to improve.

3.3 Methods

3.3.1 Pulse Design

We used the additive angle method to design two-dimensional RF pulses, and compared it to small-tip-angle RF pulse design in simulations and experiments. Desired patterns were specified on a 64×64 grid, with a FOV of 24 cm $\times$ 24 cm, and were blurred

by convolution with a Gaussian kernel of FWHM = 1.2 cm, to reduce ringing in the resulting excitation patterns. Bloch equation simulations for pulse design were performed on the same grid, while simulations for final error computation and comparison were performed on a finer 128×128 grid with the same FOV. Bloch simulations for pulse design were initialized with all magnetization in M_z. Spins outside the ROI were not simulated. 50 CG iterations were used for each small-tip-angle pulse design. To ensure that $\left\{\tilde{\boldsymbol{b}}_1, \ldots, \tilde{\boldsymbol{b}}_R\right\}$ stay in the small-tip-angle regime, we scaled $d^{new}(\boldsymbol{x})$ to a maximum tip angle of $\frac{\pi}{4}$ radians, except in simulation II, where the maximum tip angle was varied. We stopped the additive-angle iterations when the Root-Mean-Square Error (RMSE), defined as $RMSE = \frac{1}{N_s}\sqrt{\sum_{i=1}^{N_s}\left|\theta^{des}(\boldsymbol{x}_i) - \theta(\boldsymbol{x}_i)\right|^2}$, between the desired and Bloch-simulated tip-angle patterns at the current iteration decreased by less than 0.01% of the previous one. For conventional small-tip design, we used the method in [23], with the same desired flip angle pattern as in the additive angle implementation, and with 100 CG iterations. Small-tip-angle design was initialized with zero pulses, and additive angle design was initialized with the small-tip-designed pulses, scaled by 0.75, except in Simulation II, where the scaling factor is varied. This scaling factor corresponds to a nominal initial flip angle of $3\pi/8$ radians in the case of $\pi/2$-pulse design, and $3\pi/4$ radians in π-pulse design. Pulses were designed with a small Tikhonov regularization parameter $\beta = 10^{-1}$, except in Simulation II, where β was varied. All pulse designs and simulations were performed in MATLAB R2006a (Mathworks, Natick, MA, USA), on a 3.4GHz Pentium IV workstation with 2GB RAM.

3.3.2 Numerical Simulations

Simulations of parallel excitation were carried out assuming an 8 element active rung transmit array [41]. Transmit sensitivity patterns were obtained via Finite-Difference Time-Domain simulation [42] of the array at 3.0 Tesla, using a phantom modeled as a

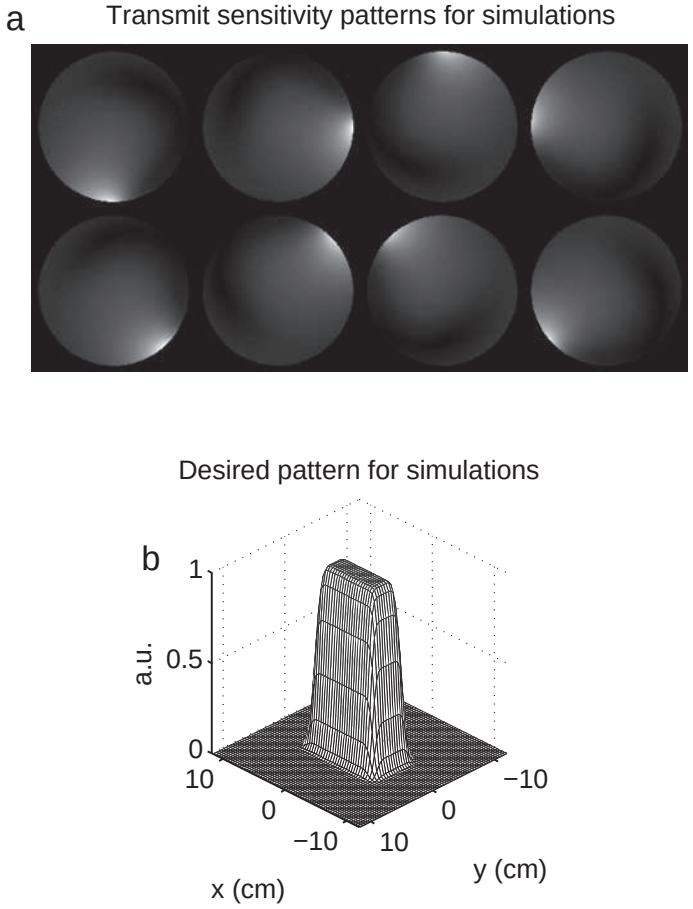

Figure 3.1: (a) Magnitude of transmit sensitivity patterns used in simulations of eight-channel parallel excitation. (b) Desired flip angle pattern used in simulations, which was a smoothed 10 cm $\times$ 5 cm rectangular block, whose peak was scaled to π and $\frac{\pi}{2}$ for pulse design.

22 cm diameter lossy cylinder with $\sigma = 0.3$ S/m and $\epsilon_r = 80$ (Fig. 3.1a). The ROI for pulse design and error calculation was the phantom interior. The desired pattern, shown in Fig. 3.1b, was a rectangular block that was centered in the phantom, with dimensions 10 cm $\times$ 5 cm.

We designed pulses using spiral and echo-planar (EP) excitation k-space trajectories. Spiral trajectories were single-shot spiral-out with the parameters: maximum amplitude = 4 G/cm, maximum slew rate = 18 G/cm/ms. Acceleration was achieved via undersampling in the radial direction, resulting in reduction of the excitation field of view (XFOV) of the individual coils' excitation patterns. EP trajectories were designed using the parameters: maximum amplitude = 4 G/cm, maximum slew rate = 15 G/cm/ms. For these trajectories, acceleration was achieved via undersampling in the blipped (phase-encoded) dimension. We define "speedup factor" as the ratio of the FOV of the desired pattern to the reduced XFOV of the excitation k-space trajectories. The spatial resolution for all trajectories was 0.75 cm, which is twice that of the grid on which the desired patterns were specified. We find that specifying the desired pattern on a grid of finer resolution than the k-space trajectory improves accuracy of both small-tip-angle and additive angle-designed pulses. The sampling period for all pulses was 4 μs.

Simulation I: Speedup Factor

In the first simulation, we designed $\frac{\pi}{2}$- and π-excitation pulses with a range of speedup factors from 2.4 to 6, corresponding to an XFOV range from 10 cm down to 4 cm. We compared performance of the additive angle method to that of small-tip-angle design in terms of RMSE between excited and desired flip angle patterns, peak total RF field magnitude, and visual quality. Compute time was also recorded for the additive angle method.

Simulation II: Convergence

In this simulation we investigated convergence properties of the additive angle method. We repeated additive angle designs of EP (speedup factor = 3) and spiral (speedup factor = 4.8) π-pulses, and varied design parameters that may influence final excitation error. We first varied the nominal flip angle of the initial, small-tip-designed pulse that was used to seed the additive angle method, between 0 and 2, corresponding to seed pulses with nominal flip angles between 0 and 2π radians. We then performed designs in which we varied the maximum tip angle of $d^{new}(\boldsymbol{x})$ from $\pi/8$ to π radians, with a zero initial seed pulse. Finally, we performed designs over a range of β-values, from $\log_{10}\beta = -1$ to $\log_{10}\beta = 2.5$.

Simulation III: Refocusing

In this simulation we verified that a π-pulse designed using the additive angle method will refocus a population of spins possessing a range of off-resonant frequencies, and compared refocusing performance to that of a small-tip designed pulse. EP pulses with speedup factor = 3 (XFOV = 8 cm, pulse length 3.34 ms) were used in these simulations. We performed 40 simulations that were initialized with magnetization in the transverse plane everywhere in the object, but over a phase range of 0-2π radians, in 40 equally-spaced angular steps. The initial phase represents the phase accrued due to off-resonance between excitation and TE/2. After application of the pulse, the initial phase was again added to the magnetization's phase, representing the phase accrued between the refocusing pulse (TE/2) and TE. We then summed the magnetization over the phase range, to obtain the net magnetization at TE. Phase evolution due to off-resonance during pulse application was neglected, due to the short duration of the pulse.

3.3.3 Scanner Experiment

Scanner experiments were performed on a GE 3T Signa Excite Scanner (GE Healthcare, Milwaukee, WI, USA). Due to a lack of parallel transmit hardware, we carried out a single-channel transmit experiment to validate the additive angle design method and compared it to small-tip-angle pulse design. We computed 2D spatially-selective inversion pulses that were applied in the spin preparation stage of a spiral GRE sequence. The sequence began with the inversion pulses, followed directly by gradient crushers, which were subsequently followed by standard sinc excitation and a multi-shot spiral-in readout. Ideally, the inversion pulses flip image phase within the inverted region, but leave image magnitude unperturbed.

All transmission and reception was performed using a standard birdcage head coil. A spherical MnCl phantom was used, which expressed a non-uniform transmit field magnitude (B1+) in the birdcage coil. The B1+ field was mapped for one slice in the phantom by acquiring a set of GRE images collected with nominal flip angles $(30°, 60°, 90°)$, and processing the resulting images with a regularized B1+ mapping method [43]. The imaging parameters for B1+ mapping were as follows: slice thickness = 4.0 mm; FOV = 24 cm; reconstructed matrix size = 64 $\times$ 64; repetition time (TR) = 8 s; echo time (TE) = 10 ms. The measured B1+ pattern was used to design EP pulses that inverted the 9 $\times$ 3 cm square desired pattern shown in Fig 3.9a. Placement of the inverted region was chosen such that a large B1+ magnitude gradient existed across the long dimension of the region. The EP trajectory was designed with XFOV = 18 cm, spatial resolution = 0.75 cm, maximum slew rate = 15 G/cm/ms, and sampling period = 4 μs. To reduce RF magnitude near the center of k-space, the central 3 phase encodes were designed with a maximum gradient amplitude of 0.5 G/cm, while the outer 22 phase encodes were designed with maximum amplitude = 4 G/cm. These parameters yielded a pulse length of 8.7 ms. Pulse design time, includ-

ing B1+ map estimation, was recorded. Imaging parameters for the inversion-preparation sequence were as follows: slice thickness = 4.0 mm; FOV = 24 cm; reconstructed matrix size = 128 $\times$ 128; TR = 8 s; TE = 20 ms; nominal flip angle (sinc pulse) = 10°; 8 averages. Excitation gradient waveforms were shifted forward by 150 μs to compensate for the delay between RF and gradient channels. Four spiral interleaves were used in both the B1+ mapping and inversion-preparation sequences to reduce readout time so that off-resonance effects during acquisition were minimized. We also acquired images with the inversion pulse magnitude set to zero. These were used to remove the effects of non-uniform transmit and receive sensitivities during sinc excitation and readout by dividing them from of images acquired with the inversion pulses switched on. Images were reconstructed using a fast implementation of the off-resonance compensated conjugate phase method [33]. It used field maps estimated from two images acquired with a TE difference of 2.5 ms [34].

3.4 Results

3.4.1 Simulation I: Acceleration

Figure 3.2 shows simulated π-excitation patterns. In Figs. 3.2(a,c), the small-tip-designed pulses produce significant erroneous excitation outside the inverted blocks. In the EP case, we see the well-known bandwidth narrowing effect [44] that occurs when small-tip-angle Cartesian pulses are scaled to large tip-angles. This effect manifests as a spatially narrow inversion region, compared to the wider region the pulses would correctly excite if scaled to produce small tip-angles. For both EP and spiral trajectories, excitation accuracy is dramatically improved by the additive angle method. In Figs. 3.3(a,b), we see that inversion pulses designed using the additive angle method achieve lower RMSE over the full speedup factor range, without a significant increase in peak RF magnitude. Improvement in accuracy is most dramatic for the EP trajectory. Figure 3.4 plots coil 1's

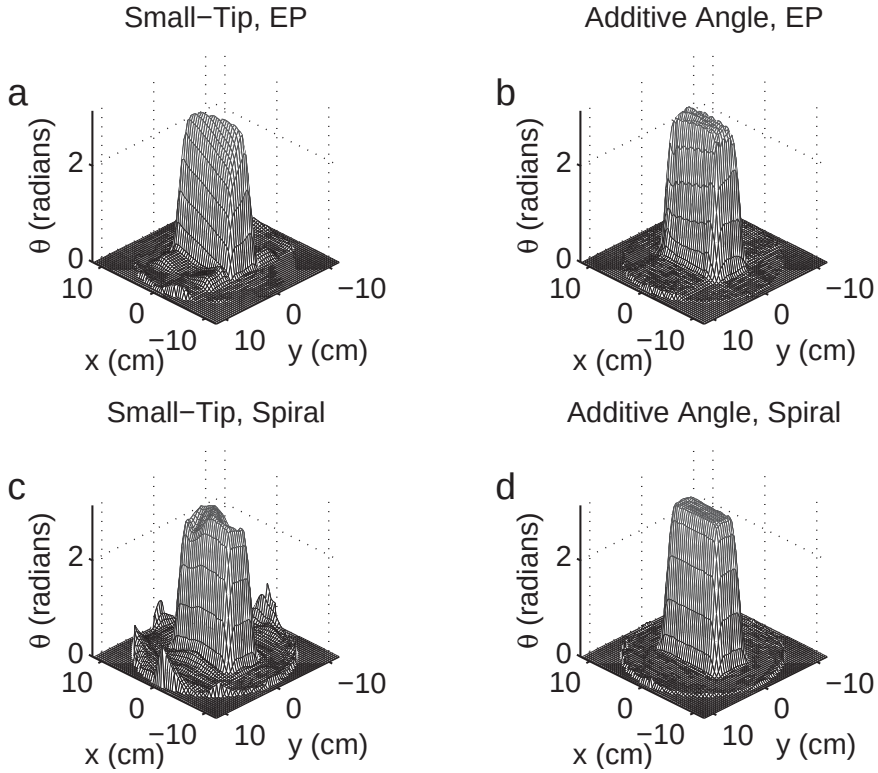

Figure 3.2: Simulated π excitation patterns produced by pulses designed with the small-tip (a,c) and additive angle (b,d) methods, for an EP trajectory (a,b) with speedup factor = 3 (XFOV = 8 cm, pulse length 3.34 ms), and a spiral trajectory (c,d) with speedup factor = 4.8 (XFOV = 5 cm, pulse length 1.16 ms). For both trajectories, the additive angle method yields pulses that produce patterns with reduced erroneous excitation outside the block, and improved uniformity inside the block.

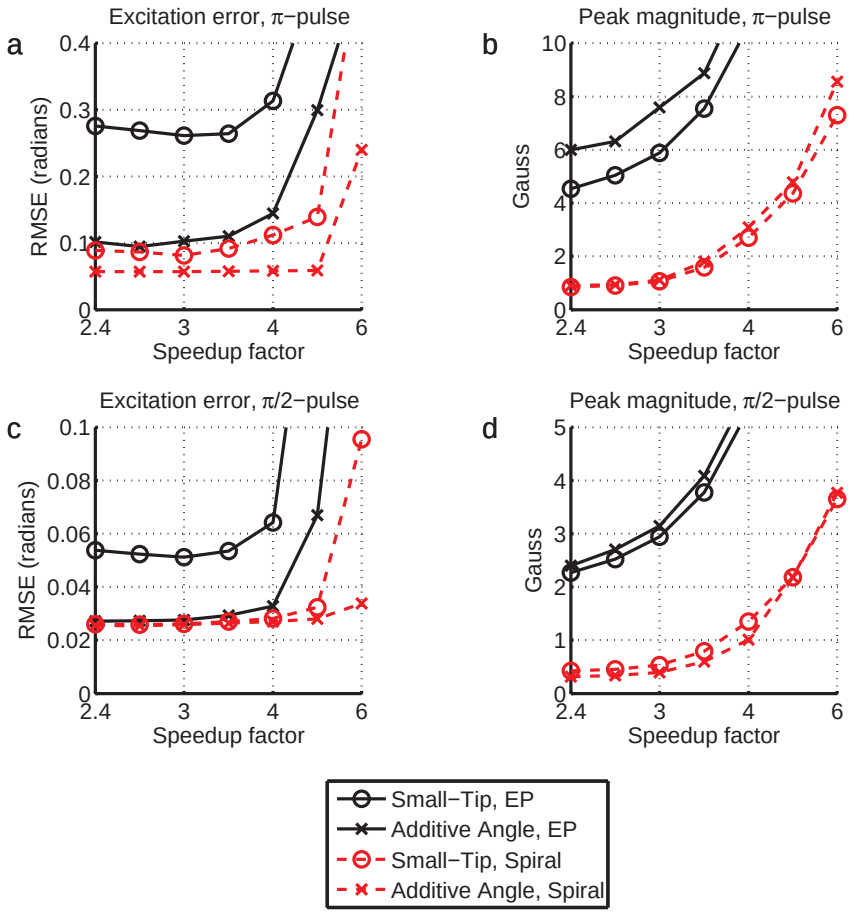

Figure 3.3: Comparison of excitation accuracy and peak RF magnitude between pulses designed using the small-tip and additive angle methods, over a range of speedup factors. For both π- and $\frac{\pi}{2}$-pulses (a,b), the additive angle method achieves lower error, without a significant increase in pulse power. Improvement in accuracy with the additive angle method is most significant for EP and spiral π-pulses, and for EP $\frac{\pi}{2}$-pulses.

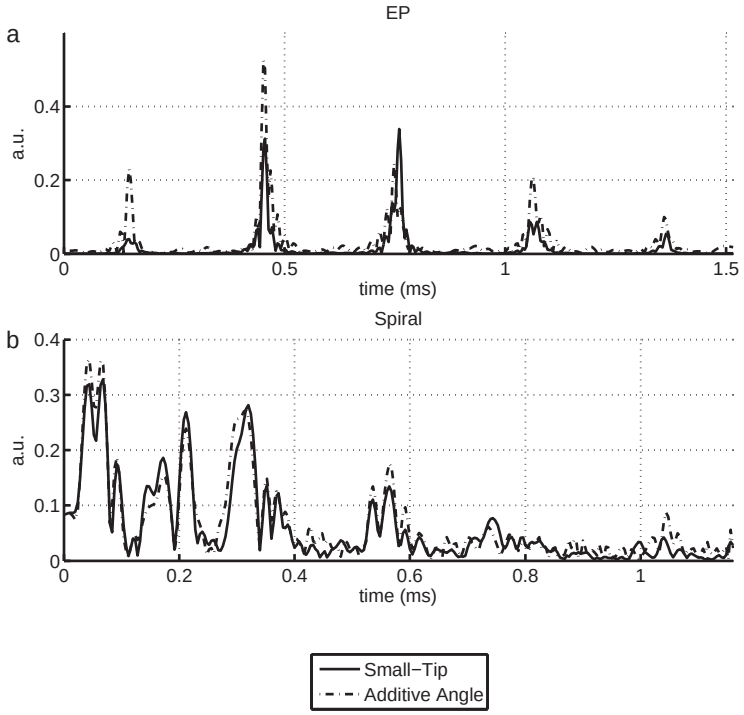

Figure 3.4: Magnitude of the π-excitation pulses of Fig. 3.2 for coil 1. (a) In the EP case (pulse plotted for the central five phase encode lines only), large changes in pulse shape resulted in significantly decreased RMS error, from 0.26 radians for the small-tip designed pulses, to 0.10 radians for the additive angle-designed pulses. (b) For spiral pulses, smaller perturbations decreased RMS error from 0.14 radians to 0.06 radians.

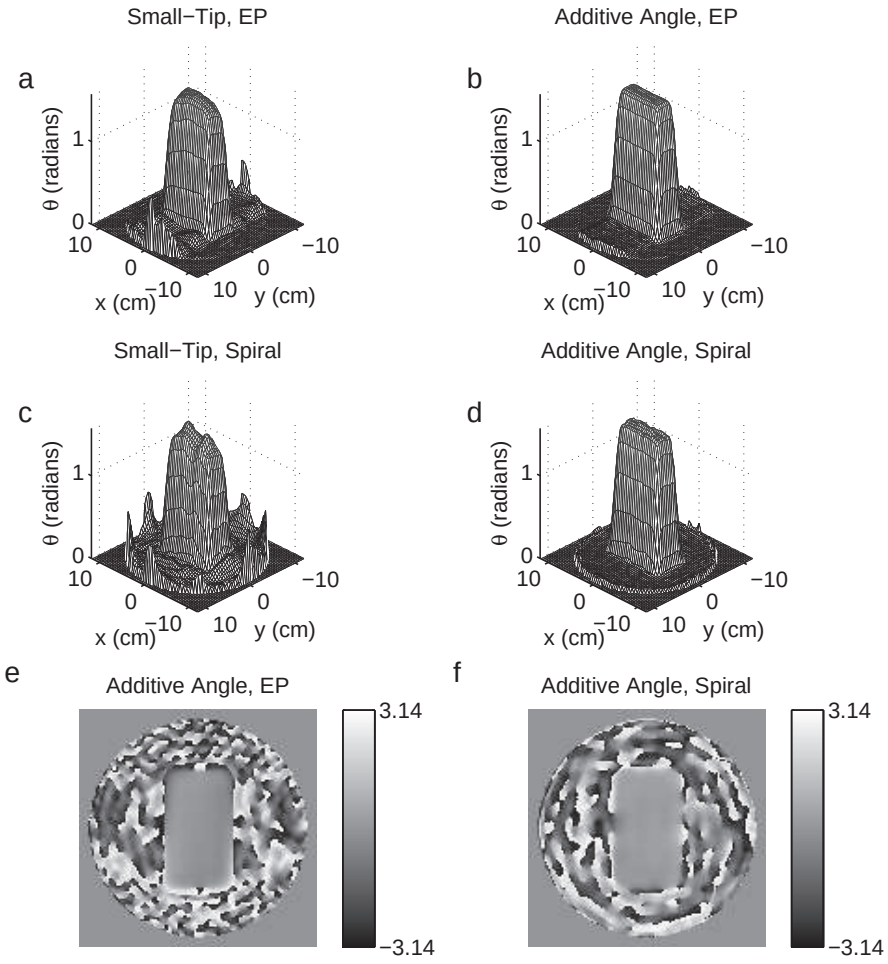

Figure 3.5: Simulated $\frac{\pi}{2}$ excitation patterns produced by pulses designed with the small-tip (a,c) and additive angle (b,d) methods. For both the EP trajectory (a,b) with speedup factor = 4 (XFOV = 6 cm, pulse length 2.7 ms), and the spiral trajectory (c,d) with speedup factor = 6 (XFOV = 4 cm, pulse length 1 ms), pulses designed with the additive angle method produce patterns with reduced erroneous excitation outside the block, and improved uniformity inside the block. (e,f) Pulses designed using the additive angle method excite magnetization with uniform phase, even though phase is allowed to drift during the design process.

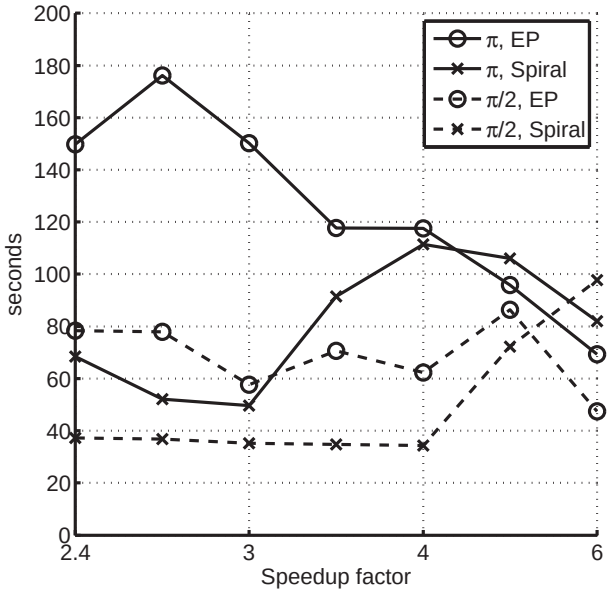

Figure 3.6: Measured design times for simulations. The design times for $\frac{\pi}{2}$-pulses are shorter than those for π-pulses. Additionally, design times for spiral pulses are generally shorter than those for EP pulses. This is most likely due to the shorter length of spiral pulses compared to EP pulses, and the lower error achieved by the small-tip-designed spiral pulses used to seed the additive angle method, compared to EP seed pulses.

pulse magnitude for the π-excitation pulses of Fig. 3.2. We observe that in the EP case (Fig. 3.4(a)), large changes in pulse shape were required to achieve high excitation accuracy, while in the spiral case (Fig. 3.4(b)), smaller perturbations resulted in significantly improved accuracy. Figure 3.5 shows simulated $\frac{\pi}{2}$-excitation profiles, and we again see an improvement in excitation accuracy for the additive angle case. As shown in Figs. 3.3(c,d), this improvement is maintained over the simulated speedup factor range, particularly in the EP case, again without a significant increase in peak RF magnitude. Additionally, for both trajectories, the phase within the blocks excited by additive angle pulses is highly uniform, as shown in Figs. 3.5(e,f). In the EP case of Figs. 3.5(b,e), an average (RMS) phase deviation of 4.8° was measured in the block, while in the spiral case of Figs. 3.5(d,f), an RMS deviation of 3.5° was measured. This is a welcome result, considering that the excited magnetization's phase is controlled only initially via the desired pattern used in the initial small-tip-angle pulse design.

Figure 3.6 plots design times required for convergence. Spiral design times are shorter than EP design times for both π- and $\frac{\pi}{2}$-pulses, with the exception of the highest speedup factors for which accurate EP pulses are not reached. Longer EP design time is most likely due to the longer duration of the EP trajectory for a given speedup factor, and the higher level of error produced by the small-tip-designed pulses used to seed EP pulse design. Compared to spiral design times, the longer EP times are also in agreement with the larger changes in waveform shape created by our method, shown in Fig. 3.4. Design time for π-excitation pulses is generally longer than that for $\frac{\pi}{2}$-pulses in both EP and spiral pulse design, which can be attributed to the higher level of error produced by the small-tip-designed π-pulses used to seed our method. Bloch simulation/small-excitation pulse design iterations required for convergence were roughly proportional to design time. EP π-pulse design required between 10 and 20 iterations, while spiral π-pulse design required between 7 and 16 iterations. For $\frac{\pi}{2}$-pulse design, the EP trajectory required between 7 and 12 iterations, while the spiral trajectory required between 5 and 15 iterations. In comparison to these measured times, design times for exact Bloch-equation based methods are generally an order of magnitude longer.

3.4.2 Simulation II: Convergence

Figure 3.7 shows results of our convergence investigation. From the designs in which we varied the nominal flip angle of the initial small-tip-designed pulse (Fig. 3.7a), we see that the additive angle method converges to the same error level over the range of nominal flip angles from 0 to π radians. In fact, the method continues to converge to the same error even for larger nominal flip angles that would not be used in practice. Figure 3.7b shows that the method is also robust to the maximum magnitude of $\boldsymbol{d}_{new}(\boldsymbol{x})$. Figure 3.7c shows that the final RMS error of the pulses is a smooth, increasing function of the Tikhonov regularization parameter β. Using a higher β results in a higher RMS error, but reduces

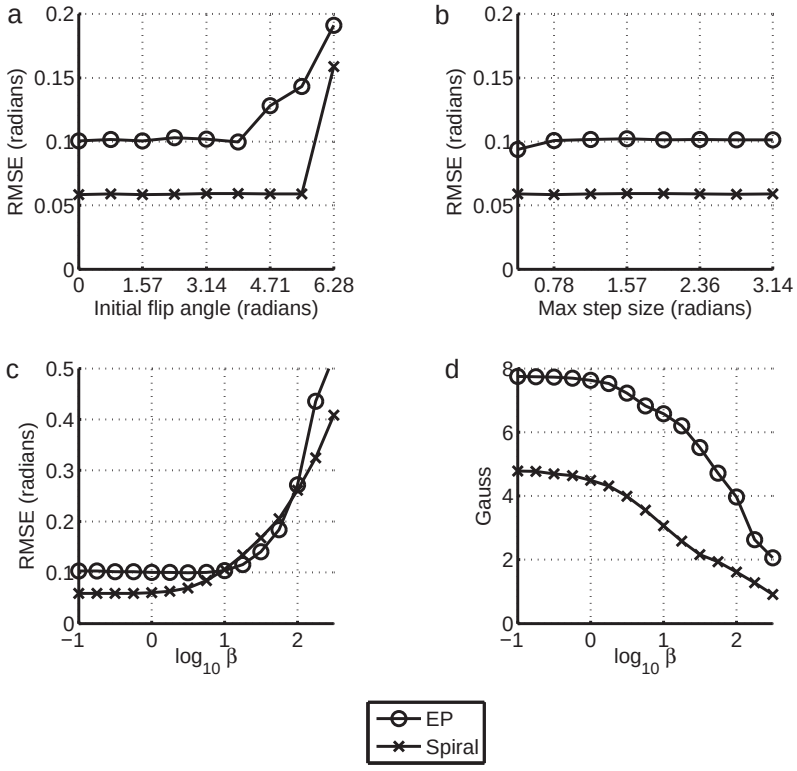

Figure 3.7: Influence of design parameters on convergence and peak RF magnitude. Additive angle designs of EP (speedup factor = 3) and spiral (speedup factor = 4.8) π-pulses were repeated over a range of design parameters, to investigate the method's convergence properties. (a,b) The additive angle method is robust to both the nominal flip angle of the small-tip-designed pulse used to seed the method, and the maximum flip angle allowed in $d^{new}(\boldsymbol{x})$. (c,d) The Tikhonov regularization parameter β can be increased to mitigate peak RF magnitude, at the cost of increased excitation error.

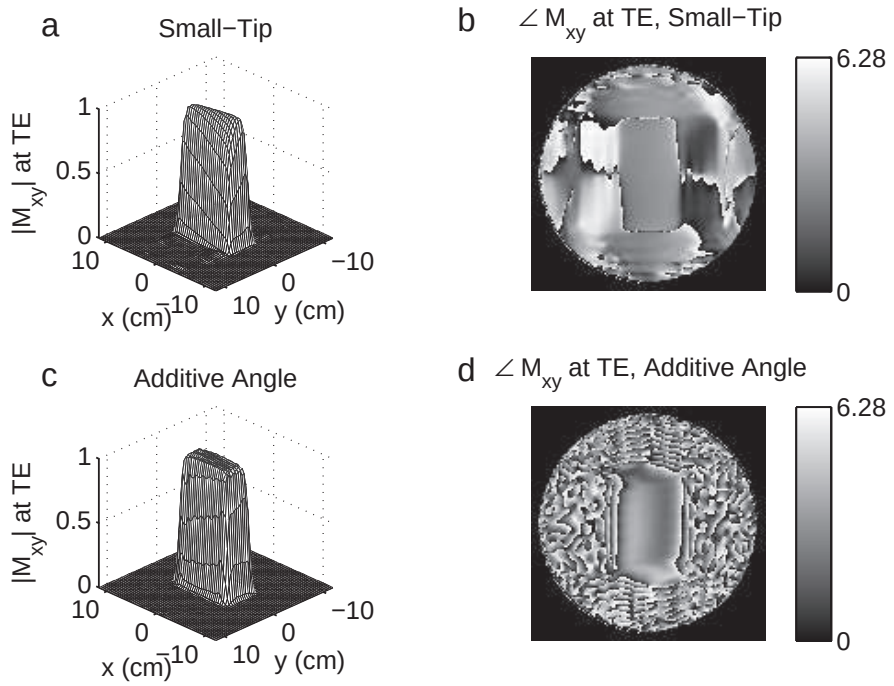

Figure 3.8: Comparison of small-tip and additive angle-designed EP π-pulses applied as refocusing pulses. In this simulation, the pulses of Figs. 3.2(a,b) were used to excite magnetization initially in the transverse plane, and over a range of transverse-plane phase angles. (a) The small-tip-designed pulse fails to uniformly rotate magnetization by π radians within the block, resulting in an inhomogeneous magnetization pattern at TE. Furthermore, the small-tip-designed pulse partially refocuses magnetization outside the block. (b) In comparison, the additive angle-designed pulse fully refocuses magnetization within the block, and does not refocus magnetization outside the block. (b,d) The net phase of magnetization at TE is spatially varying for both pulses, though the additive-angle pulse leaves more phase variation within the refocused block.

peak RF magnitude, as shown in Fig. 3.7, and can be tuned to balance the two metrics. EP and spiral pulse designs possess similar sensitivity to all design parameters.

3.4.3 Simulation III: Refocusing

Figure 3.8 shows simulation results of small-tip and additive angle-designed π-pulses used for refocusing. In Fig. 3.8a, the magnetization magnitude subsequent to application of the small-tip-designed π-pulse of Fig. 3.2a is highly non-uniform within the refocused block, and exhibits a narrowing effect similar to that of the pulse's flip angle pattern. Some magnetization is also refocused outside the block. Figure 3.8b shows the magnetization phase at TE, which is relatively uniform within the block, with an RMS deviation of 9°.

In contrast, Fig. 3.8c shows that the magnetization after application of the additive angle-designed pulse is uniform inside the block, and no magnetization is refocused outside it. In Fig. 3.8d, we see that for the additive angle pulse, magnetization phase is spatially-varying within the block at TE, with a higher RMS phase deviation of 34°.

3.4.4 Scanner Experiment

Figure 3.9b shows a magnitude profile of the estimated B1+ map, which expresses significant inhomogeneity over the phantom. Within the desired inversion pattern, the B1+ map has a maximum magnitude of 0.74 Gauss/full RF magnitude, a minimum of 0.51 Gauss/full RF magnitude, and a mean of 0.66 Gauss/full RF magnitude. A pulse designed without B1+ compensation and tuned to excite π radians at the mean B1+ magnitude would produce flip angles between 2.43 and 3.5 radians over the excited region. Figures 3.9(c,d) show images obtained using the inversion-preparation sequence. The effects of non-uniform B1+ during sinc excitation and B1- during signal reception have been removed from these images using reference images obtained with the inversion pulses set to zero. As in our simulations, we see that the small-tip-designed pulses suffer from a bandwidth-narrowing effect [44] in the phase-encode dimension. The effect is manifested as the narrowed M_y profile in Fig. 3.9e, and the non-uniform image intensity of the inverted region of Fig. 3.9c. In contrast, the additive angle-designed pulse inverts an accurate rectangular region (Fig. 3.9d), in which the image intensity is more uniform (Figs. 3.9(d,e)). The intensity inside the inverted region is close to that outside it, indicating that a full inversion was achieved in the square. Pulse design time, including B1+ map image reconstruction and estimation, was 46.3 seconds.

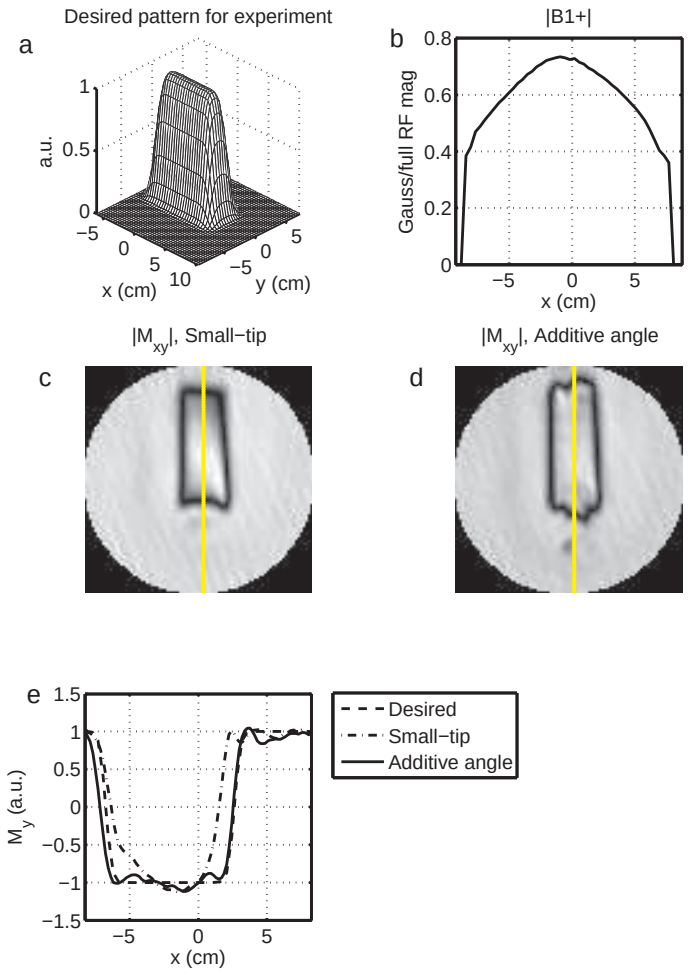

Figure 3.9: Experimental results. (a) The desired flip angle pattern was a smoothed 9 $\times$ 3 cm square, whose peak was scaled to π for inversion pulse design. (b) Magnitude profile through the center of the object's B1+ field map, along the dashed lines in (c,d). (c,d) Magnitude images of the phantom after application of the small-tip-designed pulse (c) and additive angle-designed pulse (d). (e) M_y profiles taken through the center of the phantom, as indicated by the dashed lines in (c,d). The small-tip-designed pulse produces a pattern that is narrowed in the phase-encode direction, while the additive angle pulse produces an accurate square inversion region that matches the desired pattern. The M_y profiles verify that magnetization phase in the inverted region is shifted by π relative to magnetization outside.

3.5 Discussion and Conclusions

We have presented a new method for fast large-tip-angle RF pulse design in multi-dimensional parallel excitation, and have shown that it may be used to design π- and $\frac{\pi}{2}$-excitation pulses. We have demonstrated that these pulses produce flip angle patterns with significantly improved accuracy, compared to pulses designed using small-tip-angle methods. In the case of spiral trajectories, improvement in accuracy is most dramatic at high speedup factors, corresponding to large reductions in pulse length. This is due to the fact that pulses designed with spiral trajectories satisfy the linear-class conditions [8] at low speedup factors, and may thus be scaled to produce accurate large-tip-angle excitation patterns. At high speedup factors however, increased pulse magnitude violates the small-RF approximation used to derive the linear class [23], and a non-linear design method such as the one presented here must be used. In the case of EP trajectories, we showed that a significant improvement in accuracy is achieved over the full range of speedup factors. The EP trajectory does not satisfy the linear-class conditions, and so a non-linear method must be used at all speedup factors. We showed experimentally that our method is also capable of designing accurate large-tip-angle single-channel EP pulses. Though not presented here, we have also designed 'B1+ shimming' pulses using three-dimensional fast k_z trajectories [20, 27], and have found that the additive angle method produces accurate three-dimensional large-tip-angle pulses in that scenario as well.

Our method presents two opportunities to further reduce compute time by parallelizing computations. First, all small-tip-angle pulse designs require the evaluation of as many NUFFT's as there are coils, at each iteration of the CG algorithm. Because the NUFFT's are independent of each other, they can be computed in parallel to achieve a reduction in small-tip-angle design times. The second opportunity is in Bloch simulation, which may

be parallelized by dividing the simulation spatially or temporally. Though our method already produces accurate pulses in a short time, these improvements would make online large-tip-angle parallel pulse design even more practical.

Many of the pulses we designed in simulation possessed high peak RF magnitudes and could not be feasibly deployed on human MR scanners. We showed in simulations that one approach to obtaining usable pulses is to increase Tikhonov regularization, which reduces peak RF magnitude at the cost of increased excitation error. Another approach is to modify the k-space trajectories using variable-XFOV [45, 46] or variable-rate strategies [47, 48] to increase sampling density in regions of k-space where the pulses are expected to possess high magnitude. Both strategies will reduce RF magnitude at the cost of increased pulse length. In the design of large-tip-angle pulses, the k-space regions of high RF magnitude can be determined either from prior pulse designs, or by intuition from the small-tip-angle pulse design scenario.

In our method, the excited transverse magnetization's phase is controlled only initially via the desired pattern for small-tip-angle pulse design, and is allowed to vary both spatially and between design iterations. Deviations from the initial phase are introduced by Bloch equation non-linearity. In our simulations we found that phase deviation within the $\frac{\pi}{2}$-excitation patterns was small, suggesting that a multidimensional pulse designed using our method could still be used to perform slice-selection in one dimension, with negligible signal loss due to signal cancellation through the slice. We also demonstrated that π-excitation pulses may be employed for refocusing, though there are larger variations in the resulting phase in this case. While this is not problematic for scenarios in which the pulses are applied in the imaging plane, it may reduce their utility for cases where signal is averaged across the refocused region. In Chapter IV, we introduce a large-tip-angle parallel pulse design method that permits control of excitation phase.

In conclusion, we have introduced a method for large-tip-angle parallel RF pulse design that is capable of producing accurate multidimensional pulses in a short time. The method is simple to implement, provided one already has the software tools available to design small-tip-angle parallel excitation pulses, and a Bloch equation simulator. Through spiral and EP pulse design simulations, we demonstrated that the method produces pulses of high accuracy that may be used for excitation, inversion, and refocusing.

CHAPTER IV

Fast optimal control method for large-tip-angle parallel RF pulse design

4.1 Introduction

The optimal control pulse design method was initially introduced for the design of one-dimensional slice-selective pulses [25]. Based on optimal control theory [49], the method is an iterative algorithm that designs an RF pulse to minimize a least-squares cost function. At each iteration, the Bloch equation is evaluated using the current pulse. Gradients with respect to the Bloch equation and the cost function are also computed, and the pulse is updated by stepping in the negative gradient direction. As we showed in Chapter I, the method readily generalizes to multidimensional parallel excitation [30], however, evaluation of the Bloch equation at each iteration is computationally expensive, and renders the method unsuitable for online use.

The goal of the fast optimal control method is to replace the Bloch equation with a linear model that can be evaluated rapidly, preferably using non-uniform fast Fourier transforms (NUFFT's). In Chapter III, we investigated a method that uses the small-tip-angle equation for this purpose, a choice that was driven by intuition from the small-tip-angle regime. The approach we take here is to *analytically* linearize the Bloch equation around an underlying pulse, resulting in a model that accurately relates small perturbations in an RF pulse to small perturbations in magnetization. As will be shown, the new algorithm converges to

pulses of similar quality to those designed using conventional optimal control, in much less time. Compared to the additive angle method of Chapter III, this algorithm produces pulses of higher quality, and allows control of excitation phase.

The fast optimal control method has two main advantages over the additive angle method introduced in Chapter III. First, it is derived by a more rigorous treatment of the Bloch equation, and as such possesses a more solid theoretical foundation. While the additive angle iterations were demonstrated to consistently and robustly reduce the value of an l^2 cost function, their form was not derived from any cost function. In contrast, the fast optimal control method makes iterative updates to RF pulses that are directly derived from the cost function being minimized. As a result, it is reasonable to expect that the fast optimal control method may be more computationally efficient than the additive angle method, and may converge to more accurate pulses. Additionally, the cost function framework allows the user to easily include regularizers, or jointly refine gradient waveforms. The second advantage of the fast optimal control method is that the user maintains control of the excited *phase* pattern. While additive angle iterations can be initialized with pulses designed to produce a desired phase pattern, the pattern is allowed to drift from iteration to iteration. In Chapter III we showed that in the case of EP pulses, the excited phase of additive-angle-designed pulses deviated significantly from the initial flat phase pattern. Control of the excited phase pattern may be important in certain pulse design scenarios, e.g., if the imaging sequence does not resolve one of the dimensions selected by a tailored excitation or refocusing pulse, in RF-encoded sequences [50, 51], or in spin echo sequences requiring a specific phase relationship between excitation and refocusing pulses, such as 90_x-180_y.

4.2 Theory

4.2.1 Derivation of perturbed spinor parameters

Consider a scenario in which we are given a set of (possibly) large-tip-angle RF pulses $\{b_1, \ldots, b_R\}$ for R coils. At a spatial position $\boldsymbol{x}$, the spin-domain Bloch equation for these pulses is (Eq. 1.5):

$$\begin{pmatrix} \dot{\beta}_0 \\ \dot{\alpha}_0^* \end{pmatrix} = \frac{i\gamma}{2} \begin{pmatrix} \boldsymbol{G}\cdot\boldsymbol{x} & b_{tot}^* \\ b_{tot} & -\boldsymbol{G}\cdot\boldsymbol{x} \end{pmatrix} \begin{pmatrix} \beta_0 \\ \alpha_0^* \end{pmatrix}, \tag{4.1}$$

where $b_{tot} = \sum_{r=1}^{R} s_r^*(\boldsymbol{x})\, b_r^*$, $s_r(\boldsymbol{x})$ is coil r's transmit sensitivity pattern. We have dropped the time dependence of b_r, α_0, β_0 and $\boldsymbol{G}$, and the spatial dependence of b_{tot}, α_0, and β_0 for brevity. Our goal is to derive a differential equation for the *perturbations* $\left(\tilde{\alpha}, \tilde{\beta}\right)$ of (α_0, β_0), induced by a pulse set $\left\{\tilde{b}_1, \ldots, \tilde{b}_R\right\}$ that is added to $\{b_1, \ldots, b_R\}$. To obtain this equation, we subtract (4.1) from the Bloch equation for the summed pulse set $\left\{b_1 + \tilde{b}_1, \ldots, b_R + \tilde{b}_R\right\}$, yielding:

$$\begin{aligned} \begin{pmatrix} \dot{\tilde{\beta}} \\ \dot{\tilde{\alpha}}^* \end{pmatrix} = \frac{i\gamma}{2} \begin{pmatrix} \boldsymbol{G}\cdot\boldsymbol{x} & b_{tot}^* + \tilde{b}_{tot}^* \\ b_{tot} + \tilde{b}_{tot} & -\boldsymbol{G}\cdot\boldsymbol{x} \end{pmatrix} \begin{pmatrix} \beta_0 + \tilde{\beta} \\ \alpha_0^* + \tilde{\alpha}^* \end{pmatrix} - \\ -\frac{i\gamma}{2} \begin{pmatrix} \boldsymbol{G}\cdot\boldsymbol{x} & b_{tot}^* \\ b_{tot} & -\boldsymbol{G}\cdot\boldsymbol{x} \end{pmatrix} \begin{pmatrix} \beta_0 \\ {\alpha_0}^* \end{pmatrix}. \end{aligned} \tag{4.2}$$

Multiplying this out gives the following coupled pair of differential equations:

$$\dot{\tilde{\beta}} = \frac{i\gamma}{2} \left(\boldsymbol{G}\cdot\boldsymbol{x}\tilde{\beta} + b_{tot}^*\tilde{\alpha}^* + \tilde{b}_{tot}^*\alpha_0^* + \tilde{b}_{tot}^*\tilde{\alpha}^* \right) \tag{4.3}$$

$$\dot{\tilde{\alpha}}^* = \frac{i\gamma}{2} \left(b_{tot}\tilde{\beta} + \tilde{b}_{tot}\beta_0 + \tilde{b}_{tot}\tilde{\beta} - \boldsymbol{G}\cdot\boldsymbol{x}\tilde{\alpha}^* \right). \tag{4.4}$$

This pair of equations seems unsolvable analytically, so we simplify it using approximations inspired by the small-excitation approximation (Section 1.2.2). We expect that $b_{tot}^*\tilde{\alpha}^*$ and $\tilde{b}_{tot}^*\tilde{\alpha}^*$ will be small compared to other terms in Eq. 4.3, so we approximate them as

zero. Likewise, we approximate as zero $b_{tot}\tilde{\beta}$ and $\tilde{b}_{tot}\tilde{\beta}$ in Eq. 4.4. These approximations *decouple* the equations for $\dot{\tilde{\beta}}$ and $\dot{\tilde{\alpha}}^*$, leaving:

$$\dot{\tilde{\beta}} \approx \frac{i\gamma}{2}\left(\boldsymbol{G}\cdot\boldsymbol{x}\tilde{\beta} + \tilde{b}^*_{tot}\alpha^*_0\right) \tag{4.5}$$

$$\dot{\tilde{\alpha}}^* \approx \frac{i\gamma}{2}\left(\tilde{b}_{tot}\beta_0 - \boldsymbol{G}\cdot\boldsymbol{x}\tilde{\alpha}^*\right). \tag{4.6}$$

Using initial conditions $\tilde{\alpha}(0) = 0$ and $\tilde{\beta}(0) = 0$, the solutions to these equations are:

$$\begin{aligned}\tilde{\beta}(\boldsymbol{x},T) &\approx \frac{i\gamma}{2}\sum_{r=1}^{R} s^*_r(\boldsymbol{x})\int_0^T \tilde{b}^*_r(t)\,\alpha^*_0(\boldsymbol{x},t)\,e^{\frac{i\gamma}{2}\boldsymbol{x}\cdot\int_t^T \boldsymbol{G}(t')dt'}dt \\ &= \frac{i\gamma}{2}\sum_{r=1}^{R} s^*_r(\boldsymbol{x})\int_0^T \tilde{b}^*_r(t)\,\alpha^*_0(\boldsymbol{x},t)\,e^{-\frac{i}{2}\boldsymbol{x}\cdot\boldsymbol{k}(t)}dt\end{aligned} \tag{4.7}$$

$$\begin{aligned}\tilde{\alpha}^*(\boldsymbol{x},T) &\approx \frac{i\gamma}{2}\sum_{r=1}^{R} s_r(\boldsymbol{x})\int_0^T \tilde{b}_r(t)\,\beta_0(\boldsymbol{x},t)\,e^{-\frac{i\gamma}{2}\boldsymbol{x}\cdot\int_t^T \boldsymbol{G}(t')dt'}dt \\ &= \frac{i\gamma}{2}\sum_{r=1}^{R} s_r(\boldsymbol{x})\int_0^T \tilde{b}_r(t)\,\beta_0(\boldsymbol{x},t)\,e^{\frac{i}{2}\boldsymbol{x}\cdot\boldsymbol{k}(t)}dt,\end{aligned} \tag{4.8}$$

where $\boldsymbol{k}(t) \triangleq -\gamma\int_t^T \boldsymbol{G}(t')\,dt'$. It is interesting to note that the small-excitation approximation (Section 1.2.2, Eqs. 1.17 and 1.19) is a special case of Eqs. 4.7 and 4.8. In that scenario, $b_{tot} = 0$, so $\beta_0 = 0$ and $\alpha^*_0(\boldsymbol{x},t) = e^{-\frac{i\gamma}{2}\boldsymbol{x}\cdot\int_0^t \boldsymbol{G}(t')dt'}$. Plugging these into (4.8) and (4.7), rearranging the k-space integral limits in (4.7), and summing the results with (α_0,β_0) yields the parallel excitation version of (1.19) and (1.17). The small-tip-angle approximation then follows as a special case of the small-excitation approximation in which magnetization is initially at equilibrium [8].

To implement Eqs. 4.7 and 4.8 on a computer, we discretize them to N_t time points and N_s spatial points, yielding:

$$\tilde{\beta}(\boldsymbol{x}_i,T) \approx \frac{i\gamma}{2}\Delta t\sum_{r=1}^{R} s^*_r(\boldsymbol{x}_i)\sum_{j=1}^{N_t}\tilde{b}^*_r(t_j)\,\alpha^*_0(\boldsymbol{x}_i,t_j)\,e^{-\frac{i}{2}\boldsymbol{x}_i\cdot\boldsymbol{k}(t_j)}, i = 1,\ldots,N_s \tag{4.9}$$

$$\tilde{\alpha}^*(\boldsymbol{x}_i,T) \approx \frac{i\gamma}{2}\Delta t\sum_{r=1}^{R} s_r(\boldsymbol{x}_i)\sum_{j=1}^{N_t}\tilde{b}_r(t_j)\,\beta_0(\boldsymbol{x}_i,t_j)\,e^{\frac{i}{2}\boldsymbol{x}_i\cdot\boldsymbol{k}(t_j)}, i = 1,\ldots,N_s, \tag{4.10}$$

where Δt is the sampling period. Expressed in matrix-vector form:

$$\tilde{\boldsymbol{\beta}} \approx \sum_{r=1}^{R} \operatorname{diag}\left\{s_r^*\left(\boldsymbol{x}\right)\right\} \boldsymbol{B} \tilde{\boldsymbol{b}}_r^*, \quad \boldsymbol{B} = \{b_{ij}\} \tag{4.11}$$

$$b_{ij} \triangleq \frac{i\gamma}{2} \alpha_0^*\left(\boldsymbol{x}_i, t_j\right) e^{-\frac{i}{2}\boldsymbol{x}_i \cdot \boldsymbol{k}(t_j)} \Delta t \tag{4.12}$$

$$\tilde{\boldsymbol{\alpha}}^* \approx \sum_{r=1}^{R} \operatorname{diag}\left\{s_r\left(\boldsymbol{x}\right)\right\} \boldsymbol{A} \tilde{\boldsymbol{b}}_r, \quad \boldsymbol{A} = \{a_{ij}\} \tag{4.13}$$

$$a_{ij} \triangleq \frac{i\gamma}{2} \beta_0\left(\boldsymbol{x}_i, t_j\right) e^{\frac{i}{2}\boldsymbol{x}_i \cdot \boldsymbol{k}(t_j)} \Delta t, \tag{4.14}$$

where $\tilde{\boldsymbol{b}}_r = \begin{bmatrix} \tilde{b}_r\left(t_1\right) & \cdots & \tilde{b}_r\left(t_{N_t}\right) \end{bmatrix}^T$. Eqs. 4.11 and 4.13 provide linear relationships that can be used to compute approximate perturbations to the spinor parameters, $\tilde{\boldsymbol{\beta}}$ and $\tilde{\boldsymbol{\alpha}}^*$, given pulse perturbations $\left\{\tilde{\boldsymbol{b}}_1, \ldots, \tilde{\boldsymbol{b}}_R\right\}$. Given an initial magnetization state, we use the perturbations to compute magnetization perturbations via Eq. 1.6. For example, if magnetization is initially at equilibrium, the magnetization perturbations are given by:

$$\begin{aligned} \tilde{m}_{xy} &\approx -2\left(\alpha_0^* + \tilde{\alpha}^*\right)\left(\beta_0^* + \tilde{\beta}^*\right) M_0 + 2\alpha_0^* \beta_0^* M_0 \\ &= -2\left(\alpha_0^* \tilde{\beta}^* + \beta_0^* \tilde{\alpha} + \tilde{\alpha}^* \tilde{\beta}^*\right) M_0 \\ &\approx -2\left(\alpha_0^* \tilde{\beta}^* + \beta_0^* \tilde{\alpha}^*\right) M_0, \end{aligned} \tag{4.15}$$

$$\begin{aligned} \tilde{m}_z &\approx |\alpha_0 + \tilde{\alpha}|^2 - |\beta_0 + \tilde{\beta}|^2 - |\alpha_0|^2 + |\beta_0|^2 \\ &= 2\Re\left\{\alpha_0 \tilde{\alpha}\right\} + \tilde{\alpha}^* \tilde{\alpha} - 2\Re\left\{\beta_0 \tilde{\beta}\right\} - \tilde{\beta}^* \tilde{\beta} \\ &\approx 2\Re\left\{\alpha_0 \tilde{\alpha} - \beta_0 \tilde{\beta}\right\}. \end{aligned} \tag{4.16}$$

In these approximations we have dropped terms that are quadratic in $\left\{\tilde{b}_1, \ldots, \tilde{b}_R\right\}$, allowing us to use a "linear" Conjugate Gradient algorithm [12] in our method. We then form a

cost function in terms of the magnetization to design $\left\{\tilde{\boldsymbol{b}}_1, \ldots, \tilde{\boldsymbol{b}}_R\right\}$:

$$\Psi\left(\tilde{\boldsymbol{b}}_1, \ldots, \tilde{\boldsymbol{b}}_R\right) = \left\| \begin{bmatrix} \boldsymbol{m}_{xy}^{des} \\ \boldsymbol{m}_z^{des} \end{bmatrix} - \begin{bmatrix} \boldsymbol{m}_{xy}^0 + \tilde{\boldsymbol{m}}_{xy}\left(\tilde{\boldsymbol{b}}_1, \ldots, \tilde{\boldsymbol{b}}_R\right) \\ \boldsymbol{m}_z^0 + \tilde{\boldsymbol{m}}_z\left(\tilde{\boldsymbol{b}}_1, \ldots, \tilde{\boldsymbol{b}}_R\right) \end{bmatrix} \right\|_{\boldsymbol{W}}^2 + \\ + \lambda_1 \sum_{r=1}^{R} \left\| \boldsymbol{b}_r + \tilde{\boldsymbol{b}}_r \right\|^2 + \lambda_2 \sum_{r=1}^{R} \left\| \tilde{\boldsymbol{b}}_r \right\|^2, \tag{4.17}$$

where $\boldsymbol{m}_{xy}^{des}$ and $\boldsymbol{m}_z^{des}$ are the sampled desired transverse and longitudinal magnetization patterns, respectively, and $\boldsymbol{m}_{xy}^0$ and $\boldsymbol{m}_z^0$ are the transverse and longitudinal magnetization patterns excited by the initial pulses $\{\boldsymbol{b}_1, \ldots, \boldsymbol{b}_R\}$, and are computed via Bloch simulation. The Tikhonov regularization parameter λ_1 balances excitation error with total pulse power, while λ_2 can be set to enforce small perturbation pulse magnitudes, which may be necessary to maintain the accuracy of our approximations. As an alternative to using λ_2 to enforce small perturbation pulse magnitudes, one could simply incorporate a 'step-size' that multiplies $\left\{\tilde{\boldsymbol{b}}_1, \ldots, \tilde{\boldsymbol{b}}_R\right\}$ to ensure small pulse perturbations.

4.2.2 Fast computation of perturbed spinor parameters

Though the matrices $\boldsymbol{B}$ and $\boldsymbol{A}$ in Eqs. 4.11 and 4.13 contain Fourier kernels, overall they are non-Fourier due to $\alpha_0^*(\boldsymbol{x}_i, t_j)$ and $\beta_0(\boldsymbol{x}_i, t_j)$, respectively. This prevents us from directly using NUFFT's to evaluate matrix-vector products involving $\boldsymbol{B}$ and $\boldsymbol{A}$. Focusing on $\alpha_0^*(\boldsymbol{x}_i, t_j)$ for the moment, to enable fast computation we seek *separable* approximations of the form [16]:

$$\alpha_0^*(\boldsymbol{x}_i, t_j) \approx \sum_{l=1}^{L} c_{il} d_{lj} \qquad \begin{matrix} j = 1, \ldots, N_t \\ i = 1, \ldots, N_s. \end{matrix} \tag{4.18}$$

Substituting this approximation into Eq. 4.12 yields, in matrix form,

$$\boldsymbol{B} \approx \sum_{l=1}^{L} \text{diag}\{c_{il}\} \boldsymbol{G} \text{diag}\{d_{lj}\}, \tag{4.19}$$

where $\boldsymbol{G}$ is an $N_s \times N_t$ NUFFT operator with elements $g_{ij} = \frac{i\gamma}{2}\Delta t e^{-\frac{i}{2}\boldsymbol{x}_i \cdot \boldsymbol{k}(t_j)}$. We evaluate (4.19) efficiently using L NUFFT calls. Let $\boldsymbol{C} = \{c_{il}\} \in \mathbb{C}^{N_s \times L}$ and $\boldsymbol{D} = \{d_{lj}\} \in \mathbb{C}^{L \times N_t}$. The length-$N_t$ rows $\boldsymbol{d}_l$ of $\boldsymbol{D}$ can be interpreted as temporal basis vectors over which the rows of the matrix $\boldsymbol{\alpha_0^*} = \{\alpha(\boldsymbol{x}_i, t_j)\} \in \mathbb{C}^{N_s \times N_t}$ are expanded, with spatially-varying coefficients contained in the length-N_s columns $\boldsymbol{c}_l$ of $\boldsymbol{C}$. One approach to choosing $\boldsymbol{C}$ and $\boldsymbol{D}$ would be to compute the SVD of $\boldsymbol{\alpha}_0^*$. This choice would yield $\boldsymbol{C}$ and $\boldsymbol{D}$ that minimize the Frobenius norm

$$\underset{\boldsymbol{C},\boldsymbol{D}}{\operatorname{argmin}} \left\| \boldsymbol{\alpha}_0^* - \boldsymbol{C}\boldsymbol{D} \right\|_{Frob}^2. \tag{4.20}$$

Two issues are encountered in directly computing the full SVD of $\boldsymbol{\alpha}_0^*$; the first is illustrated in Fig. 4.1a. This figure plots the singular values, in descending order, of an $\boldsymbol{\alpha_0^*}$ matrix obtained by simulation of an accelerated spiral pulse, as well as from an accelerated echo-planar (EP) pulse. In both cases $\boldsymbol{\alpha_0^*}$ has a large number of singular values, so low-rank (i.e., small L) approximations to it will be highly inaccurate. However, it is possible to substitute an alternative form of $\alpha_0^*(\boldsymbol{x}_i, t_j)$ into Eq. 4.7 that results in a non-Fourier matrix (denoted as $\hat{\boldsymbol{\alpha}}_0^*$) with only a few significant singular values. We derive this new form from the small-excitation regime. In Chapter I we showed that for a pulse that rotates magnetization through a small angle, $\alpha_0^*(\boldsymbol{x}_i, t_j)$ is given by (Eq. 1.20):

$$\alpha_0^*(\boldsymbol{x}_i, t_j) = e^{-\frac{i\gamma}{2}\boldsymbol{x}_i \cdot \int_0^{t_j} \boldsymbol{G}(t')dt'}. \tag{4.21}$$

Substituting this analytical form into Eq. 4.12 yields:

$$\begin{aligned} b_{ij} &= \frac{i\gamma}{2} e^{-\frac{i\gamma}{2}\boldsymbol{x}_i \cdot \int_0^{t_j} \boldsymbol{G}(t')dt'} e^{-\frac{i}{2}\boldsymbol{x}_i \cdot \boldsymbol{k}(t_j)} \Delta t \\ &= \frac{i\gamma}{2} e^{-\frac{i}{2}\boldsymbol{x}_i \cdot \left(\boldsymbol{k}(t_j) - \boldsymbol{k}_f(t_j)\right)} \Delta t, \end{aligned} \tag{4.22}$$

where $\boldsymbol{k}_f(t) \triangleq -\gamma \int_0^t \boldsymbol{G}(t')\, dt'$. Because this equation contains no non-Fourier terms, an NUFFT can be used to directly evaluate it. In essence, to arrive at this expression we

have divided $\alpha_0^*(\boldsymbol{x}_i, t_j)$ by its' Fourier small-excitation solution, and absorbed that solution into the existing Fourier kernel, resulting in a unity term that need not be expanded, i.e., has one non-zero singular value. We have found empirically that even for large-tip-angle pulses, the matrix $\hat{\boldsymbol{\alpha}}_0^*$ with elements $\hat{\alpha}_0^*(\boldsymbol{x}_i, t_j) = \alpha_0^*(\boldsymbol{x}_i, t_j)\, e^{-\frac{i}{2}\boldsymbol{x}_i \cdot \boldsymbol{k}_f(t_j)}$ has only a few significant singular values. This result is plotted in Fig. 4.1a for the spiral and EP pulses. Therefore, an accurate low-rank approximation to $\hat{\boldsymbol{\alpha}}_0^*$ can be determined via SVD, enabling fast computation of Eq. 4.11. Figure 4.1b shows that the same result is true for $\beta_0(\boldsymbol{x}_i, t_j)$; i.e., that the matrix $\hat{\boldsymbol{\beta}}_0$ with elements $\hat{\beta}_0(\boldsymbol{x}_i, t_j) = \beta_0(\boldsymbol{x}_i, t_j)\, e^{-\frac{i}{2}\boldsymbol{x}_i \cdot \boldsymbol{k}_f(t_j)}$ has only a few significant singular values compared to $\boldsymbol{\beta}_0$. Intuitively, in the $\boldsymbol{\alpha}_0^*$ case, we use our separable approximation to represent the *deviation* from the Fourier small-excitation model for $\boldsymbol{\alpha}_0^*$ that is caused by the large-tip-angle pulses. It is interesting to note that $\hat{\beta}_0(\boldsymbol{x}_i, t_j)$ and $\hat{\alpha}_0^*(\boldsymbol{x}_i, t_j)$ correspond to the spin domain parameters observed in a frame rotating at the spatially- and temporally-varying frequency induced by the gradient fields, that we refer to as the *gradient frame*. We can transform α^* and β to and from the gradient frame via division and multiplication with $e^{\frac{i}{2}\boldsymbol{x}\cdot\boldsymbol{k}_f(t)}$, respectively.

The second computational issue is that too much memory and time would be required to compute the SVD of the full $\boldsymbol{\alpha_0^*}$ matrix in practice. To avoid this cost, we compute the SVD of a *reduced* $\boldsymbol{\alpha}_0^*$ matrix that is obtained by Bloch simulation of $\{b_1, \ldots, b_R\}$ over a subset of spatial locations, so that the reduced matrix has size $N_s^* \times N_t$, where $N_s^* \ll N_s$. The simulated locations are chosen to be uniformly distributed over the range of flip angles in the desired pattern. To choose the N_s^* locations, we divide the range of flip angles into N_b bins, $N_b < N_s^*$, then pull N_s^*/N_b locations from each bin by arranging the location indices within that bin lexicographically and taking evenly-spaced locations. An SVD of the reduced matrix yields the $L \times N_t$ temporal basis vector matrix $\boldsymbol{D}$ that we use to approximate $\alpha_0^*(\boldsymbol{x}, t)$ at all spatial locations, per (4.18). Once the matrix $\boldsymbol{D}$ is determined,

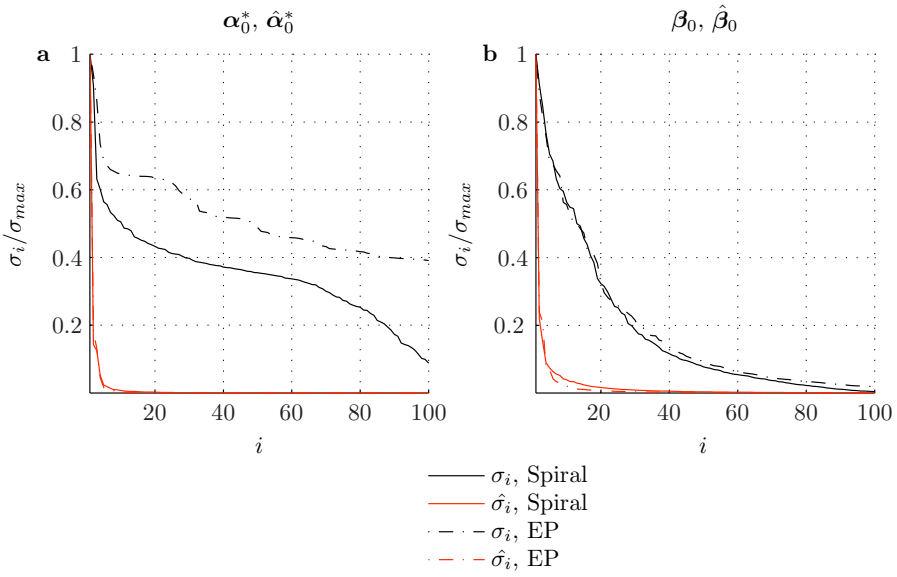

Figure 4.1: (a) The first 100 normalized singular values σ_i and $\hat{\sigma}_i$, plotted in descending order, of $\boldsymbol{\alpha}_0^*$ and $\hat{\boldsymbol{\alpha}}_0^*$, respectively. (b) The same, for $\boldsymbol{\beta_0}$ and $\hat{\boldsymbol{\beta}}_0$. The matrices were obtained by Bloch simulation of small-tip-designed accelerated spiral and EP pulses, that were scaled to excite large-tip-angles. $\hat{\boldsymbol{\alpha}}_0^*$ and $\hat{\boldsymbol{\beta}}_0$ possess few significant singular values compared to $\boldsymbol{\alpha}_0^*$ and $\boldsymbol{\beta_0}$, permitting accurate low-rank approximations to these matrices.

the least-squares optimal coefficient matrix $\boldsymbol{C}$ is determined as:

$$\boldsymbol{C}' = \left[\boldsymbol{D}\boldsymbol{D}'\right]^{-1} \boldsymbol{D}\left(\boldsymbol{\alpha}_0^*\right)' = \boldsymbol{D}\left(\boldsymbol{\alpha}_0^*\right)', \tag{4.23}$$

where the second equality follows from the orthogonality of singular vectors. This is computed as a running sum during Bloch simulation of $\{b_1, \ldots, b_R\}$ for all spatial locations, obviating the need to store the full matrix $\boldsymbol{\alpha}_0^*$.

We apply the same techniques to approximate $\boldsymbol{\beta}_0$, which we expand as

$$\beta_0\left(\boldsymbol{x}_i, t_j\right) \approx \sum_{l=1}^{L} e_{il} f_{lj} \quad \begin{matrix} j = 1, \ldots, N_t \\ i = 1, \ldots, N_s. \end{matrix} \tag{4.24}$$

This is substituted into Eq. 4.14, yielding

$$\boldsymbol{A} \approx \sum_{l=1}^{L} \mathrm{diag}\left\{e_{il}\right\} \boldsymbol{G} \mathrm{diag}\left\{f_{lj}\right\}. \tag{4.25}$$

The matrix $\boldsymbol{F} = \{f_{lj}\} \in \mathbb{C}^{L \times N_t}$ is computed using the SVD of a reduced $\boldsymbol{\beta}_0$ resulting from Bloch simulation of the initial pulses over a subset of spatial locations. The matrix is then used to compute the least-squares optimal $\boldsymbol{E}$ via:

$$\boldsymbol{E}' = \boldsymbol{F}\boldsymbol{\beta}_0', \tag{4.26}$$

which is calculated as a running sum during Bloch simulation for all spatial locations.

4.2.3 The Fast Optimal Control Algorithm

The required steps of the algorithm are summarized as follows.

Fast Optimal Control Algorithm

1. Simulate $\{\boldsymbol{b}_1, \ldots, \boldsymbol{b}_R\}$ using a Bloch equation simulator over a subset of spatial locations, yielding $\boldsymbol{\alpha}_0^*$ and $\boldsymbol{\beta}_0$ for these points.

2. Compute the SVD's of the reduced $\boldsymbol{\alpha}_0^*$ and $\boldsymbol{\beta}_0$ matrices to obtain temporal basis matrices $\boldsymbol{D}$ and $\boldsymbol{F}$.

3. Repeat the simulation of $\{\boldsymbol{b}_1, \ldots, \boldsymbol{b}_R\}$ for all spatial locations. Use (4.23) and (4.26) to compute the matrices $\boldsymbol{C}$ and $\boldsymbol{E}$ via running sums, to conserve memory. Also store the last columns of $\boldsymbol{\alpha}_0^*$ and $\boldsymbol{\beta}_0$ in preparation for computing the perturbed magnetization.

4. Using (4.11) and (4.13) to compute $\tilde{\boldsymbol{\beta}}$ and $\tilde{\boldsymbol{\alpha}}^*$, with the approximations of (4.19) and (4.25) for the matrices $\boldsymbol{B}$ and $\boldsymbol{A}$, and computing perturbed magnetization using (4.15) and (4.16), apply the CG algorithm to find the $\left\{\tilde{\boldsymbol{b}}_1, \ldots, \tilde{\boldsymbol{b}}_R\right\}$ that minimize (4.17) iteratively.

5. Set $\{\boldsymbol{b}_1, \ldots, \boldsymbol{b}_R\} \rightarrow \left\{\boldsymbol{b}_1 + \tilde{\boldsymbol{b}}_1, \ldots, \boldsymbol{b}_R + \tilde{\boldsymbol{b}}_R\right\}$ and return to step 1 until a convergence criterion is met.

4.3 Methods

4.3.1 Pulse Design

We used the fast optimal control method to design two-dimensional RF pulses, and compared it to additive-angle and conventional optimal control RF pulse design in simulations. Desired patterns were specified on a 64×64 grid, with a FOV of 24 cm $\times$ 24 cm, and were blurred by convolution with a Gaussian kernel of FWHM = 1.2 cm, to reduce ringing in the resulting excitation patterns. Bloch equation simulations for pulse design were performed on the same grid, while simulations for final error computation and comparison were performed on a finer 128×128 grid with the same FOV. Spins outside the ROI were not simulated.

The fast optimal control method alternated between Bloch simulations to update the $\boldsymbol{\alpha}_0^*$ and $\boldsymbol{\beta}_0$ expansions and 25 CG iterations. The expansions used $L = 4$ (Eqs. 4.19 and 4.25), except in simulation II, where L was varied. The SVD's for determination of the $\boldsymbol{\alpha}_0^*$ and $\boldsymbol{\beta}_0$ expansions were calculated on the results of a reduced Bloch simulation over a set of 50 representative spatial locations, that were chosen to uniformly sample the range of flip angles in the desired pattern. Fast optimal control iterations were stopped when the Normalized Root-Mean-Square Error (NRMSE), defined as

$$NRMSE = \frac{\left\| \boldsymbol{m}_{des} - \boldsymbol{m}\left(\tilde{\boldsymbol{b}}_1, \ldots, \tilde{\boldsymbol{b}}_R\right) \right\|}{\|\boldsymbol{m}_{des}\|}, \tag{4.27}$$

between the desired and Bloch-simulated magnetization patterns at the current Bloch/CG alternation decreased by less than 0.01% of the previous one. The Tikhonov regularization parameter for the perturbation pulses, λ_2 in Eq. 4.17, was initialized to $\lambda_2 = 10^{-2}$. This small value allows large perturbation pulse magnitudes, and therefore potentially large reductions in excitation error per alternation. However, our linear model's accuracy can also be degraded at large perturbation pulse magnitudes. To allow the greatest possible error

reduction per iteration while avoiding divergence due to model inaccuracy, we adopted the following scheme to adjust λ_2: if, at a given Bloch/CG alternation, the NRMSE of the total pulse exceeded 99.99% of that of the previous alternation, λ_2 was increased by a factor of 10. If λ_2 exceeded 10^3, alternations were stopped.

The method of [30] was used for conventional optimal control pulse design. This method optimized pulses using gradient descent, with a step size that was chosen to maximize downhill descent per iteration, while avoiding divergence. The method was stopped at 100 iterations. The small-tip design method in Chapter II was used to design initial pulses for all three large-tip methods, with 100 CG iterations and the same desired flip angle pattern. Small-tip-angle design was initialized with zero pulses. In all design methods, pulses were designed with small λ_1, the total pulse Tikhonov regularization parameter in Eq. 4.17, except in Simulation II, where λ_1 was varied for the fast optimal control method. For pulse design, Bloch simulations were initialized with all magnetization in M_z. All pulse designs and simulations were performed in MATLAB R2007a (Mathworks, Natick, MA, USA), on a 3.4GHz Pentium IV workstation with 2GB RAM.

4.3.2 Numerical Simulations

Simulations of parallel excitation were carried out assuming the same 8 element active rung transmit array and phantom configuration of Chapter III. The ROI for pulse design and error calculation was the phantom interior. The desired pattern, shown in Fig. 3.1b, was a rectangular block that was centered in the phantom, with dimensions 10 cm $\times$ 5 cm.

We designed pulses using spiral and echo-planar (EP) excitation k-space trajectories. Spiral trajectories were single-shot spiral-out with the parameters: maximum amplitude = 4 G/cm, maximum slew rate = 18 G/cm/ms. Acceleration was achieved via undersampling in the radial direction, resulting in reduction of the excitation field of view (XFOV) of the individual coils' excitation patterns. EP trajectories were designed using the parameters:

maximum amplitude = 4 G/cm, maximum slew rate = 15 G/cm/ms. For these trajectories, acceleration was achieved via undersampling in the blipped (phase-encoded) dimension. The spatial resolution for all trajectories was 0.75 cm, which is twice that of the grid on which the desired patterns were specified. The sampling period for all pulses was 4 μs.

Simulation I: Speedup Factor

In the first simulation, we designed $\frac{\pi}{2}$- and π-excitation pulses with a range of speedup factors from 2.4 to 6, corresponding to an XFOV range from 10 cm down to 4 cm. We compared performance of the fast optimal control method to that of additive angle and conventional optimal control design in terms of NRMSE between excited and desired magnetization patterns, peak total RF field magnitude, and visual quality. Compute time was also recorded for the optimal control method.

Simulation II: Convergence

In this simulation we investigated convergence properties of the fast optimal control method. We repeated fast optimal control designs of EP (speedup factor = 3) and spiral (speedup factor = 4.8) π-pulses, and varied design parameters that may influence final excitation error and peak total pulse power. We first varied the Tikhonov regularization parameter λ_1 (Eq. 4.17) from $\log_{10}\lambda_1 = -1$ to $\log_{10}\lambda_1 = 2.25$. This parameter adjusts the balance between excitation error and integrated total pulse magnitude. We then performed designs over a range of L values, from 1 to 10, where L is the expansion order of our approximations to the matrices $\boldsymbol{\alpha}_0^*$ and $\boldsymbol{\beta}_0$ in Eqs. 4.19 and 4.25.

Simulation III: Refocusing

In our third simulation, we applied an EP π-pulse designed for inversion to refocusing of a spin population. An EP pulse with speedup factor = 3 (XFOV = 8 cm, pulse length 3.34 ms) was used in these simulations. We performed 40 simulations that were initialized

with magnetization in the transverse plane everywhere in the object, but over a phase range of 0-2π radians, in 40 equally-spaced angular steps. The initial phase represents the phase accrued due to off-resonance between excitation and TE/2. After application of the pulse, the initial phase was again added to the magnetization's phase, representing the phase accrued between the refocusing pulse (TE/2) and TE. We then summed the magnetization over the phase range, to obtain the net magnetization at TE. Phase evolution due to off-resonance during pulse application was neglected, due to the short duration of the pulse.

4.4 Results

4.4.1 Simulation I: Speedup Factor

Figure 4.2 plots error versus speedup factor for the three pulse design methods. In terms of flip angle RMS error, the methods all perform equally well, for both spiral and EP pulses, and both π and $\frac{\pi}{2}$ flip angles. This fact is also demonstrated in Fig. 4.3. In that figure, the M_z profiles produced by fast optimal control-designed pulses are very similar to those produced by additive angle-designed pulses. Though the EP M_z profile excited by fast method's pulses (Fig. 4.3b) appears rougher in the inverted region than the additive angle pulses' profile, the NRMSE of these profiles, measured on M_z, is 2.7 % lower for the fast optimal control method. This is due to improved excitation fidelity in the transition regions of the pattern. The biggest advantage of the optimal control methods is exhibited in the plots (Figs. 4.2(b,d)) of magnetization error ($NRMSE_{xyz}$) versus speedup factor, where we see that the optimal control methods achieve consistently lower error than the additive angle method. The excitation patterns shown in Fig. 4.4 demonstrate that in the EP case (Fig. 4.4(a,b)) this is partly due to reduced erroneous excitation outside of the desired pattern. However, if we examine M_x and M_y profiles through the centers of these patterns (Fig. 4.5), we see the dominant reason for this reduction: the optimal control

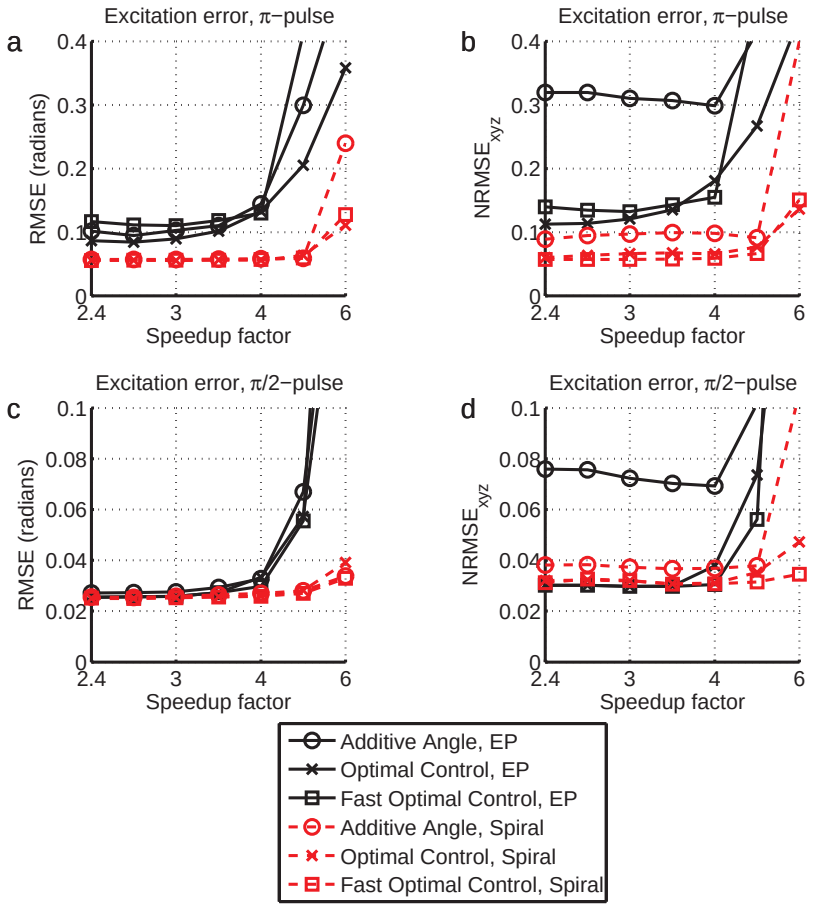

Figure 4.2: Error vs. speedup factor for the additive angle method, the conventional optimal control method, and the fast optimal control method, for π- and $\frac{\pi}{2}$-spiral and EP pulses. In terms of flip angle error (a,b), the optimal control methods achieve the same or better accuracy than the additive angle method. In terms of NRMSE calculated on the magnetization directly (b,d), the optimal control methods produce pulses that are consistently more accurate than those produced by the additive angle method. The fast optimal control method achieves similar error to the conventional optimal control method.

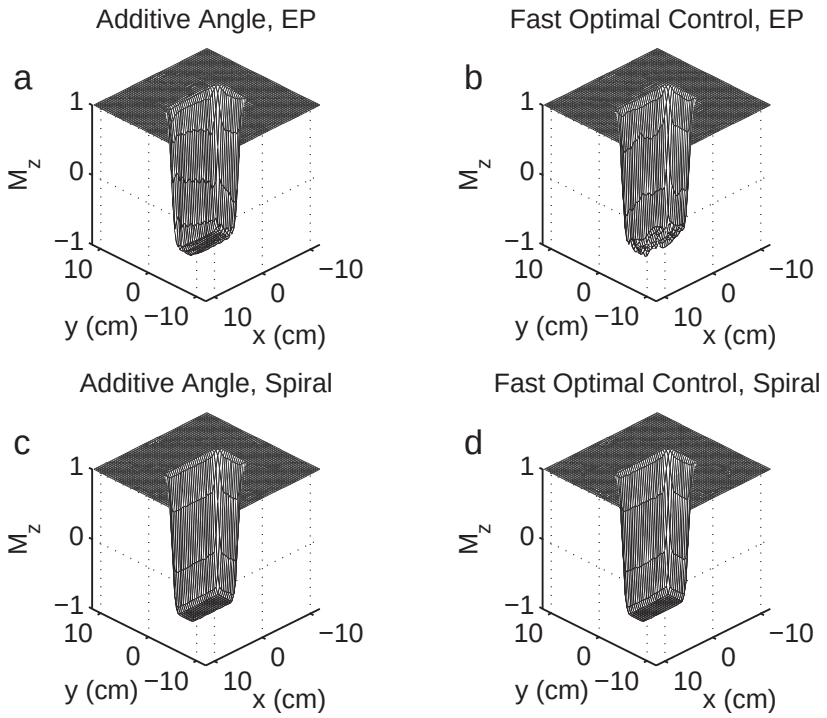

Figure 4.3: Simulated M_z patterns produced by π-pulses designed with the additive angle (a,c) and fast optimal control (b,d) methods, for an EP trajectory (a,b) with speedup factor = 3 (XFOV = 8 cm, pulse length 3.34 ms), and a spiral trajectory (c,d) with speedup factor = 4.8 (XFOV = 5 cm, pulse length 1.16 ms). The M_z patterns excited by the methods are of similar quality, though in the EP case the z-NRMSE is 2.7% lower for the fast optimal control-designed pulses.

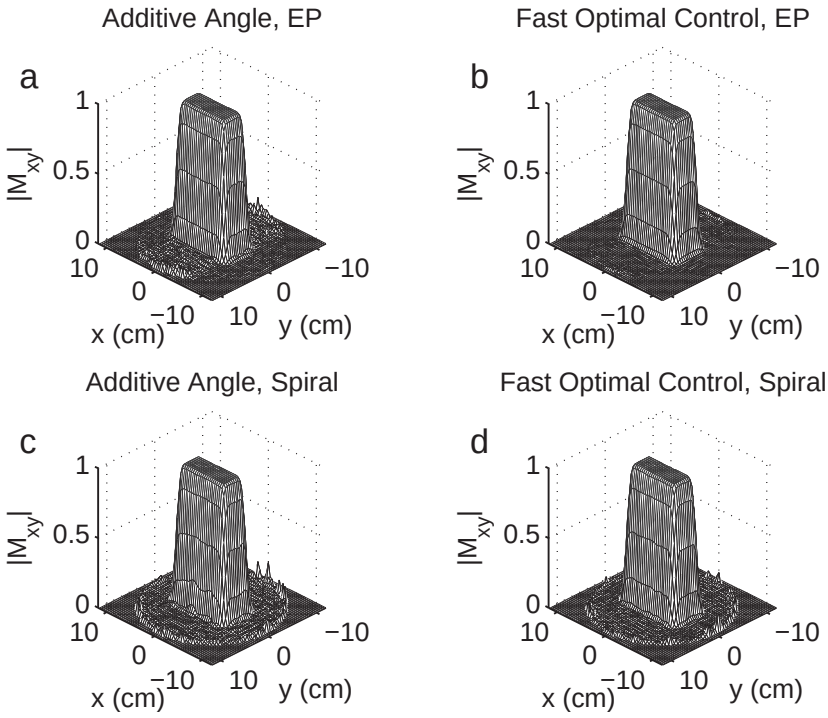

Figure 4.4: Simulated M_{xy} patterns produced by $\frac{\pi}{2}$-pulses designed with the additive angle (a,c) and fast optimal control (b,d) methods. For the EP trajectory (a,b) with speedup factor = 4 (XFOV = 6 cm, pulse length 2.7 ms), pulses designed with the fast optimal control method produce patterns with reduced erroneous excitation outside the block. For the spiral trajectory with speedup factor = 6 (XFOV = 4 cm, pulse length 1 ms), similar magnetization profiles are excited.

methods produce pulses with accurate excitation phase. Our desired pattern specifies that all excited magnetization should lie along the M_x direction, corresponding to zero phase. While the additive angle method allows the excited phase to drift between iterations, hence allowing non-zero M_y, the optimal control method maintains the desired phase.

Figure 4.2 also shows that for spiral π-pulses and for spiral and EP $\frac{\pi}{2}$-pulses, the fast optimal control method produces pulses of equal or better accuracy than the conventional optimal control method. In the case of EP π-pulses, however, the conventional method converges to pulses of lower accuracy than those produced by the fast method, for all but one of the simulated speedup factors. To demonstrate that it is possible to use the fast method to design pulses of the same accuracy as the conventional method, we re-ran the EP π-pulse simulations with a larger value of λ_2, which encourages small perturbation pulse

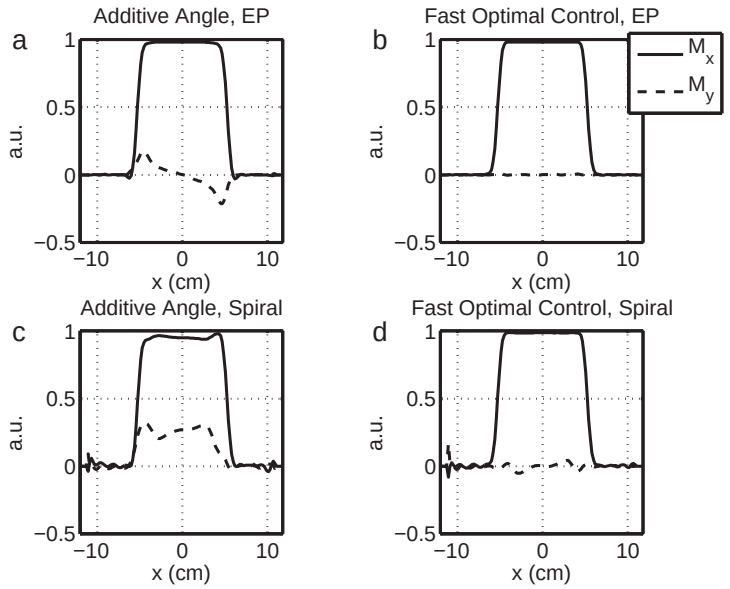

Figure 4.5: Profiles through the center ($y = 0$) of the excited magnetization patterns of Fig. 4.4. For both EP and spiral pulses, the fast optimal control method excites patterns with more uniform phase, as evidenced by the smaller imaginary (M_y) magnetization components in (b) and (d).

magnitudes for which our model is more accurate, at the cost of increased design time. The results of these additional simulations are shown in Fig. 4.6. Here, we increased λ_2 from 10^{-2} to 10^2. The increased regularization parameter discouraged large perturbation pulse magnitudes, thereby maintaining our model's accuracy. This in turn caused the fast method to converge to pulses of more similar accuracy to those designed with the conventional method. Design times for the two methods are compared in Fig. 4.7. The figure plots the design times for EP and spiral π-pulses. For the EP pulse, the fast method converged to a design $NRMSE_{xyz}$, measured on the 64×64 design grid, of 10.34% in 7.5 minutes. To reach this same level of error, the conventional method required 69 iterations, which took 114 minutes. In this case, the fast method achieved a 15.2-fold reduction in design time. For the spiral π-pulse, the fast method converged to a much lower design $NRMSE_{xyz}$ than was reached by the conventional method, $NRMSE_{xyz}$ = 0.92%. In contrast, the minimum design error reached by the conventional method in 100 iterations

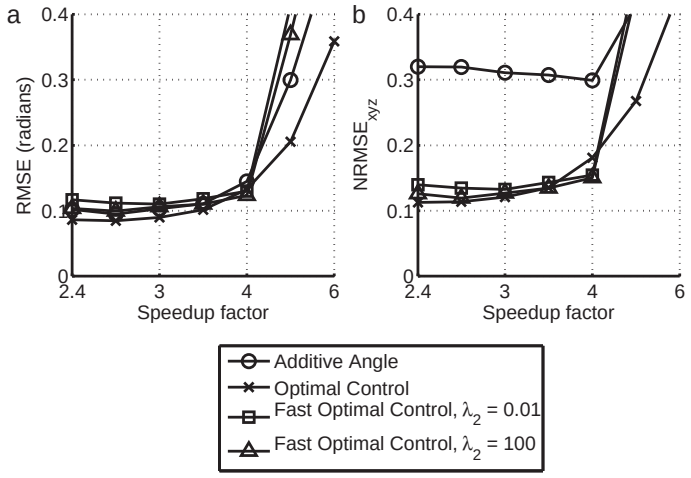

Figure 4.6: Error vs. speedup factor for EP π-pulses designed with the additive angle method, the conventional optimal control method, and the fast optimal control method with $\lambda_2 = 10^{-2}$ and 10^2. Increasing λ_2 encourages smaller perturbation pulse magnitudes for which our approximate model is more accurate. This in turn leads to a reduction in excitation error, resulting in error levels that are closer to that of pulses designed using conventional optimal control. This improvement comes at the cost of increased computation time.

was $NRMSE_{xyz}$ = 2.81 %, in 67.5 minutes. The fast optimal control method reached this same error in 3.2 minutes, corresponding to a 21.2-fold reduction in design time.

4.4.2 Simulation II: Convergence

Figure 4.8 plots the dependence of the fast optimal control-designed pulses' error and peak RF magnitude on the various design parameters. As the total pulse Tikhonov regularization (λ_1) is increased, the fast method trades $NRMSE_{xyz}$ for lower pulse power, and therefore lower pulse magnitude, as shown in Figs 4.8(a,b). Therefore, the user can adjust λ_1 to balance this tradeoff in a given design scenario. In Fig. 4.8c, the final $NRMSE_{xyz}$ is plotted against the order of the $\boldsymbol{\alpha}_0^*$ and $\boldsymbol{\beta}_0$ matrix expansions, L. Interestingly, the final error is approximately independent of L, especially for the spiral design case. Figure 4.8d plots the design $NRMSE_{xyz}$ as a function of Bloch/CG alternation, for $L = 1$ and $L = 10$. This figure indicates, especially for the spiral case, that while L may not significantly influence the final design error, using a smaller L does cause a greater number of

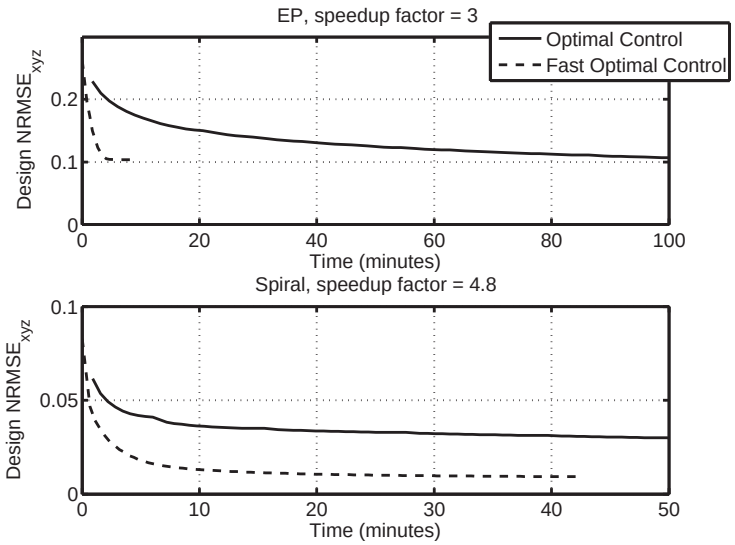

Figure 4.7: Comparison of design times for conventional and fast optimal control methods. For the EP case (π-pulse speedup factor = 3), a 15.2-fold reduction in design time was achieved by the fast method. For the spiral case (π-pulse, speedup factor = 4.8), the error achieved by the fast method was never reached by the conventional method, though the fast method achieved the conventional method's final error with a 21.2-fold reduction in design time.

Bloch/CG alternations to be required to reach a low error level. Because L influences the time required to perform each CG design, this result indicates that L should be chosen to optimize design time. For example, if Bloch equation simulations are computationally inexpensive compared to CG iterations, a smaller L may minimize the design time, while if Bloch simulations are very computationally expensive, the required number of simulations can reduced by choosing larger L.

4.4.3 Simulation III: Refocusing

Figure 4.9 shows the results of our refocusing simulation. As evidenced in Fig. 4.9a, the pulse successfully rotated magnetization by π radians within the block, and zero radians outside. This resulted in coherent signal addition within the block, and complete signal cancellation outside. The phase pattern of the summed magnetization is shown in Fig. 4.9b. We see from this image that the phase within the refocused region is spatially varying, with a standard deviation of 25.4°. This corresponds to a reduction in phase devi-

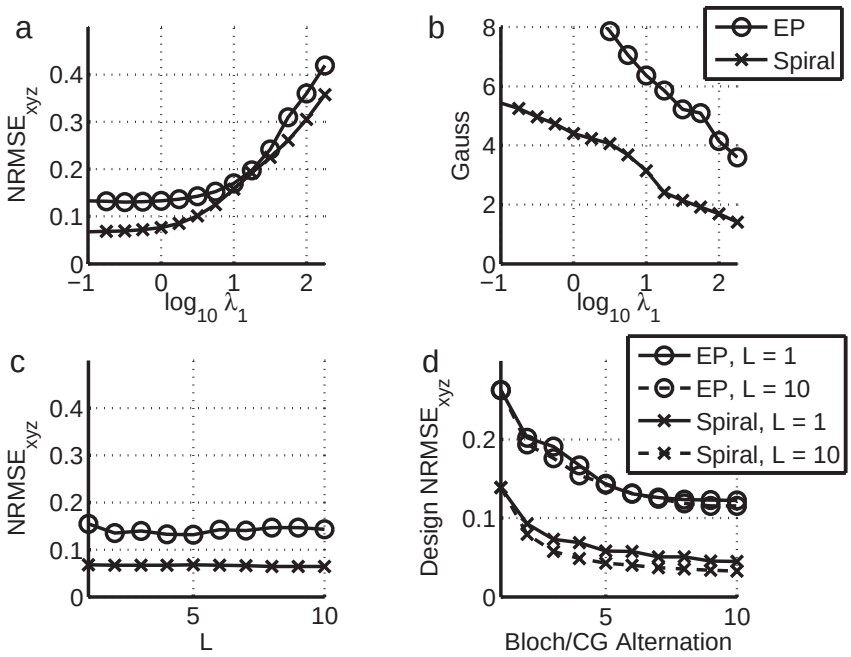

Figure 4.8: Influence of design parameters. (a,b) The total pulse Tikhonov regularization parameter (λ_1) can be tuned to balance excitation accuracy against peak RF magnitude. (c) Final excitation accuracy is largely independent of the $(\boldsymbol{\alpha}_0^*, \boldsymbol{\beta}_0)$ expansion order, L, but (d) shows that fewer Bloch/CG alternations are required for larger values of L.

ation compared to additive angle-designed pulses of Chapter III, Figure 3.8, which excited a refocused pattern with phase deviation 34°.

4.5 Discussion and Conclusions

In this chapter we have introduced a new method for fast large-tip-angle RF pulse design in parallel excitation. It is a fast version of the optimal control pulse design method, first introduced by Conolly et al [25], and extended to parallel excitation by Xu et al [30]. The method is derived directly from the spin-domain Bloch equation, by analyzing the difference between the Bloch equation of a set of large-tip-angle pulses plus small perturbation pulses, and the Bloch equation of the small perturbation pulses alone. By approximating a few terms in the difference equations as zero, we were able to derive a Fourier-like relationship between the perturbation pulses and the perturbations they produce to the

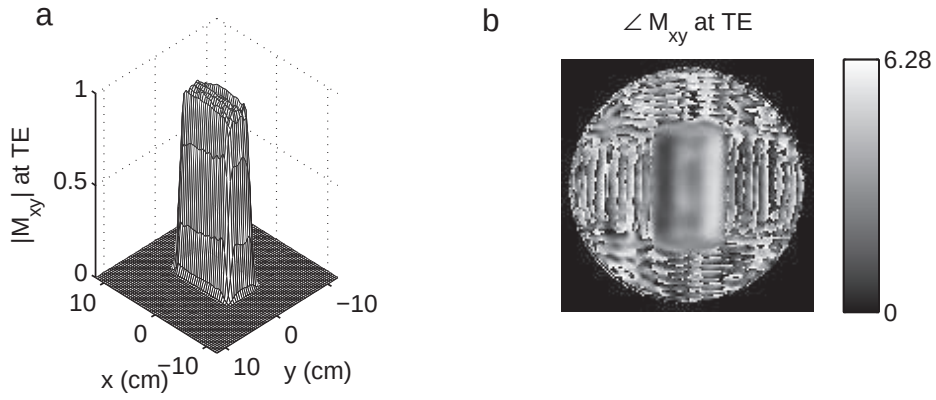

Figure 4.9: Fast optimal control-designed EP π-pulse (speedup factor = 3) applied as a refocusing pulse. (a) The pulse succeeds in uniformly rotating magnetization by π radians within the block, and zero radians outside. (b) The net phase of the refocused magnetization is spatially varying.

spinor parameters of the large-tip-angle pulses.

There are two central ideas we have introduced that make our method 'fast'. The first is the linearization of the spin-domain Bloch equation that results in a Fourier-like linear relationship between perturbation pulses and the perturbations they produce. This relationship alone could be valuable to a pulse designer, particularly in scenarios where the pulses being designed are parameterized. For example, this may arise when designing the weights on the spokes of a fast-k_z trajectory [27], where each spoke contains a sinc pulse whose magnitude we wish to optimize to achieve a flat in-plane excitation pattern. In this scenario, Eqs. 4.11 and 4.13 could be evaluated exactly for each spoke of the trajectory, avoiding the need for further accelerations. The second innovation we introduced was the translation of the $\boldsymbol{\alpha}_0^*$ and $\boldsymbol{\beta}_0$ matrices to the gradient frame of reference. This dramatically reduced the rank of these matrices, allowing us to use low-rank separable approximations to represent them accurately. This idea is necessary if the method is to be feasible when applied to general pulse design scenarios.

Compared to the additive angle method of Chapter III, this new method has some attractive advantages. First, the fast optimal control method is based upon a more solid

theoretical foundation. However, in the limiting case where the expansion order $L = 1$, the additive angle method and the fast optimal control method have essentially the same functional form. It would be an interesting exercise to determine just how closely related they are in this case, and what exactly the difference between the methods is. Insight gained from this exercise could result in the derivation of a more solid theoretical foundation for the additive angle method, or a simpler fast optimal control method, whereby the $\boldsymbol{\alpha}_0^*$ and $\boldsymbol{\beta}_0$ expansions may be determined without SVD. Though the fast optimal control method generally requires longer compute times than the additive angle method (several minutes compared to about two minutes), we showed in Simulation I that it has the additional practical advantage of allowing the user to control the excitation phase. This will be important both in applications where the user desires a specific phase pattern, and where the imaging sequence does not resolve across all excited dimensions. Though not shown here, the fast optimal control method should allow inclusion of off-resonance effects in the pulse design, resulting in off resonance-compensated pulses. The inclusion of off-resonance effects causes the additive angle method to diverge before a satisfactory level of accuracy is achieved. This is a topic for future investigation.

Compared to the conventional optimal control method, we demonstrated that our method generally achieves more than an order of magnitude reduction compute time. Furthermore, the fast method requires significantly less memory. Efficient implementation of the conventional optimal control requires the storage of 6 $N_s \times N_t$ matrices, where N_s is the number of points in the spatial design grid, and N_t is the number of time points in the pulses. The matrices contain the three magnetization components resulting from the forward and reverse Bloch simulations that are required at each iteration. This memory requirement can be restrictive for longer two-dimensional pulse designs, and renders three-dimensionl pulse design unfeasible on a workstation. In comparison, the fast method only requires

storage of $2L$ length-N_s vectors and $2L$ length-N_t vectors, where $L \ll N_s$ and $L \ll N_t$, and NUFFT interpolators. Therefore, the fast method can be used to design a much wider range of pulses.

Another topic for future investigation is the application of our method to designing refocusing pulses. While we showed that π inversion pulses designed with our method can be applied as refocusing pulses if one does not care about exciting a flat phase pattern, a designer will generally desire control over the phase of the refocused pattern. Directly designing refocusing pulses is a more constrained problem than designing an inversion pulse, since inversion pulses can excite magnetization about any vector; they need only produce a π rotation. In our initial investigations, we have found that controlling the phase of π-pulses is a more challenging problem than controlling the phase of $\frac{\pi}{2}$-pulses. Simply demanding that pulses rotate magnetization from $+M_x$ to $-M_x$ is not sufficient, since the design algorithm can either produce pulses that rotate magnetization about a transverse-plane (x-y) vector, or pulses that rotate magnetization about the z-axis using the gradient field. Pulses that use the gradient field to rotate magnetization will fail when applied as refocusing pulses. To avoid this pitfall, we can design the pulses in the spin domain, which allows us to directly specify the flip angle and rotation vector at each point in space. However, we have found that it is difficult to reach sufficiently-accurate pulses in this case using the fast optimal control method. This is most likely due to the more non-linear nature of the Bloch equation in the π flip-angle regime, which causes our method to converge to a local minimum of insufficient accuracy. Therefore, it may be necessary to seek new initializers other than those provided by small-tip-angle designs, that are closer to the desired pulses. For example, EP pulse designs could be initialized with a series of SLR-weighted sinc pulses [44]. Another possibility is to design pulses in the magnetization domain, by specifying multiple initial magnetization states in the transverse plane, each

with its own target state. This also avoids the possibility of designing pulses that rotate about the z-axis.

In conclusion, the method we have introduced permits the design of large-tip-angle parallel excitation pulses that are more accurate than those produced by the additive angle method, in a shorter time than that required by the conventional optimal control method. We have verified our method in simulations of two-dimensional spiral and EP parallel RF pulse design. Future work will concentrate on the inclusion of off-resonance effects in the method, and its application to the design of refocusing pulses.

CHAPTER V

Contributions and future work

The research reported in this thesis has explored methods for small- and large-tip-angle RF pulse design in parallel excitation. In Chapter II we introduced a new method for small-tip-angle RF pulse design. In Chapter III we introduced a simple but effective method for designing large-tip-angle parallel excitation pulses that is capable of designing accurate pulses with a small number of Bloch simulations. In Chapter IV we explored a fast optimal control pulse design technique that aimed to complement the shortcomings of the simple method in Chapter III. Let us recap the problems that each of these methods aim to solve, and highlight their strengths, weaknesses and opportunities for future work.

5.1 Small-tip-angle parallel pulse design

We showed that the small-tip-angle method of Chapter II has several advantages over the competing methods described in Chapter I, which include transmit SENSE [1], transmit GRAPPA [22], and Zhu's SENSE-like method [2]. It is a model-based approach that is computationally efficient, optimal in a squared-excitation error sense, and allows the user to model system non-idealities such as off-resonance. The method has been used experimentally by other groups [20, 52–56], and is favored for its simplicity - one need only discretize the small-tip-angle integral (Eq. 2.2) to a matrix-vector form and let the conjugate gradient algorithm do the heavy lifting. It is also straightforward to include

off-resonance and to improve excitation error using ROI's. However, the method does have some drawbacks that could lead a user to choose a different method. In analogy to the SENSE [3] vs. GRAPPA [4] debate in parallel imaging, the first drawback is that it requires accurate determination of transmit sensitivities, while transmit GRAPPA does not. Another potential drawback is that a computationally-efficient implementation of the method requires an NUFFT algorithm, which, while conceptually simple, are not ubiquitous, and will therefore generally require extra coding on the user's part. In contrast, transmit GRAPPA and Zhu's method are formulated as parameter fitting problems that are of smaller dimension and therefore easy to implement efficiently.

There are many opportunities for future work on small-tip-angle RF pulse design. Within the context of the spatial-domain method are opportunities to reduce computation time, which could be approached in two ways. First, one could aim to reduce the number of iterations required to design a pulse via initialization or preconditioning. Our group has developed an alternative parallel RF pulse design algorithm that is sub-optimal but applies to general trajectories and is faster than the spatial-domain method, costing half the compute time of one CG iteration [57]. The method produces pulses of an accuracy that requires several CG iterations of the spatial domain method. Particularly in the case of longer pulses, it could be used to initialize spatial-domain CG iterations to achieve a reduction in compute time. One could also take the approach of reducing the cost per CG iteration. Yoon et al [58] have introduced a Toeplitz version of our method that avoids NUFFT's altogether, instead reformulating the design problem using the push-through matrix identity. In the standard CG algorithm, at each iteration one computes $\boldsymbol{A}'_{full}\boldsymbol{A}_{full}\boldsymbol{b}_{full}$ by first computing $\boldsymbol{y} = \boldsymbol{A}_{full}\boldsymbol{b}_{full}$ using an NUFFT, and then computing $\boldsymbol{A}'_{full}\boldsymbol{y}$, again using an NUFFT. The Toeplitz approach reformulates the problem so that at each iteration, we instead evaluate $\boldsymbol{A}_{full}\boldsymbol{A}'_{full}\boldsymbol{b}_{full}$, where $\boldsymbol{A}_{full}\boldsymbol{A}'_{full}$ is a block-Toeplitz matrix,

with which multiplications can be evaluated using two FFT's, at a computational cost that is roughly half that of the original formulation. There may also be opportunities to develop specialized NUFFT's that somehow take advantage of the fact that for each system matrix multiply (i.e., each time we evaluate $\boldsymbol{A}_{full}\boldsymbol{b}_{full}$), multiple NUFFT's are computed and their results are summed. Another approach to reducing design time is to parameterize RF pulses, for instance using wavelet or spline bases. One could pre-compute the magnetization excited by each basis waveform and store the result. Online pulse design would involve finding (a few) least-squares optimal coefficients for the basis expansion, which would be chosen to provide as compact a representation as possible.

On a note related to pulse parameterization, another question that may require resolution before parallel excitation achieves widespread adoption is the appropriate choice of the RF pulse temporal point spread function (PSF's) in the design process. Traditionally, RF pulse design methods have assumed that the excitation PSF is either a Dirac delta function, or a boxcar function. Though they can be easily generalized to any point spread function, our own small- and large-tip-angle pulse design methods have assumed that the PSF is a Dirac delta function. This assumption has not been problematic to previous researchers since the designed pulses have always been very smooth, e.g., sinc-like, due to slower traversal through excitation k-space, and any smoothing effected by the RF chain has little effect. However, in parallel excitation, we have both a faster traversal of k-space, and the additional sensitivity encoding mechanism, so we can no longer assume that the designed pulses will be smooth. In my own experience, accelerated pulses can be very 'spikey', but the narrow spikes in the pulses are surely smoothed somewhat due to the finite bandwidth of the RF amplifiers chain. Characterization of the temporal PSF of a given excitation system may be required to ensure excitation fidelity. The temporal PSF could probably be measured easily on the bench, using magnetic field probes and an os-

cilloscope, and should remain relatively consistent from patient to patient (i.e., between coil loads). Of course, this whole problem is avoided if pulses are parameterized by wide, smooth basis functions.

Outside the context of our spatial-domain method, there are opportunities to improve the performance of small-tip-designed pulses in practical situations that may be effectively addressed by extensions to our method. One problem that users of parallel excitation will face is uncertainty in the transmit sensitivity patterns. This could be the result of estimation error, patient motion during readout, and many other sources. It may be possible to design parallel pulses that are robust to sensitivity errors, for instance by reducing the speedup factor of a pulse and penalizing for aliased excitation that the design algorithm expects will be cancelled by another coil, but may not be when the pulses are deployed on the scanner. Another issue I have found empirically concerns the large-tip-angle performance of small-tip-designed spiral parallel pulses. The issue is that while an unaccelerated set of spiral pulses that are designed using the spatial domain method excite a pattern at small tip-angles that matches the accuracy of a single-channel spiral pulse, when scaled to produce large-tip-angles, the pulses often excite a distorted pattern compared to the single-channel pulse. The cause of this is perplexing, since there is no theoretical reason why parallel pulses would not satisfy the linear class conditions [8]. Instead, I believe the cause is the design algorithm. While the total RF deposition of pulses designed with the spatial-domain method would be Hermitian symmetric for a real-valued excitation pattern, it is likely that along one or more rungs of the spiral, energy is deposited in a non-Hermitian symmetric manner, that is then expected to be cancelled out by an adjacent rung. Again, it may be possible to discourage this effect via regularization, for instance by enforcing that each coil excite a strictly real-valued pattern.

5.2 Large-tip-angle parallel pulse design

In Chapter II, we analyzed the performance of small-tip-designed parallel pulses at large-tip-angles, and demonstrated that, even when scaled to $90°$, the accelerated pulses excited patterns that were highly distorted compared to unaccelerated pulses. This analysis motivated our exploration of large-tip-angle methods, and we have introduced two of these. Like the spatial-domain method, the additive-angle method introduced in Chapter III has the advantage of being simple to implement, provided one already has code to design small-tip-angle parallel pulses, and Bloch simulation code. The method reduces the number of Bloch simulations required to design a large-tip-angle pulse, compared to competing optimal control-like algorithms [26, 28, 30]. It is also surprisingly robust to design parameters, such as step size and the initial pulses' excited flip angle. There are drawbacks to the method, that we improved upon with the fast optimal control method. The first is that the additive angle method was not formulated as the minimization of a specific cost function; instead, it was based on the observation that the squared flip angle error of an excited pattern can be generally reduced by adding pulses together that excite magnetization with the same phase. In contrast, the fast optimal control method was formulated as the minimization of a cost function that was a function of magnetization components, and as a result generally produces more accurate pulses. The optimal control method also controls excitation phase, which is particularly advantageous in echo-planar pulse designs in which the initial pulses excite a highly distorted phase pattern. Furthermore, the fast optimal control method would robustly account for off-resonance during pulse design. In initial experiments with the additive angle method, I have found that the inclusion of an off-resonance map can cause the algorithm to diverge. This should not be an issue for the model-based fast optimal control method, and is a topic of future research. These ad-

vantages do come at a cost in compute time, as it generally takes longer to design pulses using the optimal control method. Even before parallel excitation becomes available, the large-tip-angle algorithms I developed could find applications in single-channel multidimensional pulse design. One example application is the design of fast-k_z pulses for B1+ inhomogeneity compensation [27], a problem that has been explored in the small-tip-angle regime by Stenger et al. Our methods could extend these pulse designs to large-tip-angles. Other potential applications include reduced-FOV imaging [59, 60], in which multidimensional pulses or successive one-dimensional pulses along orthogonal directions are used to restrict the FOV for decreased scan time, and spectroscopy [61], where the same can be done to select a voxel.

My future work with large-tip-angle pulse design will focus on gradient waveform design and optimization. In the small-tip-angle regime, the design of gradient waveforms can be largely informed by Fourier analysis, though it is somewhat complicated by the non-Fourier nature of sensitivity encoding. In the large-tip-angle regime, where we do not have generally have a Fourier relationship between a pulse and its excitation pattern, gradient optimization techniques stand to make a larger impact. Recently, our group has demonstrated an extension of the spatial-domain method that jointly designs RF pulses and the phase-encoding locations of an echo-planar excitation trajectory [62]. The method calculates parameterizes the echo-planar trajectory, and uses analytical gradient formulas to optimize encoding locations using gradient descent. Because gradients are computed with respect to the Fourier kernel, this method does not readily extend to large-tip-angle pulse design. However, it may be possible to apply the perturbation analysis employed by the fast optimal control method to the gradient waveforms, and to derive a linear relationship between perturbations in the gradient waveforms and perturbations they produce in the spinor parameters. Not only would this permit fast gradient waveform design at large-

tip-angles, it could also be solved using the conjugate gradient algorithm, obviating the need to choose a step size. Such a technique could also be applied to the small-tip-angle regime. Another area of investigation is the initialization of large-tip-angle pulse design methods. Both of the iterative methods presented in this thesis were initialized with small-tip-designed pulses. Though this may be the best choice of initializer for spiral pulses that generally behave well at large-tip-angles to begin with, there may be better choices for other trajectories such as echo-planar.

BIBLIOGRAPHY

BIBLIOGRAPHY

[1] U Katscher, P Börnert, C Leussler, and J S van den Brink. Transmit SENSE. *Magn Reson Med*, 49(1):144–150, Jan 2003.

[2] Y Zhu. Parallel excitation with an array of transmit coils. *Magn Reson Med*, 51(4):775–784, Apr 2004.

[3] K P Pruessmann, M Weiger, M B Scheidegger, and P Boesiger. SENSE: Sensitivity encoding for fast MRI. *Magn Reson Med*, 42(5):952–962, Nov 1999.

[4] M A Griswold, P M Jakob, R M Heidemann, M Nittka, V Jellus, J Wang, B Kiefer, and A Haase. Generalized autocalibrating partially parallel acquisitions (GRAPPA). *Magn Reson Med*, 47(6):1202–1210, Jun 2002.

[5] F Bloch. Nuclear induction. *Phys. Rev.*, 70:460–473, 1946.

[6] E T Jaynes. Matrix treatment of nuclear induction. *Phys. Rev.*, 98(4):1099–1105, May 1955.

[7] J M Pauly, D G Nishimura, and A Macovski. A k-space analysis of small-tip-angle excitation. *Magn Reson Med*, 81:43–56, 1989.

[8] J M Pauly, D G Nishimura, and A Macovski. A linear class of large-tip-angle selective excitation pulses. *J Magn Reson*, 82(3):571–587, 1989.

[9] C Y Yip, J A Fessler, and D C Noll. Iterative RF pulse design for multidimensional, small-tip-angle selective excitation. *Magn Reson Med*, 54(4):908–917, Oct 2005.

[10] P Börnert and B Aldefeld. On spatially selective RF excitation and its analogy with spiral MR image acquisition. *MAGMA*, 7(3):166–178, Dec 1998.

[11] T B Harshbarger and D B Twieg. Iterative reconstruction of single-shot spiral MRI with off resonance. *IEEE Trans Med Imaging*, 18(3):196–205, 1999.

[12] B P Sutton, D C Noll, and J A Fessler. Fast, iterative image reconstruction for MRI in the presence of field inhomogeneities. *IEEE Trans Med Imaging*, 22:178–188, 2003.

[13] P Munger, G R Crelier, T M Peters, and G B Pike. An inverse problem approach to the correction of distortion in EPI images. *IEEE Trans Med Imaging*, 19(7):681–689, 2000.

[14] J A Fessler and B P Sutton. Nonuniform fast Fourier transforms using min-max interpolation. *IEEE Trans Sig Proc*, 51(2):560–574, 2003.

[15] C Y Yip, J A Fessler, and D C Noll. Advanced three-dimensional tailored RF pulse for signal recovery in T2*-weighted functional magnetic resonance imaging. *Magn Reson Med*, 56(5):1050–9, 2006.

[16] J A Fessler, S Lee, V T Olafsson, H R Shi, and D C Noll. Toeplitz-based iterative image reconstruction for MRI with correction for magnetic field inhomogeneity. *IEEE Trans Sig Proc*, 53(9):3393–3402, 2005.

[17] D C Noll, W A Grissom, and C Y Yip. RF pulse design for parallel excitation. ISMRM, May 2006.

[18] T S Ibrahim, R Lee, B A Baertlein, A M Abduljalil, H Zhu, and P M Robitaille. Effect of RF coil excitation on field inhomogeneity at ultra high fields: a field optimized TEM resonator. *Magn Reson Imaging*, 19(10):1339–1347, 2001.

[19] A Kangarlu, B A Baertlein, R Lee, T Ibrahim, L Yang, A M Abduljalil, and P M Robitaille. Dielectric resonance phenomena in ultra high field MRI. *J Comput Assist Tomogr*, 23(6):821–831, Nov-Dec 1999.

[20] Z Zhang, C Y Yip, W Grissom, D C Noll, F E Boada, and V A Stenger. Reduction of transmitter B1 inhomogeneity with transmit SENSE slice-select pulses. *Magn Reson Med*, 57(5):842–847, May 2007.

[21] Z Zhang and V A Stenger. Validation of transmit SENSE with reciprocity. In *Proceedings 13th Scientific Meeting, International Society for Magnetic Resonance in Medicine, Miami Beach*, page 2434, 2005.

[22] M A Griswold, S. Kannengiesser, M Muller, and P M Jakob. Autocalibrated accelerated parallel excitation (Transmit-GRAPPA). In *Proceedings 13th Scientific Meeting, International Society for Magnetic Resonance in Medicine, Miami Beach*, page 2435, 2005.

[23] W Grissom, C Y Yip, Z Zhang, V A Stenger, J A Fessler, and D C Noll. Spatial domain method for the design of RF pulses in multicoil parallel excitation. *Magn Reson Med*, 56(3):620–9, Sep 2006.

[24] C Hardy, P Bottomley, M O'Donnell, and P Roemer. Optimization of two-dimensional spatially selective NMR pulses by simulated annealing. *J Magn Reson*, 77:233–250, 1988.

[25] S Conolly, D Nishimura, and A Macovski. Optimal control solutions to the magnetic resonance selective excitation problem. *IEEE Trans Med Imaging*, 5:106–115, 1986.

[26] J L Ulloa, M Callaghan, P Irarrazaval, J Hajnal, and M Guarini. Calculation of B1 pulses for RF shimming at arbitrary flip angle using multiple transmitters. In *Proceedings 14th Scientific Meeting, International Society for Magnetic Resonance in Medicine, Seattle*, page 3016, 2006.

[27] S Saekho, C Y Yip, D C Noll, F E Boada, and V A Stenger. Fast-kz three-dimensional tailored radiofrequency pulse for reduced B1 inhomogeneity. *Magn Reson Med*, 55(4):719–724, Apr 2006.

[28] K Setsompop, A C Zelinski, V A Alagappan, U J Fontius, F Hebrank, F Schmitt, L L Wald, and E Adalsteinsson. High flip angle slice selective parallel RF excitation on an 8-channel system at 3T. In *Proceedings 15th Scientific Meeting, International Society for Magnetic Resonance in Medicine, Berlin*, page 677, 2007.

[29] W H Press. *Numerical recipes in C*. Cambridge University Press, 2nd ed., v2.0 edition, 1993.

[30] D Xu, K F King, Y Zhu, G McKinnon, and Z-P Liang. Multidimensional arbitrary-flip-angle parallel transmit pulse design using an optimal control approach. In *Proceedings 15th Scientific Meeting, International Society for Magnetic Resonance in Medicine, Berlin*, page 1696, 2007.

[31] W Grissom, J A Fessler, and D C Noll. Time-segmented spin domain method for fast large-tip-angle RF pulse design in parallel excitation. In *Proceedings 15th Scientific Meeting, International Society for Magnetic Resonance in Medicine, Berlin*, page 676, 2007.

[32] J. A. Fessler, D. Yeo, and D. C. Noll. Regularized fieldmap estimation in MRI. In *Biomedical Imaging: Macro to Nano, 2006. 3rd IEEE International Symposium on Biomedical Imaging*, pages 706–709, 2006.

[33] D C Noll, C H Meyer, J M Pauly, D G Nishimura, and A Macovski. A homogeneity correction method for magnetic resonance imaging with time-varying gradients. *IEEE Trans Med Imaging*, 10:629–637, 1991.

[34] E Schneider and G Glover. Rapid in vivo proton shimming. *Magn Reson Med*, 18(2):335–347, Apr 1991.

[35] R H Chan and M K Ng. Conjugate gradient methods for Toeplitz systems. *SIAM Review*, 38(3):427–482, 1996.

[36] W A Grissom, J A Fessler, and D C Noll. Additive angle method for fast large-tip-angle RF pulse design in parallel excitation. In *Proceedings 15th Scientific Meeting, International Society for Magnetic Resonance in Medicine, Berlin*, page 1689, 2007.

[37] W A Grissom, C Y Yip, S M Wright, J A Fessler, and D C Noll. Additive angle method for fast large-tip-angle RF pulse design in parallel excitation. *Magn Reson Med*, 2007, Accepted for publication.

[38] D Xu, K F King, Y Zhu, G C McKinnon, and Z P Liang. A noniterative method to design large-tip-angle multidimensional spatially-selective radio frequency pulses for parallel transmission. *Magn Reson Med*, 58(2):326–334, Jul 2007.

[39] E T Lebsack and S M Wright. Iterative RF pulse refinement for magnetic resonance imaging. *IEEE Transactions on Biomedical Engineering*, 49:41–48, 2002.

[40] J T Ngo and P G Morris. General solution to the NMR excitation problem for noninteracting spins. *Magn Reson Med*, 5(3):217–237, Sep 1987.

[41] K N Kurpad, E B Boskamp, and S M Wright. A parallel transmit volume coil with independent control of currents on the array elements. In *Proceedings 13th Scientific Meeting, International Society for Magnetic Resonance in Medicine, Miami Beach*, page 16, 2005.

[42] S M Wright. 2D full-wave modeling of SENSE coil geometry factors at high fields. In *Proceedings 10th Scientific Meeting, International Society for Magnetic Resonance in Medicine, Honolulu*, volume 10, page 854, 2002.

[43] A Funai, J A Fessler, W Grissom, and D C Noll. Regularized B1+ map estimation in MRI. In *Biomedical Imaging: Macro to Nano, 2007. 4th IEEE International Symposium on Biomedical Imaging*, pages 616–619, 2007.

[44] J Pauly, D Spielman, and A Macovski. Echo-planar spin-echo and inversion pulses. *Magn Reson Med*, 29(6):776–782, Jun 1993.

[45] Christoph Schroder, Peter Bornert, and Bernd Aldefeld. Spatial excitation using variable-density spiral trajectories. *J Magn Reson Imaging*, 18(1):136–141, 2003.

[46] V A Stenger, F E Boada, and D C Noll. Variable-density spiral 3D tailored RF pulses. *Magn Reson Med*, 50(5):1100–1106, Nov 2003.

[47] S Conolly, D G Nishimura, A Macovski, and G Glover. Variable-rate selective excitation. *J Magn Reson*, 78:440–458, 1988.

[48] I Graesslin, S Biederer, F Schweser, K-H Zimmerman, U Katscher, and P Börnert. SAR reduction for parallel transmission using VERSE and k-space filtering. In *Proceedings 15th Scientific Meeting, International Society for Magnetic Resonance in Medicine, Berlin*, page 674, 2007.

[49] A E Bryson and Y-C Ho. *Applied Optimal Control*. Halsted Press, New York, NY, USA, 1981.

[50] W E Kyriakos, W S Hoge, and D Mitsouras. Generalized encoding through the use of selective excitation in accelerated parallel MRI. *NMR Biomed*, 19(3):379–392, May 2006.

[51] W E Kyriakos and L P Panych. Implementation of wavelet encoded MRI with large flip-angle RF pulses. In *Proceedings 5th Scientific Meeting, International Society for Magnetic Resonance in Medicine, Seattle*, page 1990, 1997.

[52] P Ullmann, S Junge, M Wick, F Seifert, W Ruhm, and J Hennig. Experimental analysis of parallel excitation using dedicated coil setups and simultaneous RF transmission on multiple channels. *Magn Reson Med*, 54(4):994–1001, Oct 2005.

[53] P Ullmann, F Schubert, R Haueisen, S Junge, F Seifert, M Wick, W Ruhm, and J Hennig. Flexible feature specific inner-volume selection with transmit SENSE: Methods and applications in humans, animals and biological samples. In *Proceedings 14th Scientific Meeting, International Society for Magnetic Resonance in Medicine, Seattle*, page 598, 2006.

[54] P Ullmann, S Junge, F Seifert, G Wuebbeler, J Hennig, and W Ruhm. SAR-analysis for transmit SENSE with a 4-channel head array at 3 T. In *Proceedings 14th Scientific Meeting, International Society for Magnetic Resonance in Medicine, Seattle*, page 601, 2006.

[55] A Kerr, R Watkins, R Giaquinto, J Pauly, Y Zhu, and C Cunningham. Self-calibrated transmit SENSE. In *Proceedings 14th Scientific Meeting, International Society for Magnetic Resonance in Medicine, Seattle*, page 2561, 2006.

[56] H Nam, WA Grissom, and S M Wright. Application of RF current sources in transmit SENSE. In *Proceedings 14th Scientific Meeting, International Society for Magnetic Resonance in Medicine, Seattle*, page 2562, 2006.

[57] W A Grissom, J A Fessler, and D C Noll. Transmit-PILS RF pulse design for small-tip-angle parallel excitation. In *Proceedings 16th Scientific Meeting, International Society for Magnetic Resonance in Medicine, Toronto*, 2008, Submitted.

[58] D Yoon, W A Grissom, J A Fessler, and D C Noll. Toeplitz-based acceleration of RF pulse design for parallel excitation. In *Proceedings 16th Scientific Meeting, International Society for Magnetic Resonance in Medicine, Toronto*, 2008, Submitted.

[59] D A Feinberg, J C Hoenninger, L E Crooks, L Kaufman, J C Watts, and M Arakawa. Inner volume MR imaging: technical concepts and their application. *Radiology*, 156(3):743–747, 1985.

[60] M T Alley, J M Pauly, F G Sommer, and N J Pelc. Angiographic imaging with 2D RF pulses. *Magn Reson Med*, 37(2):260–267, 1997.

[61] A Haase. Localization of unaffected spins in NMR imaging and spectroscopy (LOCUS spectroscopy). *Magn Reson Med*, 3(6):963–969, 1986.

[62] C Y Yip, W Grissom, J A Fessler, and D C Noll. Joint design of trajectory and RF pulses for parallel excitation. *Magn Reson Med*, 58(3):598–604, 2007.